Engineering biomimetic formulations for drug and gene delivery

Hanze Hu

Submitted in partial fulfillment of the
requirements for the degree of
Doctor of Philosophy
under the Executive Committee
of the Graduate School of Arts and Sciences

COLUMBIA UNIVERSITY

2022

Abstract

Engineering biomimetic formulations for drug and gene delivery

Hanze Hu

Nanotechnology-based solutions have gained burgeoning attention in medical research, as compared with conventional therapeutic modalities, they offer advantages in efficacy, safety, and scalability. Researchers have been developing fluidic systems for nanoformulations over recent decades. Despite promising results, the clinical potential of the current nanosystems is still limited by insufficient cargo (drug and gene) loading, low production, high toxicity, low colloidal stability, unsatisfied bioavailability, and batch-to-batch variation.

Flash-based self-assembly is a recently developed technology that can manufacture nanoformulations in facile, consistent, reproducible, and scalable manners. Due to the turbulent and dynamic flow generated in the mixing chamber, biomaterials self-assemble into uniform nanoparticles (NPs) through precipitation or complexation. We modified and manufactured a number of flash-based systems and evaluated their dynamic mixing profiles through simulation and empirical testing for polyplex formation and nanoparticle coating, as the dynamic fluidic control is the key for biomaterial complexation and nanoparticle coating, which provides better nanoparticle colloidal stability. In Chapter 2, we formulated polyplexes and lipid-coated NPs with controllable size and enhanced colloidal stability by exploiting the dynamic mixing of the flash-based system.

Bio-inspired nanosystems with engineered functions have been advancing the field of nanomedicine. Incorporating bio-inspired components can provide nanosystems with productive ways of interacting with their surroundings by diminishing nonspecific interactions or enhancing specific targeting. Membranes from different cell types, and even organisms, can be employed

and merged to meet specific goals. We derived cell membranes from distinctive mammalian cell lines to improve nanosystems with smart biological interactions, such as preserving neo-antigens or enhancing specific targeting. Another potent property of utilizing cell membranes is that they provide NPs with colloidal stability. Recent studies have reported the use of cell membrane coating onto NPs in drug delivery, imaging, phototherapies, and detoxification. The derived components from the original cell source bestow the NPs with their inherent functionality without additional complicated modulation. Cell membrane coating is a top-down technique that directly derives and harnesses the natural components, evading the technical and procedural challenges in bottom-up fabrication. However, current membrane coating techniques have problems of batch-to-batch variation and low production yield, which limits its potential for clinical translation. Taking advantage of flash-based self-assembly, we standardized and scaled up the cell membrane-coating process, which is difficult to achieve in bulk mixing approaches. The optimization of cell membrane coating was explored using various simulations. The time and cost for experimental design and optimization were reduced considerably. Cell membranes derived from tumor cells contain a rich source of tumor antigens. With the potential of cell membrane coating using flash-based self-assembly, we applied the produced cell-membrane-coated mesoporous silica nanoparticles (MSN) as a biomimetic nanovaccine for cancer immunotherapy in Chapter 3.

Oral delivery of drugs and genes is a relatively convenient, patient-friendly, and safe approach. Targeted and controlled oral delivery of active pharmaceutical ingredients (API) of biomimetic nanocarriers offers significant advantages in efficacy and safety compared to conventional modalities. Besides mammalian cells, the unique functionalities of other prokaryotic and eukaryotic cell types, such as bacterium and yeasts, were exploited for

macromolecule delivery. Baker's yeast, a common yeast strain closely associated with food preparation, contains valuable polysaccharides that were reported to specifically bind to the dectin-1 receptors on the specialized intestinal epithelial cells and monocytes. Exploiting the yeast's cell wall is a biomimetic strategy when designing an oral carrier for targeted oral drug and gene delivery. We demonstrated that the specific recognition between the microfold cells (M-cells) of the small intestine and the polysaccharides on the yeast cell wall enhances the transport of yeast-based formulations across the gut epithelium and into the lymphatic tissues in chapter 4. Utilizing the micron-sized yeast capsule or decorating a nanoparticle surface with processed yeast cell wall fragments, therapeutics were efficiently delivered to the target site through the oral path. The yeast-based formulations are biomimetic systems for targeted oral delivery of therapeutics.

Taken together, the goal of this thesis is to close the gap between laboratory research and clinical translation by exploring the versatility and robustness of the developed flash technology, exploiting flash-based self-assembly for scalable production of the lipid and cell-membrane-coated nanosystems, and developing a relatively safe yeast-based drug and gene delivery platform

Table of Contents

List of Charts, Graphs, Illustrations

Acknowledgments

The work presented in this thesis represents years of effort that would not have been possible without the support of many people and different communities. First and foremost, I would like to express my sincere gratitude to Dr. Kam Leong, my Ph.D. advisor. Without him, it would have been impossible to have this valuable opportunity and unique platform to access all the necessary resources. To his mentees, Dr. Leong has always conveyed his ideology of being a scientist held to the highest standards and a righteous individual-diligent, modest, rigorous, deep thinking, and scrupulous. Under his guidance and mentorship, I learned to be, and to always better myself, to be an independent and rigorous scientist carrying responsibility for medicine and human society on my shoulder. During my journey in my doctoral studies, I have been trained extensively not only in science and Socratic thinking but have also learned essential skills that are crucial to be successful as an engineer, leader, collaborator, team player, and someone beneficial for the human society. Next, I would also like to thank Dr. Mingqiang Li and Dr. Dan Shao for providing me with technical guidance and support when I was in the early years of my Ph.D. studies. Dr. Li and Dr. Shao taught me many important technical skills to follow up on independent research. I would also like to thank all the collaborators and lab mates, Zixuan Xiao, Suwan Ding, Danielle (Dantong) Huang, Dr. Chao Yang, Dr. Huiyi Liang, Elena Ivanova, Dr. Helen Lee, Dr. Zhaoxu Tu, and Dr. Naoto Yoshinaga, for all their kind support and contribution to my Ph.D. studies. Undeniably, there have been many ups and downs during the five years of my Ph.D. life; Dr. Nicole Gonzalez has given me a tremendous amount of support and assistance during these times. Importantly, I would like to send special gratitude to my family. They had provided a large amount of financial and emotional support, sending me to study in a foreign

country when I was seventeen years old. I would also like to thank all my friends who have supported me all the time. Importantly, I want to acknowledge the guidance and patronage from my Ph.D. committee: Dr. Henry Hess, Dr. Helen Lu, Dr. Harris Wang, and Dr. Tal Danino. National Institutes of Health grants (Nos. UG3NS115598 and AR073935) and DARPA HR001118S0037-PA-008 are acknowledged. (Data in Specific Aims 3.2 were collected with the help of Dr. Dan Shao, Dr. Chao Yang, and Dr. Mingqiang Li).

Chapter 1: Overview of Research Objectives

1.1 Background

The advent of nanomedicine marks an unparalleled opportunity to develop unprecedented solutions for a wide variety of healthcare challenges[1–6]. There has been an exponential increase in nano-platform designs for drug and gene delivery with the fast-growing progress in nanotechnology and biomaterials[7–13]. Recently, lipid-based nanoformulations like lipid nanoparticles (LNP) have gained tremendous attention in RNA delivery and nanovaccine formulations. Since the first FDA-approved siRNA drug Patisiran and the most recent successful COVID-19 mRNA vaccines, many nanoformulations have been undergoing pre-clinical IND and clinical trials[14]. Despite these recent successes, efforts are still needed to understand the formulation process (nucleic acid encapsulation efficiency, complexation process of the ionizable lipid and nucleic acid, detailed mechanism after administration) of these nucleic acid-based NPs. Moreover, to improve the bioavailability of the therapeutics, functioning nanocarriers with tissue targeting ability, enhanced circulation, longer half-life, and minimal cytotoxicity are needed. Nano-platforms are typically constructed with engineered functions to facilitate the transport of the delivery system to the target site. Moreover, controlled release and environmental-responsive release can vastly improve the drug bioavailability and biosafety profile of the nanosystems[15–17]. Specifically, the nanocarrier composed of synthetic or natural biomaterials degrades to release its cargo in response to environmental changes such as altered pH, increased amount of glutathione, or elevated levels of reactive oxygen species[18–20]. The nanocarrier itself can also possess intrinsic homing properties[21–23]. To further facilitate navigation of these nanosystems to the desired delivery site, efforts have focused on decorating the nanoplatforms with synthetic or natural biomaterials to evade systemic clearance by the

reticuloendothelial system (RES) or to enhance specific tissue biodistribution by targeting distinctive cell receptors[24–27]. Also, the scalability and reproducibility of these cutting-edge nanosystems are essential to clinical translation. Nevertheless, numerous technologies and platforms are awaiting improvements before they can be truly translatable, owing to the batch-to-batch variation, limited production, undesired administration route, and low bioavailability. Issues like production inconsistency and low bioavailability of drugs are partly due to the uncontrollable process of the material self-assembly process. Self-assembly, the process of chaotic components forming an organized structure under external forces, plays a pivotal role in nanoformulations, and it has biological applications such as anti-bacterial treatment, imaging, and theranostics[28–37]. Self-assembly has been achieved using a variety of different techniques, including layer-by-layer assembly, sonication, bulk mixing, controlled growth, microfluidic-assisted hydrodynamic focusing, and evaporation-induced assembly. Although promising, only a very few of the developed nanoformulation methods can fully satisfy manufacturing requirements. The majority of these formulation techniques have limitations of product heterogeneity, low production yield, and large batch-to-batch variations[38–40]. Continuous, high-yield, repeatable, and dynamic self-assembly technologies are urgently needed. Flash nanocomplexation (FNC), which involves turbulent mixing in confined impingement jets mixers (CIJM) or multiple inlet vortex mixers (MIVM), facilitates rapid self-assembly and formation of nanocomplexes in a low-cost, high-throughput, and controllable manner (**Figure 1**). The self-assembly process can be exploited for diverse nanocomplexes to benefit a multitude of biological applications[41,42]. The quality of nanocomplexes can be maintained over the collection process in a manufacturing pipeline, which is vital for product consistency and clinical translation.

Engineering ideas are often enlightened from nature, where biomimicry can be applied for the development of nanosystems. For example, mesenchymal stem cells have the intrinsic property of homing to tumor sites[43]. We can harness this property by exploiting the cell membrane of the mesenchymal stem cells to design hybrid nanosystems for targeted tumor delivery[23,43]. Furthermore, prolonging nanoparticle circulation time and achieving specific tissue targeting can be accomplished by fabricating target□related cell□derived nanoparticle systems for drug and gene delivery[44]. This can be done by coating the NPs with natural or engineered cell membranes. In the past decade, cell membrane□based nanotechnology has emerged as a promising approach to facilitate the delivery of therapeutic agents. This top□down approach is defined by coating synthetic nanocarriers with a layer of the natural cell membrane, which improves the colloidal stability of NPs and minimizes the nonspecific tissue accumulation with selected cell membrane types. Conventionally, conjugating targeting ligands onto the nanoparticle surface endows its specific targeting function. However, the complexity of the chemistry and potential toxicity are often problematic when engineering these multifunctional systems[26,45]. Cell membrane□coated NPs could inherently reproduce the biological properties of the source cells from which their membranes are derived, aiming to achieve a wide range of functions, such as prolonged circulation and tissue-specific targeting, without the tediousness of chemical synthesis in the bottom-up strategy[27]. In part of this thesis, utilizing our developed flash-based system, we show that coating cell membrane fragments onto NPs can be achieved in a scalable and robust manner to benefit nanoformulation and drug delivery. **Figure 2** proposed herein is to comprehensively explore the possibility of utilizing FNC to coat cell membrane fragments onto biodegradable NPs for the development of a cancer nanovaccine. The scalability and reproducibility of the flash-based cell membrane coating process will expedite the clinical

translation of membrane-based nanoformulations by providing a standardized protocol to the field.

Oral delivery has been long recognized as the preferred route of administration of therapeutics due to its high patient compliance, ease of administration, and high cost-effectiveness. Nevertheless, gut variability among individuals, the difference in diet and colonization of the gut microbiome, low pH, proteolytic enzymes, and the presence of negatively charged mucosal layer all contribute to the complication of oral delivery of APIs. Gelatin capsule or other synthetic excipients have been exploited for encapsulating APIs and serves as a protection for the cargo from acid and enzymes. The most recent example of an oral anti-COVID-19 drug, Molnupiravir, has entered clinical studies[46]. However, burst release and low bioavailability of most oral formulations prevent them from fully unleashing their translational potential. Many recent studies have suggested intestinal lymphatic system (ILS) can be a preferred route for drug transport. The ILS consists of the gut-associated lymphoid tissue (GALT), which is the largest lymphatic organ in the body, accommodating as many as 60-70% of the peripheral immune cells[47–49]. Also, the GALT includes the Peyer's patches (PPs) as well as the lacteals and lymph capillaries that drain both the intestinal villi and PPs, which are functionally connected to the mesenteric lymph nodes. Microfold cells or M-cells are largely present on the ILS, especially in the ileum region of the small intestine. Considering M-cells have the excellent ability for transcytosis of large particles and macromolecules and there is less mucus cover on top of them, they could be exploited for nanoparticle transport. Importantly, the phagocytotic pattern receptors, dectin-1 and CR3, bind well with the β-1,3-glucan on the yeast cell wall to facilitate its transcytosis through M-cells[50–61]. The basal side of the M-cells often invaginates into the curved cavity to harbor antigen-presenting cells (APCs), such as circulating

macrophages and immature dendritic cells. These APCs can further carry the yeast-based NPs to the lymphatic system and later the systematic circulation. Again, the unique compositions of the microbiome cell wall promote specific cellular interaction, phagocytosis, and immunomodulation of the nanocarrier[16,62,63]. Inactivation of the live commensal and pathogenic microbiome while exploiting their unique remaining functions is the new biomimetic strategy for oral drug and gene delivery. For drainage to the lymphatic tissues, the micro-size of yeasts may limit their distribution and uptake efficiency in targeted organs and lymph nodes. Adopting the targeting function of the yeast cell wall onto a nanoparticulate system without affecting the nanoparticle size is important because the small nanoparticle size (50-100 nm) is advantageous for lymphatic drainage of these NPs[64,65]. Important polysaccharides residing on the yeast cell walls can also be harnessed for nanoparticle coating, therefore further enhancing the nanoparticle transport through the gut epithelium via M-cells and entering the systematic circulation (**Figure 3**). Improved lymphatic transport and bloodstream uptake of the NPs by yeast-based decoration makes the yeast-based system an ideal candidate for targeted oral drug and gene delivery, not only for cancer chemotherapy but also for immune modulation.

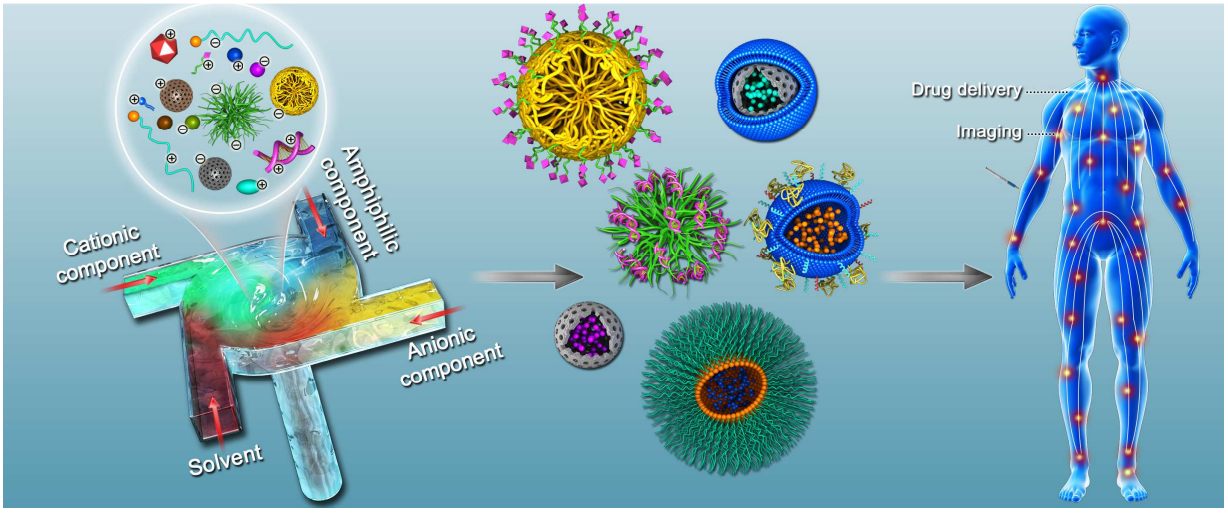

Figure 1: Overall schematic of flash-based self-assembly in preparing formulations for biological applications.

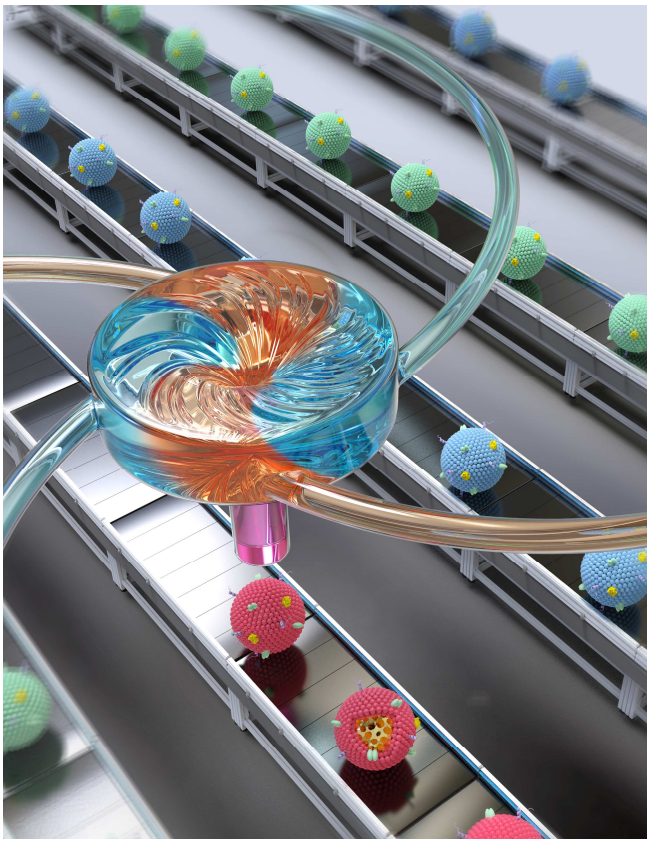

Figure 2: Cartoon illustration of the scalable production of cell-membrane-coated MSNs *via* flash-based nanoformulation.

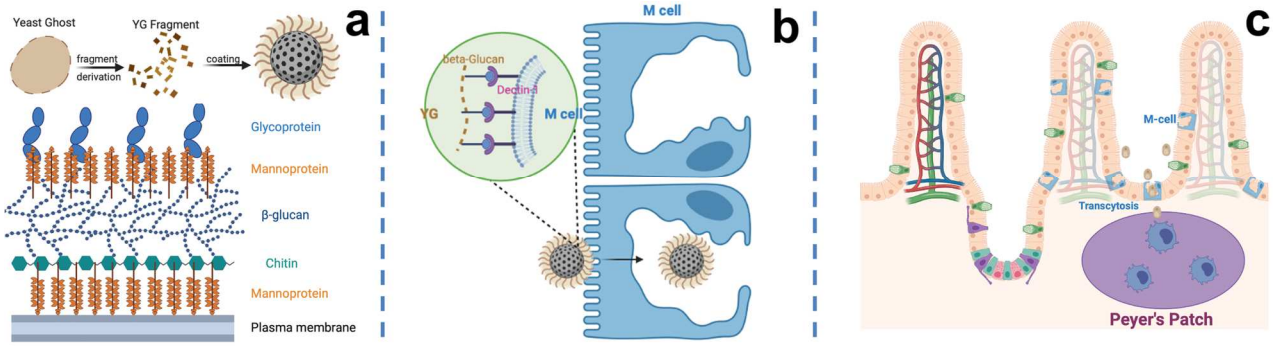

Figure 3: Schematic illustration of yeast-based system for nanoparticle delivery from (a) preparation to (b, c) schematic of the yeast-based systems for transcytosis through M-cells and crossing the gut epithelium.

1.2 Objectives and Specific Aims

Projects from all three aims are intended to link the bench-top science to future clinical translation of the described biomimetic nanoparticulate systems. Aim 1 is to design, test and demonstrate a flash-based system that can manufacture formulations in a scalable and reproducible manner. Aim 2 is to demonstrate the versatility of the cell membrane coating onto a variety of particles and to prove the robustness of the flash-based formulation by coating adjuvant-loaded NPs with cancer cell membranes for cancer immunotherapy. Aim 3 is to develop a yeast-based formulation for efficient oral drug and gene delivery by protecting the cargo from pH and enzymatic degradation and enhancing transport across the gut epithelial into the vasculature.

Specific Aim 1 (SA1): Development of FNC platform and evaluation of the versatility of flash-based technology

- SA1.1 Design and manufacture FNC devices
- SA1.2 Prepare and characterize flash-based self-assembled nanoformulations
- SA1.3 Prepare and characterize flash-based lipid-coated nanoformulations

Specific Aim 2 (SA2): Development of cell membrane-based nanoformulations for cancer immunotherapy

- SA2.1 Characterize flash-based cell membrane-coated nanoformulations
- SA2.2 *In vitro* and *ex vivo* evaluation of membrane-coated formulations on APC uptake and lymph node targeting performance
- SA2.3 *In vivo* validation of membrane-coated nanoformulations for cancer immunotherapy

Specific Aim 3 (SA3): Development of microbiome-based formulations for oral drug and gene delivery

- SA3.1 Prepare and characterize microbiome-based formulations
- SA3.2 *In vitro* and *in vivo* study of therapeutic efficacy of yeast-based micro-formulations
- SA3.3 *In vitro* and *ex vivo* demonstration of yeast fragment-based nanoformulations for oral delivery

1.3 Research Strategy and Rationale

To address these aims, we started by exploring the possibility of using flash-based self-assembly to mass-produce a variety of homogeneous NPs, as production scalability is the key to bridging bench-top fabrication to clinical translation. The first step is to design and fabricate the flash-based device. In 2003, a highly dynamic turbulent mixer was developed by Prud'homme and co-workers at Princeton[66]. The confined impinging jet mixer (CIJM) was designed to have two fluidic inlets in general. For the two-inlet CIJM, two pathways lead independent fluids to a small chamber where opposing streams containing solvent and non-solvent impinge to create turbulence. To maintain continuous flow, syringe pumps drive the streams from syringes into the mixing chamber. Prud'homme *et al.* calculated and specified design dimensions for their mixing chambers. In terms of device manufacturing, the main body of the CIJM can be made of stainless steel or a solvent-compatible thermoplastic such as polyformaldehyde or high-density polyethylene. CIJM was later adopted for polyplex complexation in which the polyanionic and polycationic materials have impinged with equal flow momentum[67]. Unequal flow momentum is needed for a more complex layer-to-layer formulation or other formulations involving multiple biomaterials. To overcome the equal flow momentum complications that are required for each channel in the CIJM, a more recent multi-inlets vortex mixer (MIVM) was developed to enable more flexible and dynamic mixing, which is required for nanoparticle coating[28]. Both CIJM and MIVM were re-designed and fabricated with modifications at Columbia in terms of the channel parameters and building materials. More importantly, computational fluidic dynamics (CFD) was utilized for flow simulation and estimation of flow shear stress in computer-aided design (CAD)-drawn MIVM designs[68–70]. The computer-based simulations can vastly reduce the cost of manufacturing and optimize the use of reagents. Different building materials, ranging from

polymers to acid-resistant stainless steel, were exploited for manufacturing in terms of device fabrication. Devices made of stainless can endure larger flow pressure, and the modified two-piece designs are more convenient for cleaning and assembly. Of note, we also explored the possibility to 3D-print some of our MIVMs, which could potentially lead to the mass production of these dynamic mixing devices.

After confirming the proper schematics of the MIVM designs and successfully manufacturing the flash-based devices, two and three-inlet CIJMs and four-inlet MIVMs were used to test the quality and the scalability of polyplex formulation. Current polymer-based and lipid-based NPs are formulated using non-standardized techniques. Methods like vortexing and manual mixing via pipetting, yield non-homogeneous products, and the batch-to-batch variations hamper them from clinical translation. Microfluidics-based techniques, including hydrodynamic focusing and parallel chips, could improve the nanoparticle polydispersity, but the yield of most of these devices still cannot meet the needs of clinical translation. To demonstrate the potential of a flash-based system in mass-producing polymer-based NPs in a consistent and homogeneous manner, different polymer-plasmid ratios for the poly(3-hydroxybutyrate-co-3-hydroxyvalerate) (PHBV) polymer-plasmid polyplexes were tested using a two-inlet CIJM device. After confirming the robustness of the flash-based system for PHBV polymer-plasmid polyplexes, the CIJM was also explored for formulating chitosan and TPP-based NPs. Based on the mixing principle of the FNC, which is a highly dynamic mixing process to form uniform polyplexes of both polycationic and polyanionic biomaterials through uniform diffusion under high Reynolds number chamber. Similarly, utilizing the highly turbulent mixing in the flash-based system allows us to explore the possibility of coating other biomaterials, such as lipids, to a nanoparticle surface. Besides natural polymers like chitosan, synthetic lipids are commonly and widely used

for a diverse range of biological applications as their physicochemical properties such as charge, fluidity, and composition can be modulated and adjusted.

Earlier studies of biomimetic strategies exploited synthetic or naturally occurring polymers to fulfill the need for various biomedical applications[71–73]. For example, liposomes are made of a lipid bilayer that resembles the plasma membrane, and their inner cavities can be loaded with synthetic and biological compounds[74–76]. In more recent studies, lipids were coated onto both organic and inorganic NPs for better particle stability, lower toxicity, and targeting effect with or without modified moieties[77–79]. The surface zeta potential can be tuned to meet the needs of different biological applications and administration routes. With advanced formulation methods such as microfluidics and dynamic mixing, lipo-polyplex, a nanocomplex consisting of a polymer core with a lipid shell, can be formed in a single and facile step[80]. The enhanced transfection efficacy of using the lipid-polymer system can be readily achieved[78]. In addition, inorganic and synthetic organic materials were combined as the hybrid formulation for therapeutic and diagnostic purposes[81].

In order to explore the feasibility, facile nature, and robustness of lipid coating using FNC, we first synthesized mesoporous silica NPs and optimized the lipid solution via balancing the ratio of DOPE, DSPE-PEG, and cholesterol. The advantage of using FNC for lipid coating a nanoparticle is that the entire process is facile and standardized; therefore, many conventional steps such as forming a liposome film through a solvent evaporation method can be skipped. Importantly, the FNC coating process minimizes batch-to-batch variation and operator error.

Furthermore, decorating a nanoparticle surface with biological substances, like a cell membrane, is an ideal top-down formulation process to take advantage of all that nature has endowed. Compared to the conventional bottom-up synthetic approach, harvesting cell

membranes directly from cells can preserve most of the cell surface's biological properties[27]. Moreover, different cell types have distinctive biological functions that can be exploited for different biological applications. Essentially, the cell membrane is a lipid bilayer with abundant proteins. The cell membrane resembles anionic lipids in many ways and is worth exploring for nanoparticle coating. In chapters two and three, these two projects were rationalized, executed, and discussed.

Nature has constantly been inspiring us for the advancement of technologies. Microbiomes, like yeast, have long been used in fermentation and food preparation. When designing an ideal drug and gene delivery system, biomimetic strategies can also be applied in the top-down formulation process, primarily for oral delivery. Safety is always the most crucial consideration when designing an oral delivery platform. The harsh gastrointestinal (GI) environment with low pH, various enzymes, and a thick mucosal layer are all problematic challenges for oral delivery systems[4].

Moreover, variability between individuals in their GI conditions presents another challenge that needs to be overcame when fabricating drug and gene delivery systems. An ideal oral delivery system should have adequate ability to withstand acidic and enzymatic degradation before reaching the target site[82]. Bioavailability should not be compromised, and the dosage of the oral system should not be toxic in the long term when usually patients are required to take the formulation over an extended period for many disease treatments. Baker's yeast, Saccharomyces cerevisiae, is a common strain that has been used in bakery and winemaking. The cell wall of the Saccharomyces cerevisiae is enriched with polysaccharides like β-1,3-glucan, chitin, and mannans. These polysaccharides are in the form of the pathogen-associated molecule pattern (PAMP), and they can be recognized by phagocytic cell pattern receptors, such as the dectin-1

receptor on the M-cell, and antigen-presenting cell (APC) types, like dendritic cells (DCs) and macrophages[16,83,84]. Loading active pharmaceutical ingredients (APIs) into the processed yeast or fragmenting the yeast cell wall to coat onto the desired NPs could be worthwhile strategies for enhancing oral delivery through the aforementioned cell types. These cells are hypothesized to facilitate the transport of yeast-based formulations into the lymphatic system and the systemic circulation. Chapter four describes the experimental design and results of the biomimetic yeast-based systems for oral drug and gene delivery.

All this work, taken together collectively, demonstrates that this thesis is a small step that intends to bridge the gap between bench-top research and clinical translation. The flash-based systems were designed and tested for formulating NPs in a facile, consistent, and scalable manner, which are crucial factors for future clinical translation. Utilizing the robustness of the flash-based system, lipid and cell membrane fragments were coated onto different NPs surfaces. This top-down biomimetic approach enables us to apply the coated NPs for various applications, especially cancer immunotherapy, owing to the preservation of most of the antigens on the cancer cell surface. The yeast-based oral systems were designed to enhance the transport of cargo to the lymphatic system and the bloodstream in a safe manner.

Chapter 2: Development of a FNC Platform and Evaluation of the Versatility of Flash-based Technology

Portions of this section are included in the following published conference proceeding and paper:

1. **Hu H**, Li M, Shao D, Yan H, Leong K. "Flash Self-Assembly for Lipid Coating of MSN and Nanotherapeutics" *BMES,* 2018
2. **Hu H**, Yang C, Li M, Tu Z, Mao HQ, Leong K. "Flash Technology-based Self-assembly in nanoformulation: Fabrication to Biomedical Applications", *Materials Today,* 2020, 1369-7021

2.1 Introduction

Nanoformulation, the construction of NPs and nanocomplexes, has profoundly impacted the chemical, food, medical device, and pharmaceutical industries[85]. Advances in nanotechnology, materials science, and biotechnology are now converging in the exciting field of nanomedicine. However, nanomedicine can fulfill its potential only if it can be produced at scale with precise control of nanoparticle properties, such as size, composition, and surface functionalization[86]. Self-assembly is an indispensable process in nanoformulation, and it has recent applications in cell-imaging, anti-inflammation, cancer therapies and many others[87–89]. As discussed in the earlier chapter, self-assembly has been performed using many different techniques, but many of these nanoformulation methods cannot fully satisfy biomanufacturing requirements due to nanoparticle heterogeneity, limited yield, and high batch-to-batch variation. A highly reproducible, scalable, and facile self-assembly technology is needed. Flash technology, which involves rapid mixing in CIJM or MIVM, facilitates self-assembly and formulation of

nanocomplexes or nanoprecipitates in a low-cost, high-throughput, and controllable manner is introduced[37,87]. The quality of the self-assembled nanoformulation can be maintained over the collection process in a manufacturing pipeline, which is vital for clinical translation. Flash self-assembly processes are conducted in micro- and milli-scale confined mixers. A variety of rapid mixers have been designed, some specifically for therapeutics or diagnostics. Nanoformulation mixers provide a dynamic mixing environment, with a high Reynolds number, essential for precise control of nanoparticle properties. Nanoparticle composition and surface modifications can be tailored by varying the configuration of the mixing chamber, flow rates of mixer inlets, and concentrations of solutions. Reproducibly generating NPs with well-controlled size and uniformity is critical for clinical translation[87,90]. Compared to batch processing methods such as dialysis, emulsification, and slow precipitation, flash self-assembly provides improved control over particle sizes, reproducibility, scalability, and throughput capacity by using continuous rapid mixing in a confined space. There are two major types of flash self-assembly: flash nanoprecipitation (FNP) and FNC. FNP uses dynamic mixing created by turbulent flow to stimulate nanoparticle nucleation and growth via solvent-induced supersaturation and polymer precipitation[87]. FNC exploits polyelectrolyte complexation-induced phase separation (**Figure 4**). In FNC, nanomaterials undergo self-assembly via physical interactions, such as electrostatic interactions and hydrogen bonding, and are formed within milliseconds or microseconds. The fluid dynamics of flash mixers in turbulent and laminar flow have been thoroughly studied in multiple fields using computational analysis and high-profile microscopy[15,39,40,91,92]. The

following sections will discuss the experimental characterization and computational simulation of flow behavior in FNP and FNC.

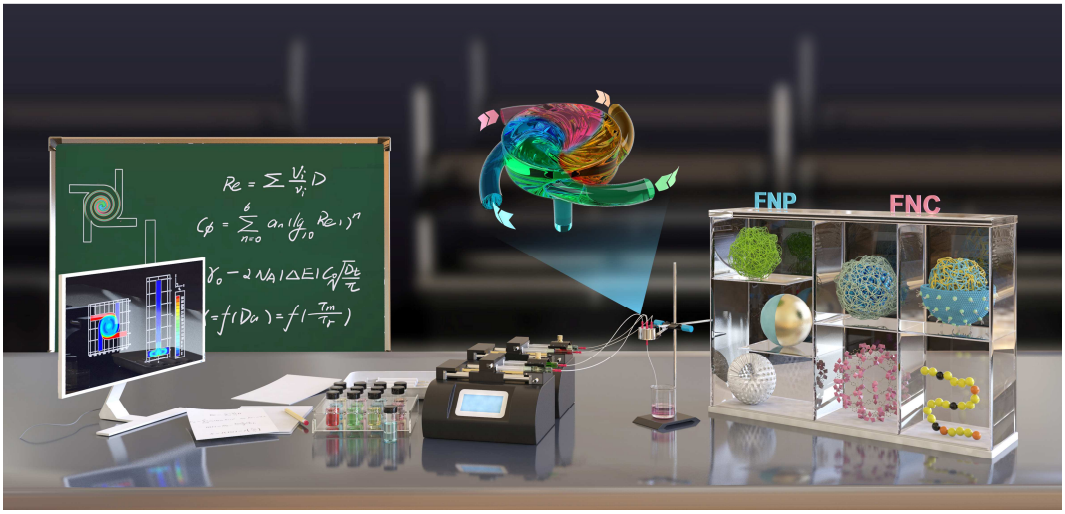

Figure 4: Schematic illustration of flash-based self-assembly procedures from computational modeling to different particle formulations.

2.2 Materials and Methods

Design and fabrication of FNC devices

All versions of the CIJM and MIVM are designed using AutoCAD for inlet and outlet dimensions. The computational-based simulation to analyze the mixing profile was performed using COMSOL. SOLIDWORKS was used to establish the 3D drawings of the CIJM and MIVM. Polyoxymethylene is used for two- and three-inlet CIJM fabrication. Two- and three-inlet CIJMs were manufactured at Johns Hopkins University's machine shop by Yizong Hu and Dr. Hai-Quan Mao, and devices were shipped to us as requested for courtesy. A regular and scaled-down version of the two-inlet CIJMs were manufactured at Columbia University's Mechanical and Materials Engineering machine shop. The three-piece unmodified four-inlet MIVMs were designed according to the previous report[15,39,92]. The three-piece MIVM is made of 304 stainless steel. We modified the design of the three-inlet MIVM to a two-inlet MIVM. Two methods were used to manufacture four-inlet MIVMs. First, we used a thermoplastic polyester, polyethylene terephthalate glycol (PETG), from ALL3DP to 3D print the two-part MIVM via a Formlabs 3L printer. For the stainless-steel version of the two-inlet MIVM, we used 316 and 316L stainless steel to manufacture the device. The stainless steel two-inlet MIVMs were manufactured at Holland Technology's and Southern China University of Technology's machine shop. All connecting parts and tubes were purchased from IDEX and McMaster-Carr. The 1 mL, 3 mL, 5 mL, 10 mL, and 20 mL syringes were purchased from Becton Dickinson (BD). The digital pumps were purchased from Harvard Apparatus.

Preparation and characterization of flash-based self-assembled nanoformulations

The two-inlet CIJMs, three-inlet CIJMs, and four-inlet MIVMs were used to perform the self-assembly of polyplexes. The pCas-9 plasmid was obtained from Dr. Yeh-Hsing Lao at Columbia University. Poly hydroxybutyrate-co-hydroxyvalerate (PHBV), chitosan, and triphenyl phosphate (TPP) were purchased from Sigma-Aldrich. For preparing PHBV-pCas polyplexes, various polymer to plasmid ratios (w/w 20, 10, 5, 2, 1, 0.8, 0.4, 0.2, 0.1, 0.05) were tested under a flow rate of 5 mL/min using a regular (V1) version of the two-inlet CIJM. The size and zeta potential of the polyplexes were recorded using a Malvern 2.0 Zetasizer. For chitosan-TPP nanoparticle preparation, two-inlet CIJMs, three-inlet CIJMs and four-inlet MIVMs were used to compare the nanoparticle size under different flow rates. Dynamic light scattering (DLS) was performed on the Malvern 2.0 Zetasizer to characterize the nanoparticle size. Nanoparticle solution was dropped onto a copper mesh without particle staining for transmission electron microscopy (TEM) observation on a FEI Talos F200X S-TEM.

Preparation of lipoMSN

To coat the MSN with liposomes with bulk mixing method, 200 µL of 1 mg/mL liposome was added directly to 200 µL of 1 mg/mL MSN. The solution was vortexed immediately for 10 seconds and then shaken at 500 rpm at 4°C for 30 minutes. Excess liposomes were removed via centrifugation at 10,000 g for 12 minutes, the supernatant was discarded, and lipoMSN was resuspending at the desired concentration. In order to load cargo like small biomolecules, the cargo was diluted with 20 µL of molecular biology grade water, added to the MSN solution, vortexed immediately for 10 seconds, and then shaken at 500 rpm at 4°C for 1 hour. Afterward, the MSNs were coated with liposomes as described above, and excess liposomes and cargo were removed by centrifugation at 10,000 rpm for 30 minutes and overnight

dialysis. For coating lipids onto MSN using FNC, MSNs and lipids were prepared and well dispersed in Milli-Q water and ethanol, respectively. First, the combined lipid solution received adequate sonication treatment. Then, MSNs and lipid solutions were introduced into the different inlets of the MIVM in an adjacent flow manner, respectively. Molar ratios of 36.83/47.78/0, 44.3/49.16/2.26, 46.99/47.78/1, 60.78/35.76/2.04, 60/39/1, 60/38/2, 60/37/3 of the DOPG/cholesterol/DSPE-PEG2000 were tested. A total of 90 mL/min flow rates were applied to prepare lipid-coated MSNs solution. A flow rate ratio of 1-3 was applied to the lipid solution inlet (11.25 mL/min) and MSNs solution inlet (33.75 mL/min). The efflux was collected and allowed to settle, lyophilized, or stored before further coating characterization.

Synthesis of liposomes through the thin-film hydration method (adapted from the protocol provided by Kate Ho and Jing Gong)

Lipid was synthesized into liposomes using the following method. Briefly, DOPE was mixed with cholesterol and DSPE-PEG2000 (Avanti Polar Lipids) at a molar ratio of 60:35:5. Anionic lipid, cholesterol, DOPE, and half of the DSPE-PEG2000 were mixed in a chloroform solution in a 0.5-dr vial. The organic solvent was evaporated under vacuum and further dried overnight to form a thin film on the vial. The lipid film was hydrated using a mixed solution of ethanol/sodium acetate buffer (200 mM, pH = 5.2, v/v = 9:1). The above solution was added dropwise to an aqueous solution of the other half of DSPE-PEG2000, and the resulting solution was incubated at 37°C for 30 minutes before subjecting to dialysis against water or phosphate-buffered saline (PBS) in 3500 molecular weight cut-off (MWCO) cassettes (Pierce/Thermo Scientific). DOPE, cholesterol hemisuccinate, and DSPE-PEG with PEG molecular weight 2000 (880128P, Avanti) were combined and dissolved in chloroform at concentration of 25 mg/mL.

The mixed lipid solution was then diluted 10 x and aliquoted into scintillation vials. The chloroform was evaporated in a fume hood for 3 hours and transferred to a vacuum baker at room temperature overnight to evaporate any residual chloroform. The lipid was frozen at -20°C for future use. To prepare liposomes, the lipid vial was settled at room temperature before it was rehydrated with 1 mL of Milli-Q water or PBS solution. The liposome solution underwent 10 cycles of the mini extruder (Avanti) with a 200 nm polycarbonate membrane. DLS was applied to test the resulting liposome size and charge. The liposome product was kept at 4°C before use.

Synthesis of MSNs

MSNs were synthesized via a modified sol-gel method previously published, using etyltrimethylammonium tosylate (CTAT) (Vulcan Chem) as a template, and TEOS was used as co-silica sources[93]. Briefly, 0.6 g CTAT, 0.15 g triethanolamine (TEAH3) (Sigma Aldrich) and 40 mL deionized (DI) water were stirred at 80°C for 30 minutes with a stirring speed of 1,000 rpm. Then, a solution of 4.0 g of TEOS (Sigma Aldrich) was added dropwise to the solution, with the resulting solution stirred at 80°C for another 4 h with a stirring speed of 1,000 rpm. These products were then collected via centrifugation for 20 minutes at 10,000 g then washed through resuspension in ethanol followed by centrifugation three times. They were then refluxed in an ethanol solution of 1% w/v NH_4NO_3 for 12 h. Finally, the MSNs were collected, washed, and dried for subsequent functionalization or loading.

Functionalization of MSN

Amine modification of MSN

Approximately 200 mg of the synthesized MSNs were resuspended in 80 mL of ethanol under sonication for 20 minutes. This solution was stirred at 80°C for 3 h and then cooled to room temperature. Next, 200 μL of 3-aminopropyltriethoxysilane (APTES) (Sigma Aldrich) was added to the solution and the mixture was stirred at room temperature for 1 h. Finally, the solution was refluxed at 80°C for 12 hours before being collected via centrifugation, washed with DI water, and lyophilized for storage.

Carboxylation of MSN

200 mg of the synthesized MSNs were resuspended in 80 mL of ethanol under sonication for 20 minutes. This solution was stirred at 80°C for 3 h and then cooled to room temperature. Next, 1.2 grams of succinic anhydride (Sigma Aldrich) and 80 μL of triethylamine (TEA) (Sigma Aldrich) were added to the solution and the mixture was stirred at 50°C for 24 h. Finally, the solution was collected via centrifugation, washed with DI water, and lyophilized for storage.

Flow cytometry determination of uptake

To determine the uptake of doxorubicin (DOX)-loaded and lipid-coated MSNs, we treated the cells of different MSNs and then performed flow cytometry 4 h later. HeLa cells were maintained in a collagen-coated tissue culture plate, treated with a Dulbecco's Modified Eagle Medium (DMEM) Medium (ATCC) supplemented with 10 % fetal bovine serum (Sigma Aldrich) at 37°C with 5 % CO_2. Cells were seeded at 100,000 cells/well for a 24-well plate and cultured 24 h before use. Membrane-coated MSNs with fluorescence-labeled cargo were added to the cell-culture well with Opti-MEM (500 μL/well) and was maintained at 37°C for 4 h. Then,

the cells were washed with cold PBS and trypsinized into a single-cell suspension. The cells were then subjected to flow cytometric analysis using BD Fortessa flow cytometry.

Computational fluid dynamics (CFD) and computational construction of the MIVM

The commercial CFD solver Ansys FLUENT ver. 19.2 was used to approximately solve the Navier-Stokes equations. A turbulence model of κ-ε was adopted to capture the gradually varying flow from the inner region to the interior lumen. The turbulence intensity was set to 1. A hybrid mesh consisting of tetrahedral grids inside and a prismatic boundary layer was generated using the ANSYS meshing system in ANSYS workbench, which contained 166416 cells and 393820 grids with an inflation layer with eight layers and a growth rate of 1.1. The liquid used in the simulation was water with a density ρ = 1000 kg·m^{-3} and a dynamic viscosity μ=0.8904×10^{-3} Pa·s. The shear stress transport eddy-viscosity model was adopted to capture the WSS distribution. We set the spatial discretization as second-order upwind and the truncation error was also set to second-order. The lumen wall was set to be rigid with a no-slip boundary condition. A boundary condition strategy was designed with four inflow inlets and a pressure outlet in the mixer. In this study, we used a steady inflow boundary condition with mass flow rates of 0.0005, 0.0015, and 0.0025 kg/s, and a 0-pressure outflow condition.

2.3 Results

SA1.1 Design and manufacture FNC devices

Flash self-assembly processes were conducted in micro- and milli-scale confined mixers. A variety of rapid mixers have been designed, some specifically for therapeutic or diagnostic formulations[15,91,92]. Dynamic mixing with the turbulent mixing environment is important for precise control of nanoparticle properties. Importantly, varying the mixing parameters, like flow rates and solution concentrations, can tailor nanoparticle composition and surface modifications[30]. The CIJMs designed at Princeton University often have two or three fluidic inlets[39]. For the two-inlet CIJM, two pathways lead to a small chamber where opposing streams containing solvent and non-solvent impinge to create turbulence (**Figure 5**). To maintain continuous flow, syringe pumps drive the streams from syringes into the mixing chamber. Design dimensions for the mixing chamber were primarily specified by Johnson and Prud'homme[15,39,92]. The main body of the CIJM can be made of stainless steel or other solvent-compatible thermoplastics or high-density polyethylene. The CIJM is a powerful tool for producing nanoformulations in the millisecond range through supersaturation and diffusion-induced electrostatic interaction. However, CIJM geometry limits the ratio of solvent to non-solvent due to the requirement of opposing streams to have equal momentum in mixing. This requirement restricts the use of CIJM to hydrophilic solutes and a specific range of solvent-to-solute ratios. To overcome the CIJM requirement of equal fluidic momentum, a multiple inlet vortex mixer (MIVM) was designed to allow for unequal solvent-to-nonsolvent ratio mixing in a scalable manner. The concept of the MIVM is that momentum from each stream contributes independently to drive micromixing in the chamber; therefore, it is possible to have larger differences in flow rates between flow inlets while maintaining dynamic micromixing. MIVMs

used in flash-based self-assembly generally consist of components manufactured using stainless steel and assembled with syringe adapters. MIVM is designed to be easily disassembled and cleaned. 3D printing can be used to fabricate MIVMs, and a 3D-printed MIVM was used to formulate lipid-polymer hybrid NPs for biological applications. The MIVM design allows the combination of immiscible solutions, providing additional flexibility to the choice of materials for nanoformulations.

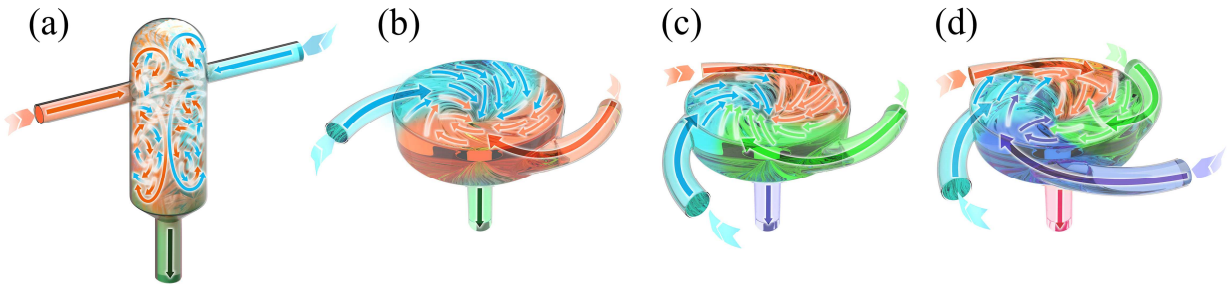

Figure 5: Geometries of mixers used in flash nanoformulation processes (a) CIJM, (b) two-inlet MIVM, (c) three-inlet MIVM, (d) four-inlet MIVM.

Before manufacturing the flash device, we explored different flow parameters in terms of the inlet dimensions and shear stress. A computational-based MIVM device was used to ensure that the flow is dynamic and highly turbulent under specific dimensions of the inlet and mixing chamber. First, the chamber wall shear stress (WSS) was plotted, corresponding to different inlet heights and widths (**Figure 6a**) in order to determine the ideal dimensions to maximize turbulent mixing with the highest wall shear stress. Then, a Computational Fluidic Dynamics (CFD)-based model was constructed based on the selected dimensions to calculate the flow velocity for the entire device (**Figure 6b-d**). From here, we began the CAD drawings and SOLIDWORKS constructions of the two-inlet, three-inlet CIJM, and four-inlet MIVM (**Figure 7a-d**). The

dimensions of the CIJM flow channel and the mixing chamber were based on the previously reported geometries[92]. The material used for CIJM fabrication is polyoxymethylene (POM), owing to its lightweight and acid-resistant properties (**Figure 7e, f**). However, the single-pieced CIJM device cannot be opened up for thorough cleaning and therefore is more susceptible to bacteria accumulation, clogging, and erosion. For higher flow rate conditions, stainless steel (stainless steel 304) was selected as the building material, and the device consisted of three individual pieces according to the previous fabrication. Then, we modified the three-piece MIVM to a two-piece device to reduce raw building materials (stainless steel 316L) and improve the ease of device cleaning (**Figure 7i**). The CAD drawings were then used as the reference for SOLIDWORKS drawings before fabrication in a mechanical machine shop or by 3D printing. We tried to 3D print the MIVM device with glycol-modified polyethylene terephthalate (PETG), a thermoplastic polymer with high chemical resistance and durability that is a commonly used material in water bottle manufacturing (**Figure 7h**). To scale up the production of nanoformulations prepared by MIVM, we also designed and fabricated a slightly larger MIVM device with a broader inlet and mixing regime that can cope with a larger flow rate without

compromising the k-length and patterned turbulent flow.

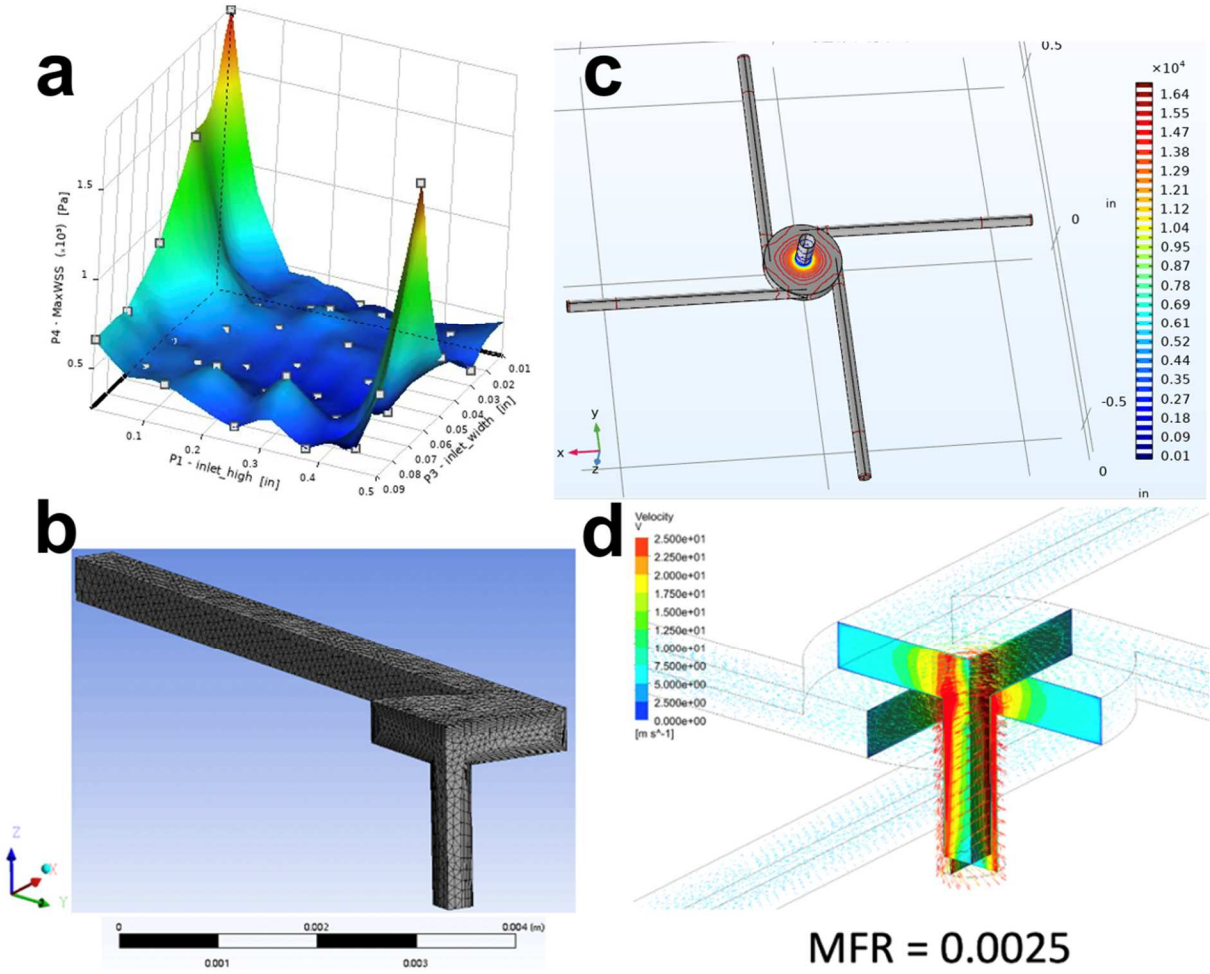

Figure 6: Construction and the CFD simulation of a MIVM. (a) MaxWSS plot of the device channel height and width versus wall shear stress, (b) construction of a quarter of MIVM model for shear and velocity analysis in the CFD, (c) analysis of the flow velocity within the MIVM, and (d) analysis of the mass flow rate at 0.0025 kg/s within the MIVM.

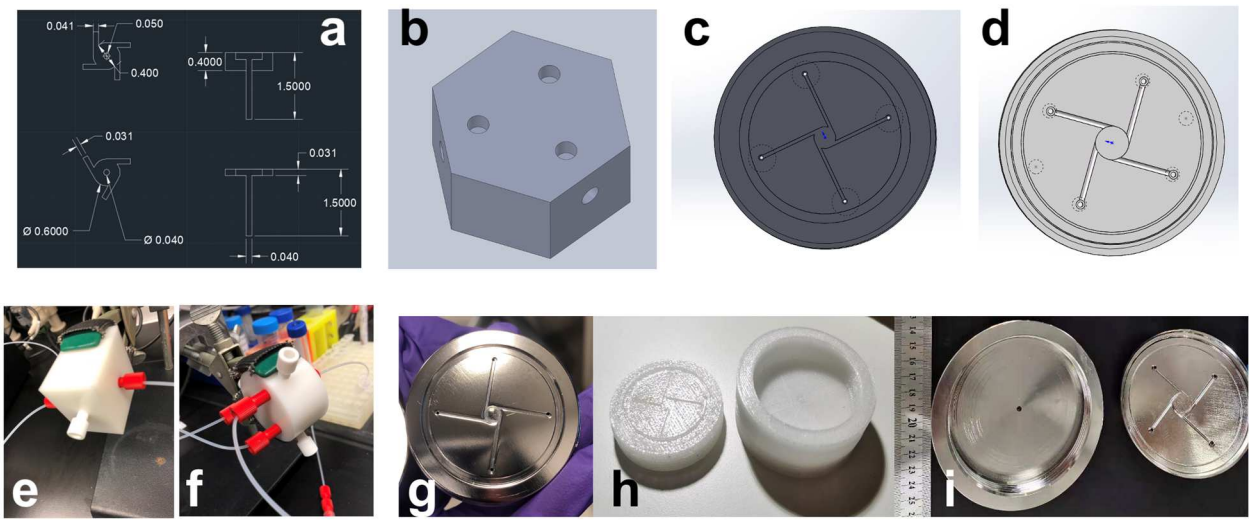

Figure 7: Design and fabrication of the CIJM and MIVM. The AutoCAD drawing of (a) 4-inlet and 3-inlet MIVM, and the SOLIDWORKS construction of (b) 3-inlet CIJM, (c-d) 4-inlet MIVM, picture of manufactured (e) POM-based 2-inlet CIJM, (f) POM-based 3-inlet CIJM, (g) stainless steel-based 4-inlet MIVM, (h) 3-D printed PETG-based 4-inlet MIVM, and (i) two-piece layout of a stainless steel-based 4-inlet MIVM. (Devices show on figure 7e and 7f were obtained from Johns Hopkins University)

SA1.2 Prepare and characterize flash-based self-assembled nanoformulations

FNC is a kinetically controlled mixing process. The dynamic mixing process can produce diverse nanoformulations with controlled size, high drug loading, and high encapsulation efficiency in a continuous and scalable manner[32,94,95]. To achieve uniform phase separation and nanoformation, a CIJM or a MIVM is used to facilitate rapid and efficient turbulent mixing of two or more polyelectrolyte solutions. For FNC, phase separation is induced by polyelectrolyte complexation, and many kinds of non-covalent and covalent interactions can be employed in fabrication, including ionic, hydrophobic, hydrogen bonding, metal coordination, and the specific ligand or host-guest interactions. To test the robustness of FNC formulating, we first evaluated the polyplex nanoformulation by CIJM. We selected PHBV, poly(hydroxybutyrate-co-hydroxy valerate) as the polycation, and pCas-9 plasmid as the polyanion to form polyplexes (**Figure 8**). We explored different polymer to plasmid w/w ratios in forming the polyplexes with

a fixed flow rate using a two-inlet CIJM. The size of the polyplex decreases along with the polymer-plasmid ratios. The surface charge of the polyplex also decreases as an indication that more plasmids were encapsulated into the polyplex. At a 0.4 polymer-to-plasmid ratio, the size of the polyplex is less than 100 nm, and the polydispersity index (PDI) of the corresponding ratio is around 0.15, which is the indication of the good size uniformity of the formulated polyplex. Importantly, at the 0.4 polymer-to-plasmid ratio, the surface charge of the polyplex is close to neutral, which may be ideal in crossing the mucosal layer on the epithelium. For future studies, we could further optimize the ratio for plasmid loading without compromising the ideal size of the polyplex. Also, with the aid of computational power and control of the flash system, we may unravel how compactly or how much of the plasmid can be specifically loaded onto a single polyplex. In addition, we also tested the polyplex formulation using a commonly used cationic biomaterial, chitosan with a polyanion, tripolyphosphate (TPP). We compared the produced polyplexes in terms of their sizes at different flow rates using a two-inlet, a three-inlet CIJM, and a four-inlet MIVM. Overall, the size of the polyplexes prepared by all three devices decreases with increasing the flow rate. At flow rates greater than or equal to 3.5 mL/min, the polyplex size stagnated, and so did the PDI for all formulations. We hypothesize that the two-inlet CIJM has a certain limitation in mixing this particular nanoformulation in terms of the dynamic and homogeneous mixing profile. Therefore, we further tested the chitosan-TPP formulation with higher flow rates using our manufactured MIVM. We tried three different flow rates (10 mL/min, 15 mL/min, 20 mL/min). We found that the size further decreased to around 50 nm and the PDI was less than 0.1, which indicates superb particle homogeneity. More and repeated studies are necessary to confirm the superior capability of the four-inlet MIVM in producing homogeneous polyplexes.

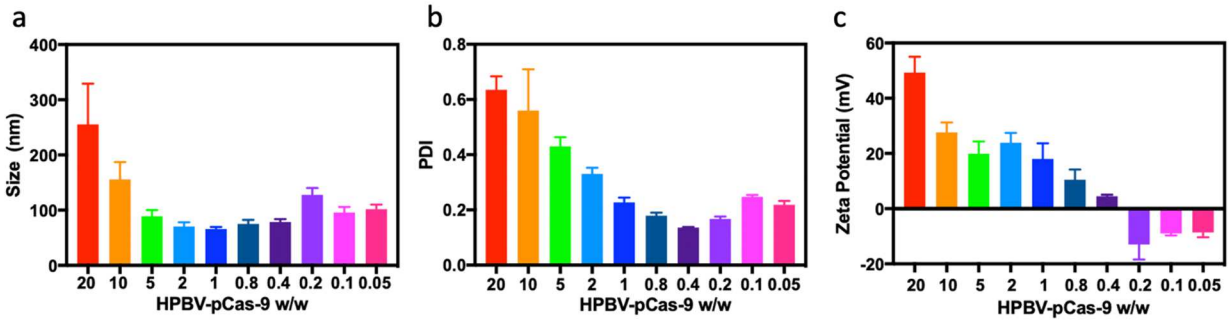

Figure 8: Characterization of the CIJM formulated HPBV polymer-plasmid polyplexes. DLS analysis of polyplex (a) size, (b) PDI, and (c) zeta potential of different polymer-plasmid ratios.

SA1.3 Prepare and characterize flash-based lipid-coated nanoformulations

FNC can prepare nanoformulations with diverse characteristics in a sequential nanoparticle formation process followed by surface modification[28,95–97]. FNC allows rapid, scalable, and organic solvent-free fabrication of diverse NPs with well-controlled structure, composition, size, surface properties, and a more expansive range of potential applications[31–33,94]. Lipids and liposomes have widely been used for drug and gene delivery. Recent studies used FNC to coat lipids onto solid drug NPs for better particle stability and prolonged particle circulation time[28]. MSNs are versatile and efficient cargo carriers, and they have been used for several applications such as cancer therapeutics, diagnostics, and theranostics[85]. The pore size of the MSNs can be tuned for accommodating small molecules and macromolecules. The backbone of the MSNs can be synthesized as stimuli-responsive and biodegradable for better biocompatibility and safety. Herein, we choose a combination of lipids, consisting of anionic lipid DOPG, cholesterol hemisuccinate, and DSPE-PEG2000 to coat onto the carboxyl-modified MSN surface (**Figure 9**). Although both MSNs and lipids have negative surface charges, the electrostatic difference allows the lipid to coat onto the MSN surface. Conventionally, researchers often prepare the liposomes via the thin-film hydration method for lipid coating onto a solid core (organic, inorganic, hybrid), which usually takes multiple days to complete the

preparation and coating steps.[79]. However, utilizing the FNC technique, which is a single-step and facile way to achieve NPs coating, vastly reduces cost and time. First, we explored the effect of different flow rates on the prepared lipid-MSN formulation size. We found that with a 24 mL/min flow rate, the lipid-coated MSN formulation has the smallest tested size (70 nm) and the lowest tested PDI (0.15). After coating, a layer of lipid (8-10 nm) was observed on the surface of the MSN shown in **Figure 10**. The bare MSNs exhibit -40 mV surface zeta potential, while the lipid has -20 mV zeta potential tested via DLS. The lipid-coated MSN shows the zeta potential closest to the zeta potential of lipids, suggesting a complete coating. TEM images of the lipid-coated MSN show that the surface of the MSN is covered by a lipid layer which is different in electron conductivity from the bare MSN. The lipid-coated MSN solution is milky and opaque (**Figure 10a**). Importantly, based on the DLS data shown in **Figures 10b and 10c**, the size of the flash-based lipid-coated MSNs tends to become smaller when we apply a higher flow rate. This result suggests that turbulent flow is essential for a complete coating because a complete coating of MSNs improves the colloidal stability of NPs in the solution and decreases their likelihood to aggregate into larger particle clusters. For therapeutic purposes and a proof-of-concept, we included DOX in the mixing process (**Figure 11**). We tested the encapsulation efficacy and the loading level of the DOX in the lipid-coated MSN nanoformulation using various DOX input amounts. We found a DOX amount of 0.125 mg to be effective with a relatively high encapsulation efficacy (79%) and without compromising the drug loading level (15%) (**Figure 11b**). We selected this drug concentration to evaluate the drug releasing profile in pH 7.4 and pH 5.5 solutions. Interestingly, we observed a slightly delayed DOX release from the lipid-coated nanoformulation in both pH conditions, and this result may suggest that the lipid bilayer serves as a physical barrier for water penetration and drug diffusion (**Figure 11c**). We also performed

an *in vitro* cellular uptake study of the bare MSN and lipid-coated MSN in HeLa cells (**Figure 11a**). We observed that both bare and lipid-coated MSNs were efficiently endocytosed by the HeLa cells. Although some of the MSNs and the lipid-coated MSNs were observed in the lysosome, the majority of NPs were presented to the cytoplasm for cargo release in the cancer cells. To compare the DOX-free molecule to the DOX-loaded MSNs and lipid-coated DOX-loaded MSNs, we also performed confocal imaging to see the DOX-associated fluorescence in HeLa cells (**Figure 11d**) to compare the uptake efficiency of the DOX with or without a nanoparticulate carrier. Furthermore, cytotoxicity is important to consider when evaluating the efficiency of a therapeutic system. We compared the *in vitro* cytotoxicity of the DOX-free drug to the DOX-loaded lipid-coated MSN group for 12 and 24 h (**Figure 12**). Based on the results, the DOX-free drug has a higher IC50 value than the DOX-loaded lipid-coated MSN group. We qualitatively observed a higher uptake and lower cytotoxicity of the DOX-loaded lipid-coated MSNs, compared to the free DOX, in the HeLa cells, and that this may be due to the delayed release of the DOX molecule from the MSNs. Moreover, as the MSNs used in this system are not biodegradable, the safety and long-term therapeutic effects of this lipid-coated system need to be further assessed. Nevertheless, this study is a proof-of-concept using flash-based self-assembly to prepare lipid-coated MSNs for cancer therapeutics. The facile and robust process of flash-based nanoformulation has the potential to overcome the challenges of limited production and batch-batch variation.

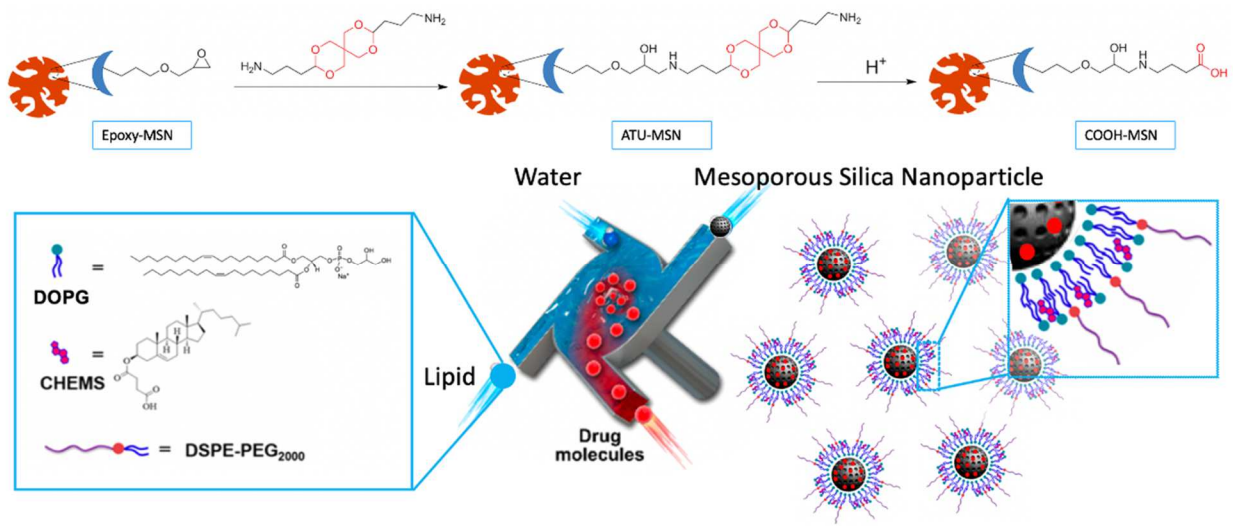

Figure 9: Schematic illustration of MSN modification and FNC-based lipid coating of modified MSN.

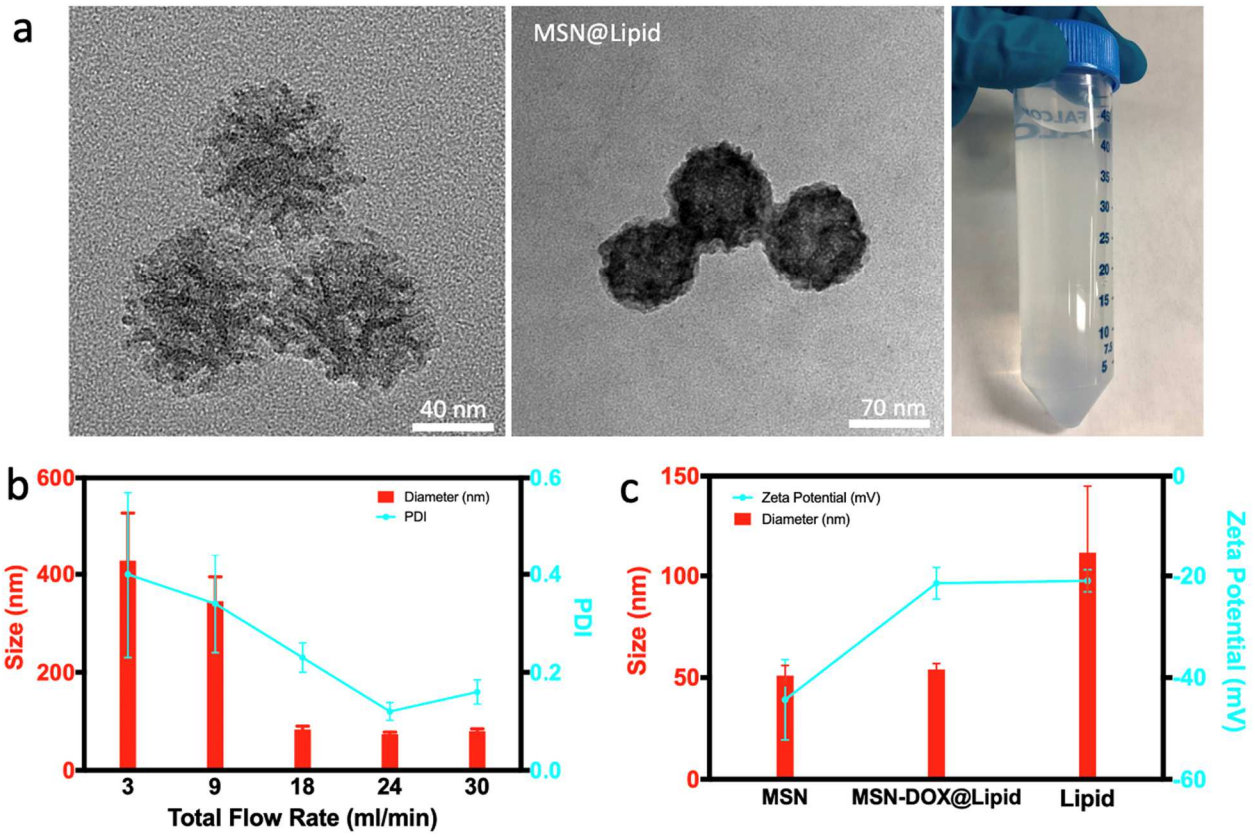

Figure 10: Characterization of lipid-coated MSNs. TEM images of (a) bare carboxyl-modified MSNs (left), lipid-coated MSN (middle), and a 50mL tube contains lipid-coated MSN solution

(right) (b) DLS analysis of size and PDI of lipid-coated MSN using different flow rates, (c) DLS analysis of size and zeta potential of the bare MSN, lipid-coated MSN, and lipid only.

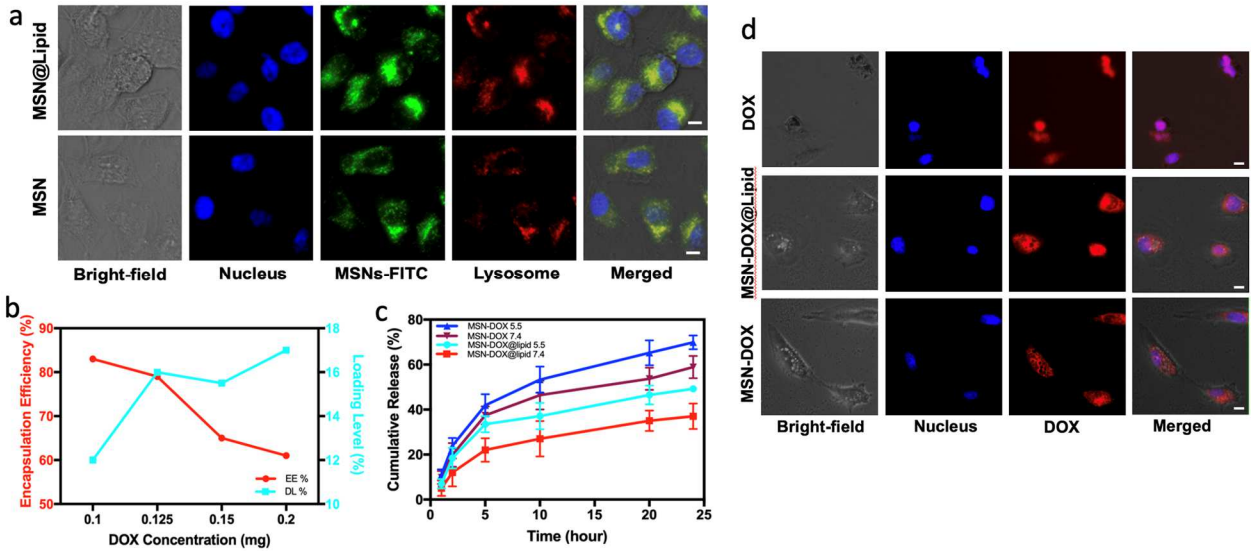

Figure 11: *In vitro* uptake study. (a) Free MSN and MSN-lipid (cell nuclei were stained by DAPI; green represents MSN by FITC; red presents lysosome by Lysotracker-Red), (b) encapsulation efficiency, EE% and Drug Loading Level, DL% of DOX laden lipid-coated MSN, (c) drug encapsulation and release profile of MSN-DOX and MSN-DOX@lipid at different pH values (5.5 and 7.4) at 37°C, and (d) confocal images of free DOX, MSN-DOX and MSN-DOX@lipid cultured with HeLa cells (cell nuclei were stained by DAPI; red represents DOX by self-fluorescence).

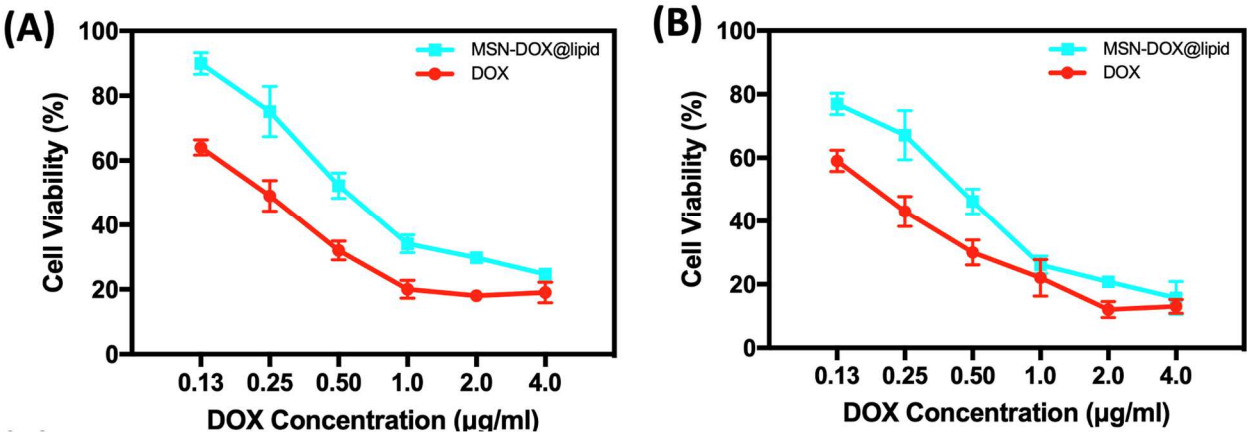

Figure 12: Quantitative analysis of cytotoxicity free DOX and MSN-DOX@lipid for HeLa cells at (a) 12 h and (b) 24 h of incubation.

2.4 Discussion

This chapter discussed the background, rationale, experimental design, and results revolving around a novel and facile nanoformulation technology called flash-based self-assembly. To build a MIVM, the device parameters were explored and optimized through CFD simulations before manufacturing it through machine shop fabrication or 3D printing. Importantly, a facile, fast, and single-step self-assembly process was demonstrated to formulate plasmid-based polyplexes and lipid-coat drug-loaded MSNs in scalable manners. Further, we compared and evaluated the quality of lipid-coated MSNs by FNC with conventional bulk mixing. We also demonstrated an ideal drug-releasing profile by comparing stability and drug-releasing behaviors between the MSN fabricated via FNC and the conventional bulk mixing methods.

Further, the drug loading efficiency and cellular uptake of lipid-coated MSN made via FNC were studied. Flash-based self-assembly using rapid mixing technology provides a more versatile, scalable, reproducible, and robust approach to nanoformulation than traditional self-assembly techniques such as bulk mixing. Also, flash-based self-assembly has the potential to reduce the amounts of reagents consumed, while improving the homogeneity and stability of the product. Despite tremendous progress, challenges remain and limit the broader application of flash-based nanofabrication. For example, there is a need to better understand the relationship between flash-based processes and nanoformulation performance. Computational modeling and *in silico* experiments can also bring us trenchant insights into nanoformulation design and particle interactions. Also, developing a transparent device might be ideal for real-time visualization of the nanoformulation process. Developing MIVMs for scaled-up production of nanoformulations for clinical translation and developing special scaled-down versions of the

MIVMs for preserving precious reagents and personalized medicine are also important. New devices with different designs or connections tailored to the self-assembly-based fabrication of specific nanomedicines are needed. This endeavor will require a better understanding of how driving forces play roles in flash-based self-assembly. It is also critical to consider the cost factors at the front end of clinical translation, from material design to large-scale production. Other crucial factors such as efficiency, stability, and safety must also be considered. New flash-based nanomedicines are expected to be fabricated using FNC via single and mixable driving forces. More effective and scalable self-assembly strategies in this multidisciplinary field will lead to more flash-based nanomedicines emerging in the coming decades.

Chapter 3: Development of Cell Membrane-based Nanoformulations for Cancer Immunotherapy

Portions of this section are included in the following published paper and PCT patent:

1. **Hu H**, Yang C, Zhang F, Li M, Dawulieti J, Yan H, Xiao Z, Sun W, Shao D, Leong K. "A Versatile and Robust Platform for the Scalable Manufacture of Biomimetic Nanovaccines", *Advanced Science*, 2021, 2002020
2. Scalable and Facile Cell-membrane-coating Technology for both Positively and Negatively Charged Particles PCT/US2021/017823 (in PCT)

3.1 Introduction

Biomimetic strategies are critical for developing sophisticated nanoparticle-based therapeutics to overcome biological barriers[71]. Cell membrane coating technology offers a promising solution to the challenges of therapeutic delivery by integrating the biological features of cell membranes with the functional versatility of nanomaterials[27]. Cell membrane coating involves covering a synthetic nanoparticle with a naturally derived cell membrane layer to form a biomimicking ensemble. These biomimetic formulations have shown advantageous physical properties, such as improved stability and longer circulation times, and intrinsic functionalities inherited from the donor cell source, such as toxin neutralization, homologous targeting, and immune invasion[27,98,99]. However, producing regulatory agency-approved cell membrane-coated nanomaterials requires an additional level of manufacturing sophistication. Current approaches to fabricate cell membrane-coated nanomaterials rely on two main strategies: extrusion and sonication[27,100]. Extrusion produces homogeneous coatings and uniform sizes, but it is prohibitively time-consuming; sonication offers a facile approach to produce a sufficient

product, but the quality control can be compromised in several ways and the coating outcomes may vary dependent on the protocol[44,101–103]. The difficulty of fabricating cell membrane-coated nanomaterials in a facile, large-scale, and reproducible manner restricts their prospects for clinical and industrial translation. Standardized formulation techniques are necessary to ensure that these biomimetic formulations can be produced in a timely manner, with minimal batch-to-batch variation, and with good manufacturing practices. Fundamentally, the challenge is to develop an efficient and reliable cell membrane coating process.

To surmount these obstacles, we took advantage of a recently developed technology, FNC, which was also discussed in Chapter 2. FNC involves turbulent mixing and self-assembly of nanomaterial ingredients in defined microchambers. It can be applied to manufacture a variety of nanoformulations for therapeutic and bioimaging applications[28,29], and provides a robust platform that may expedite the translation of nanotherapeutics. FNC exploits the dynamic mixing of nanocomposites that undergo self-assembly via physical forces such as electrostatic interactions, in which case charged nanomaterials assemble to form NPs or to modify a NP surface[67,95,104,105]. Uniform lipid-coated NPs have been fabricated using FNC by optimizing the lipid/NP mixing ratio, flow rate, and lipid composition[28,41]. We hypothesized that FNC could be applied to the mixing of cell membrane fragments and synthetic backbone materials for the robust and scalable production of cell membrane-coated NPs (**Figure 13**). In addition, by using the MIVM, the kinetic energy of multiple inlet jets can be controlled to transport cell membrane fragments and synthetic backbone materials into regions of small turbulent eddies and intershearing layers for better flow convection and hence, faster coating[106–110]. The mixing ratio and flow rate can then be tuned to produce a homogeneous coating.

Figure 13: Schematic illustration of FNC-based cell membrane coating in comparison to the bulk-sonication coating method.

3.2 Materials and Methods

Molecular dynamics simulation

The investigation of anionic lipid interaction with the cationic silica nanoparticle was based on the MARTINI force shield, while the adopted dissipative particle dynamic (DPD) model was also performed as the small scaled reference for dissipative lipid aggregation analysis[2,68,111]. Both neural and anionic lipid molecules were used to simulate the lipid composition of cell membrane fragments. The lipid composition was balanced (2000 out of 6600 lipid molecules possess negative charges) and collectively manifested in an anionic manner. The silica NP was constructed using 38882 coarse-grained particles into a nanosphere. Every other silica (Si-) motif was endowed with one amine group for silica NPs (based on our experimental protocol for amine-modified di-selenide MSN) and rendered to the cationic surface. A cubic box with a PPP boundary and a size of 300 × 300 × 300 nm^3 was created. Then, 6600 lipid molecules and water are randomly filled into the system. The interaction between the silica NPs and lipid, and theoretical analysis were adopted from the solvent-free MD model[2,103,112–114]. The unit command used in the simulation is Lennard-Jones (LJ) and the heat bath used is based on Langevin calculation in LAMMPS. The simulation was run using NVT condition with a temperature of 300 K. Timestep was set to 40 ns per timeframe. All visualization was created using the dump command and run on the software Ovito Pro 3.0.

Derivation of cell membrane and characterization of cell membrane-coated nanoformulations

Cell lines (RAW 264.7, B16-F10, Caco-2, and HepG2) were maintained in DMEM supplemented with 10% fetal bovine serum (FBS) and 1% antibiotic/antimycotic solution and

incubated at 37°C with 5% CO_2 in T175 tissue culture flasks. Cells were trypsinized, washed and suspended within PBS. To obtain the derived cell membrane, a sequential centrifugation method was applied after lysis and homogenization of the cells[115,116]. The resulting membrane pellets were washed with nuclease-free water and suspended in either 1X PBS or nuclease-free water. The total membrane protein contents derived from different cell lines were quantified using BCA protein assay kits separately. Derived cell membrane vesicles were stored in nuclease-free water or PBS solution at -80°C until further use.

All particles and cell membrane fragments were prepared and well dispersed in independent solutions. First, the cell membrane vesicles received adequate sonication treatment. Then, particle solutions and cell membrane fragments were introduced into the different inlets of the MIVM. A 90-150 mL/min flow rate was applied to prepare the membrane-coated particle solution. RAW 264.7, B16-F10, Caco-2, HepG2 cell membranes were used to coat MSNs with both small and big pores. HEK 293 cell membranes were used to coat silica dioxide microparticles with the membrane/particle mass ratio of 1/2. Caco-2 membrane was used to coat PEI-DNA nanocomplexes with the membrane/particle mass ratio of 1/2. For the surface coating of cationic MSN experiments, RAW 264.7 and B16-F10 membranes were applied with different membrane/MSN mass ratios. The efflux was collected and allowed to settle or stored before further coating characterization. For cell membrane coating NPs through the bulk sonication method, cell membrane vesicles and particle cores at various mass ratios were mixed, pipetted, and sonicated together. B16-F10 membrane was used for all *in vitro* and *in vivo* studies. Coating efficacy was evaluated based on the membrane protein concentration of the membrane-coated product. Membrane-coated MSNs by FNC were compared with the bulk-sonication method (varied sonication time). Bare MSNs were used as the negative control and cell membrane

vesicles served as the positive control. The size and zeta potential of bare and membrane-coated particles were examined using a 2.0 Malvern Zetasizer.

Cell culture

B16-F10 mouse melanoma cells (CRL-6457; American Type Culture Collection), RAW 264.7 mouse macrophage cells (TIB-71l; American Type Culture Collection), HepG2 human liver cancer cells (HB-8065; American Type Culture Collection), Caco-2 human epithelial colorectal cancer cells (HTB-37; American Type Culture Collection), HCT-116 human colon cancer cells (CCL-247; American Type Culture Collection), and HEK 293 human embryonic kidney cells (CRL-1573) were cultured for cell membrane derivation. Cells were cultured in DMEM media with 10% FBS (Gibco) and 100 U penicillin-streptomycin. The generation of bone marrow-derived dendritic cells (BMDCs) followed a previously published protocol[117]. Healthy mice were euthanized using carbon dioxide asphyxiation followed by cervical dislocation. Both femurs were dissected, cleaned in 75% ethanol, and cut on both ends. Bone marrow was then flushed out of the bone with a 1 mL sterile syringe using warm DMEM media containing 10% FBS (Gibco) and 100 U penicillin-streptomycin. Cells were then pelleted at 700 g for 5 minutes, resuspended in BMDC growth media consisting of the basal media further supplemented with 20 ng/mL granulocyte/macrophage-colony stimulating factor (GM-CSF; Protech) to a concentration of 1×10^6 cells/mL, and plated into petri plates at 2×10^6 cells per plate. Media was half-changed every two days.

Cytotoxicity Assay

The cytotoxicity of MSN, MSN-CpG and MSN-CpG@CMs in the RAW 264.7 or BMDC were assessed using an MTT assay. The assay was performed in a 96-well plate containing 5×10^3 cells per well. The cells were cultured in complete medium containing different concentrations (0, 12.5, 25, 50, 100, 200 μg/mL) of substances for 24 h, and an MTT assay was performed. The optical density of each well was measured by a multifunctional microplate reader at a wavelength of 490 nm. The relative survival rate (mean (%) ± SD, n=6) of the cells was calculated using the following equation: survival rate (%) = ($A490_{\text{treated sample}}$ / $A490_{\text{untreated sample}}$) × 100%.

In vitro uptake and activity

For the cellular uptake study, BMDCs were collected on day 5 and plated into 24-well suspension plates. FAM-labeled CpG, MSN-CpG and MSN-CpG@CMs were added at an equivalent CpG concentration of 5 μg/mL. After 3 h incubation, the cells were washed and stained with DAPI and LysoTracker Red. 15 minutes later, cells were imaged by confocal laser scanning microscopy (CLSM). For flow cytometry, cells were collected, washed twice in PBS, and resuspended in 200 μL of 10% PBS. The cell suspension was analyzed using BD Accuri C6 Plus flow cytometer. Collected data were analyzed by FlowJo software. The activity of the delivered CpG was examined using a BMDC maturation assay and cytokine release assay. BMDCs were collected on day 5, and 3×10^6 BMDCs were plated into 6-well suspension plates in BMDC growth media. Cells were pulsed with materials for 12 h at 5 μg/mL CpG, then washed twice with fresh media. After an additional 48 h of culture, cell supernatants were collected, and cytokine content was analyzed using IL-6 and IL-12 ELISA kits. The cells were then collected, washed twice, and stained with fluorescence isothiocyanate (FITC)-conjugated

anti-mouse CD11c and APC-conjugated anti-mouse CD40, CD80, or CD86. Appropriate dye-labeled antibody isotypes (BioLegend) were used for gating purposes with cells from an untreated lymph node. Data were collected using a BD FACSCelesta flow cytometer and analyzed using FlowJo software. RAW 264.7 cells were plated into 6-well suspension plates at 5×10^5 cells/well and pulsed with materials for 24 hours at 5 μg/mL CpG, then cell supernatants were collected, and cytokine content was analyzed using TNF-α ELISA kits.

In vivo lymph node distribution and DC activation

All animals received care in compliance with the guidelines outlined in the Guide for the Care and Use of Laboratory Animals, and the procedures were approved by the South China University of Technology Animal Care and Use Committee. Female C57BL/6J mice were obtained at 6–10 weeks old from Hunan SJA Laboratory Animal Co., LTD. Materials containing Cy5.5-labeled CpG or DiD-labeled membrane fragments were used to trace the distribution of nanovaccines in lymph nodes. Different materials were injected at foot pad and after 1, 3, 6, 12, 24, and 48 h, the mice were euthanized, and their popliteal lymph nodes were collected. Dye-labeled nanovaccines, 20 μL at 1 mg/mL, were injected into both hocks of mice. At time points of 6, 12, 24, and 48 h, the popliteal lymph nodes were collected. All the lymph nodes were analyzed and quantified by *In-Vivo* Xtreme Imaging System (Bruker).

To further assess the cellular uptake in the lymph nodes, dye-labeled nanovaccines were injected subcutaneously into each hock of mice. After 24 h, the popliteal lymph nodes were collected, dissociated manually by pipetting, then stained for 30 minutes with antibodies for dendritic cells (CD11c monoclonal antibody, 12-0114-82; eBioscience) and macrophages (F4/80 monoclonal antibody, 11-4801-82; eBioscience). Data were collected using BD FACSCelesta

flow cytometer and analyzed using FlowJo software. DC activation following immunization with CpG, MSN-CpG, and MSN-CpG@CMs was determined by testing DC maturation and lymph node cytokine secretion. To examine DC maturation *in vivo*, 20 μL of each material was injected into the hock. After 24 h, the popliteal lymph nodes of all treated mice were collected into 500 μL dissociation buffer and manually dissociated. Cells were stained using PE anti-mouse CD11c with either APC-conjugated anti-mouse CD40 (124611; BioLegend), CD80 (104713; BioLegend), or CD86 (105011; BioLegend). Data were collected using a Becton Dickinson FACSCanto-II FLow cytometer and analyzed using FlowJo software. To analyze cytokine production, lymph node-derived single-cell suspensions were plated with 500 μL of BMDC growth media in 24-well tissue culture plates. After 48 h, supernatant was collected and analyzed for cytokine content using IL-6 and IL-12 ELISA kits. To assess the generation of antigen-specific T cells, mice were vaccinated subcutaneously with 20 μL of the different materials on days 0, 2, and 4. On day 10, spleens were collected and processed into single cell suspensions. After lysis of red blood cells (RBCs), 5×10^6 splenocytes were plated onto 6-well suspension plates and pulsed with 1 μg/mL of mouse gp100 peptide with sequence EGSRNQDWL in BMDC growth media. After 7 days, cells were collected, washed in PBS solution, and stained with APC-conjugated anti-mouse CD8a and phycoerythrin (PE)-labeled H-2Db gp100 tetramer. Data were collected using a BD FACSCelesta flow cytometer and analyzed using FlowJo software. To evaluate the immunological effects of the combined treatment, B16-F10 tumor-bearing mice were randomly divided into six groups (n=3 mice per group). When the tumor volume reached approximately ~100 mm^3, the mice were treated with the different materials on days 1 and 4. After 7 days of treatment, the mice were sacrificed, and the tumors were collected for immunological evaluations. To evaluate the immune cells in tumors, tumors collected from

different groups of mice were cut into small pieces and homogenized in PBS (pH 7.4) containing 0.5% FBS to obtain suspensions of single cells, which were then stained with corresponding antibodies after the removal of RBCs using RBC lysis buffer (Solarbio). To identify CD4+cells (CD3+CD4+CD8-), CD8+cells (CD3+CD4-CD8+) and regulatory T cells (Treg cells) (CD3+CD4+Foxp3+), the following antibodies (from eBioscience, BioLegend) were used, respectively: CD4 monoclonal antibody (GK1.5, Alexa Fluor 488), CD8a monoclonal antibody (53-6.7, PE), CD3e monoclonal antibody (145-2C11, APC), True-Nuclear™ Mouse Treg Flow™ Kit (FOXP3 Alexa Fluor® 488/CD4 APC/CD25 PE), and TruStain FcX™ (anti-mouse CD16/32).

In vivo anticancer immunity and immunotherapeutic effects

To study the tumor prevention effect conferred by vaccination, mice were vaccinated with 100 μL of the different materials at 0.1 mg/mL of CpG or equivalent, on days -21, -14, and -7. On day -1, the right flank of each mouse was shaved and on day 0, mice (n=6) were challenged with 2×10^4 B16-F10 cells subcutaneously on the right flank. The tumor size was measured every other day and the experimental endpoint was defined as either death or a tumor size greater than 2000 mm^2. To study the therapeutic effect, mice were first challenged on the right flank with 1×10^5 B16-F10 cells on day 0. On days 2, 4, and 7, mice (n=6) were vaccinated subcutaneously in the same flank with 100 μL of the different materials. The checkpoint blockade cocktail, consisting of 100 μg anti-CTLA4 (BP0164; BioXCell), was administered intraperitoneally on the same days. Tumors were measured every other day and the experimental endpoint was defined as either death or a tumor size greater than 2000 mm^2.

3.3 Results

S*A2.1 Characterize flash-based cell membrane-coated nanoformulations*

It is often challenging to coat negatively charged cell membranes onto a positively charged nanoparticle, despite the concept of cell membrane coating majorly relying on electrostatic interaction[99]. Coating cell membranes onto a cationic NP is difficult partly due to the large difference in charge between the cell membrane and the NP surface, which leads to a heterogenous collapse of the cell membrane onto the NP and nanoparticle aggregation[27]. So, coating the cell membrane uniformly onto a nanoparticle surface is crucial for the nanoparticle colloidal stability and hence, the completeness of the coating affects the therapeutic outcome. Before performing cell-membrane coating experiments using the FNC, it is important to understand the mechanism of how the negatively charged cell membranes associate onto the positively charged NPs using computational simulation. Molecular dynamics (MD) is a convenient tool to study the interactions between atoms, molecules, and larger biological substances with distinctive force fields. We utilized the MARTINI force field, which is a coarse-grain model that is often applied for studying molecular interactions. We constructed a silica-based particle and created lipid molecules made of different charges and moieties to mimic the cell membranes. The collective surface charge of the constructed lipid molecules is anionic, and the constructed silica-based particles is cationic. The simulation process is constructed using LAMMPS, a classical MD code based on C++. By simulating many cycles over time, we were able to examine how the anionic lipids molecules associate onto the surface of the cationic silica-based particles in a uniform coating manner (**Figure 14**). Coating lipid molecules on polymeric NPs in a microfluidic-based flow system have been performed in similar simulation

studies[2,68,111]. A similar situation is also found in the highly dynamic FNC chamber as diffusion between different biomaterials happens faster than the coating process.

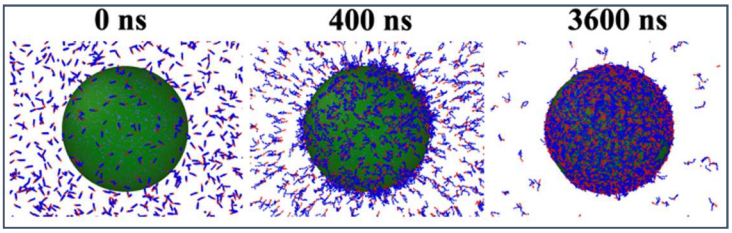

Figure 14: MD simulation of homogeneously distributed anionic lipids interact with the cationic silica NP.

Next, we selected several distinctive core materials with different compositions, surface morphologies and surface charges. We also derived various types of cell membranes to evaluate the cell membrane coating using FNC. Importantly, we compared the coating outcome of the conventional bulk mixing through basic pipetting/sonication to the FNC-based technique. Colloidal stability of a nanoparticulate system is crucial to its blood circulation and retention in tissues, thus greatly affecting delivery and therapeutic outcome. We observed that the majority of FNC-based cell membrane-coated nanoformulations are more stable on day 0 (immediately after coating) and on day 14 in 1X PBS solution (**Figure 15a**). These results suggest that the stabilizing effect of the FNC-based membrane coating is more prominent for the positively charged core (MSN big pore +) compared to its bulk method counterpart. Based on the TEM images, a darker 8-10 nm layer of cell membrane coating can be seen on the core material surface due to the difference in electron conductivity between the bare core and the cell membrane fragments (**Figure 16**). In SA2.2, we will discuss the *in vitro* and *ex vivo* results of the FNC-based cell membrane-coated nanoformulations.

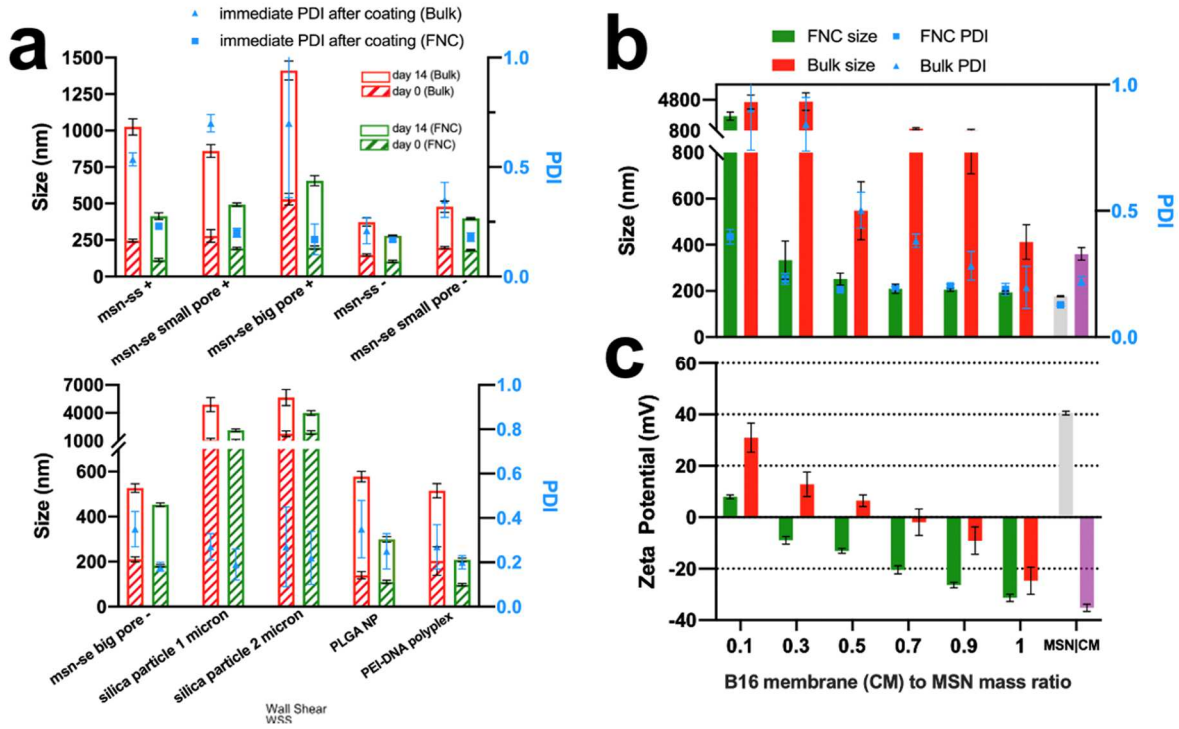

Figure 15: Fabrication of cell membrane-coated NPs using FNC. (a) Comparison of FNC and bulk sonication methods on PDI and stability of membrane-coated NPs. Characterization of membrane-coated MSNs using different membrane-to-MSN ratios in terms of (b) size and PDI, and (c) zeta potential.

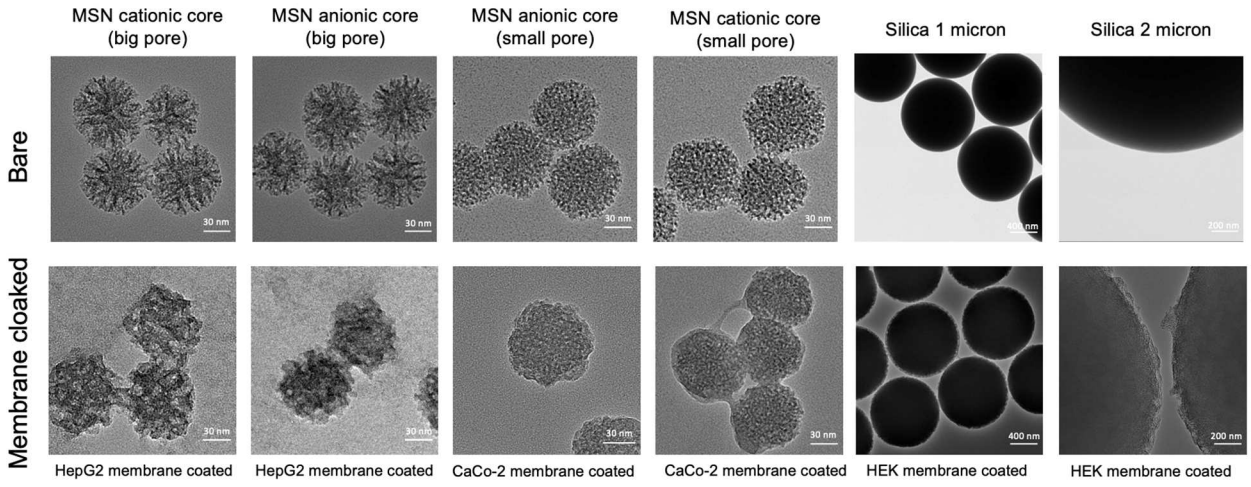

Figure 16: TEM images of different cores and cell membrane-coated particles prepared using FNC.

SA2.2 In vitro and ex vivo evaluation of membrane-coated formulations on APC uptake and lymph node targeting

FNC system can be harnessed to uniformly coat cell membranes onto NPs in a scalable manner. The potential of the uniform coating and massive production of the FNC system make it particularly ideal for vaccine development. To demonstrate the capability of the FNC-based coating technology in a biological application, we chose to validate the cell membrane-based nanoformulation in immunomodulation since the majority of the transmembrane proteins could be well preserved. First, we derived the cell membrane fragments from melanoma cells (B16-F10), largely owing to the presence of gp100 and TRP2, two cancer antigens commonly to be used for melanoma cancer immunotherapy[118,119]. In addition, CpG, a common bacteria-based nucleotide, was used to serve as the immune-adjuvant for loading onto the porous MSNs (**Figure 17**). To confirm that the antigens were well preserved after coating, we compared the protein bands among the cell membrane fragments, membrane-coated MSNs through bulk sonication, and the FNC-based approach by gel electrophoresis (**Figure 19, left**). The gel electrophoresis results suggest that the majority of the cell membrane-bounded proteins have been preserved after membrane coating of the CpG-loaded MSNs. Importantly, two important antigens, gp100 and TRP2, were preserved after coating, which was validated by Western blotting (**Figure 19, right**). To test our hypothesis that FNC is able to coat membrane onto a nanoparticle in a homogeneous manner, it is also important to confirm the gp100 proteins are uniformly presented on the outer surface of the MSN after coating, I therefore performed the negative staining as well as the gold-immunostaining of the gp100 to observe the coating under the TEM (**Figure 18**). Although it is difficult to distinguish the difference between the two coating methods in term of the gold nanoparticle distribution, it is reasonable to postulate the random distribution of the gold

NPs after immunostaining may be caused by the uneven distribution or non-uniform quantity of the anti-gp100 antibody of the gold immune-conjugation or due to the difference in strength of the antibody recognition during preparation.

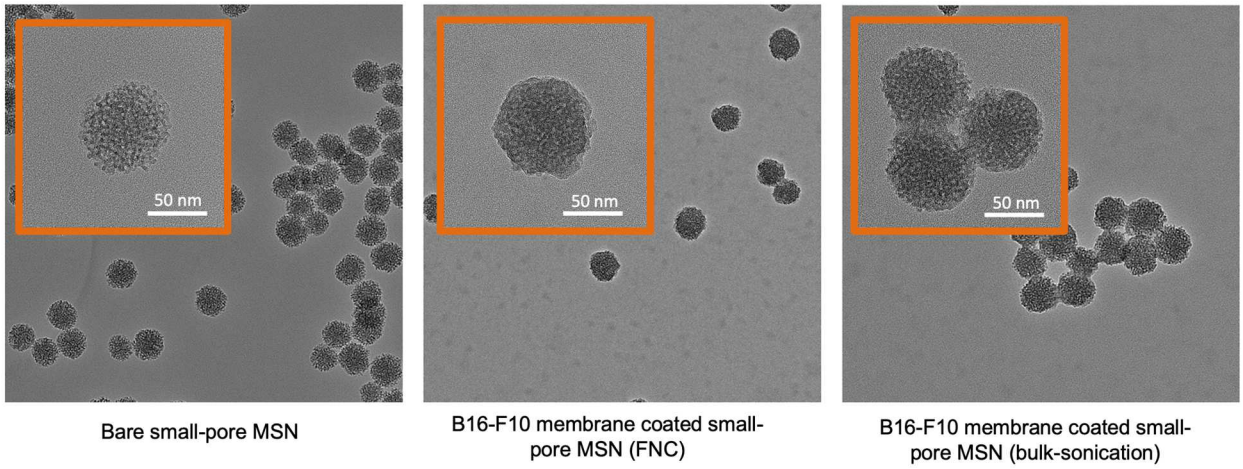

Figure 17: TEM images of uncoated MSN small pore, B16-F10 melanoma cell-membrane-coated small-pore MSN by FNC method, and by the bulk-sonication method, respectively.

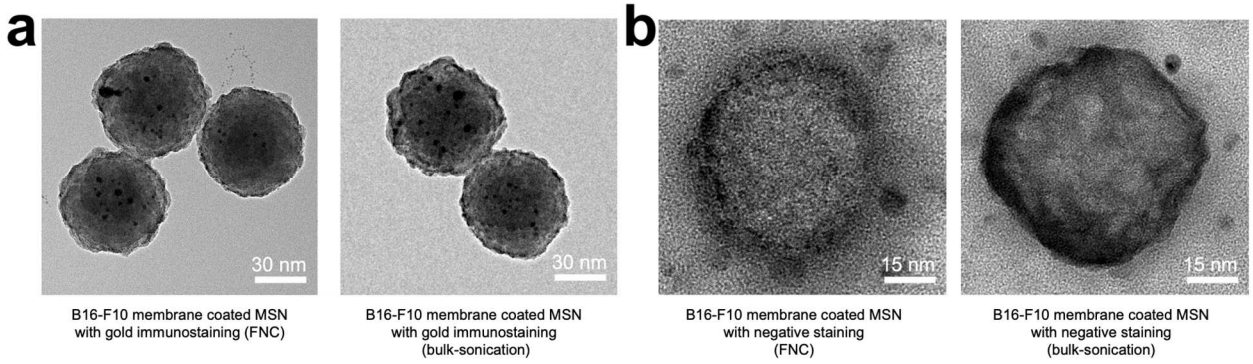

Figure 18: TEM images of (a) B16-F10 melanoma cell-membrane-coated MSN by FNC method and bulk sonication method with anti-gp100 gold immunostaining, respectively, and (b) B16 melanoma cell-membrane-coated MSN by FNC method and bulk sonication method with negative staining, respectively. (*Data on figure 18 were collected by Dr. Dan Shao)

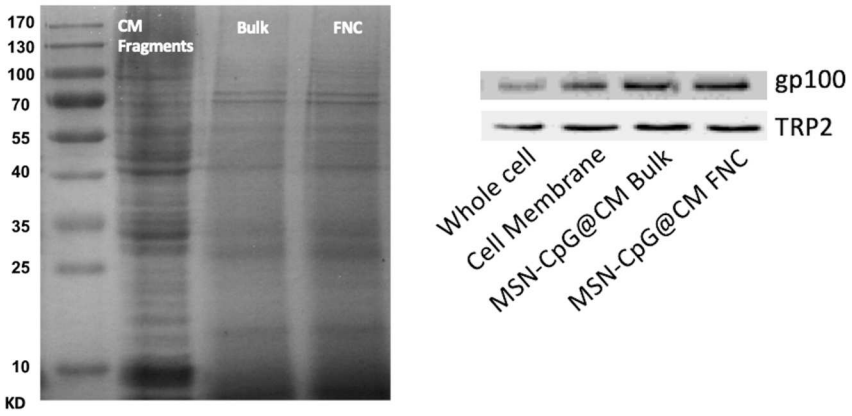

Figure 19: Confirmation of the presence of the protein after cell membrane coating *via* gel SDS-PAGE electrophoresis (left) and Western blotting (right).

In terms of successful immune-activation, a high spatial and temporal correlation between the antigen and the adjuvant of a nanoparticulate system is crucial[120]. From the cellular perspective, a cell membrane-coated nanoparticle needs to be endocytosed by the antigen presenting cell in order to activate the subsequent innate or adaptive response for serving its purpose as a competent vaccine. To demonstrate the potency of a nanovaccine after it has been endocytosed, it is important to evaluate the membrane integrity during the nanoparticle uptake in the murine macrophages[121,122]. Again, membrane integrity is essential for immune-activation since the spatial-temporal presence of both antigen and adjuvant affects the magnitude and duration of APC maturation. To evaluate the integrity of our manufactured nanovaccine, we loaded the FITC-labeled CpG onto the large pore MSNs and coated the MSNs with Cy5-labeled B16-F10 cell fragments. We then cultured the fluorescently labeled membrane-coated MSNs in RAW 264.7 cells (murine macrophage cell line) for 3 h. By confocal microscopy, we observed the co-localization of FITC, and DiD emission within the macrophage, suggesting that with the Cy5-labeled cell membrane as the antigen and FITC-labeled CpG as the adjuvant, there is strong

membrane integrity and spatial coordination (**Figure 20a**). The confocal microscopy images suggest the good integrity of the cell membrane-based nanovaccine at *in vitro* level.

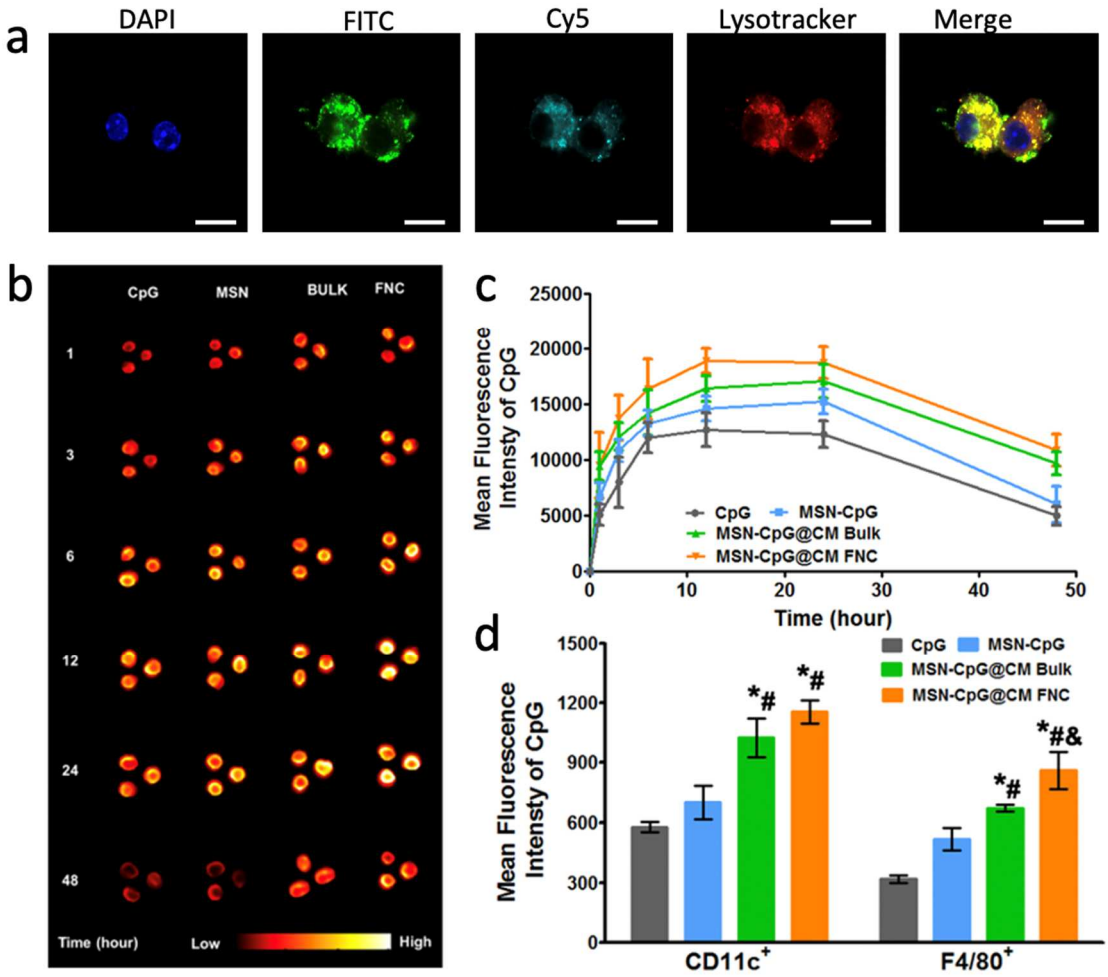

Figure 20: *In vitro* and *ex vivo* evaluation of B16-F10 membrane-coated MSNs. (a) Membrane-coated MSNs uptake in bone marrow-derived macrophages at 3 h for CpG (FITC) and membrane (Cy5), (b) fluorescence imaging of popliteal lymph node at indicated time points after footpad injection of free CpG, naked MSN-CpG, or membrane-coated CpG-MSNs produced using bulk sonication or FNC methods, (c) quantification of fluorescence intensity from Cy5.5-labeled CpG in the popliteal lymph node, (d) uptake of Cy5.5-labeled membrane-coated CpG-MSN by DCs and macrophages in the lymph node at 24-hours after injection. Data represents mean ± SD (n=3, $^{*}p<0.05$ vs. CpG group, $^{\#}p<0.05$ vs. MSN-CpG group, $^{\&}p<0.05$ vs. bulk MSN-CpG@CM group).

To further evaluate the immune-activation profile of our cell membrane-based nanovaccine, we then compared the uptake of MSN-CpG@CM by BMDCs (**Figure 20b**). Of

note, DCs are prominent in boosting the immune response by bringing processed antigens to their cellular surface for other immune cells, like T cells, to recognize[123–125]. MSN-CpG@CM were injected into mice via the foot pad and nanovaccines were observed in the popliteal lymph node 1 h after administration. The fluorescence signal from dye-labelled CpG peaked at 12 h post-injection and began to decrease at 24 h post-injection. Both MSN-CpG@CM groups (prepared using either FNC or bulk sonication) showed improved CpG uptake by DC cells versus naked MSN-CpG, demonstrating the APC-targeting effect *in vitro*. Quantification of mean fluorescence intensity of free CpG, naked MSN-CpG, and MSN-CpG@CM in the lymph node confirmed this observation (**Figure 20c**). These data again suggest that the greater lymph node accumulation of MSN-CpG@CM was achieved by using the nanovaccine prepared through the FNC method than the ones prepared through the bulk sonication method. Both DCs and macrophages preferred endocytosing MSN-CpG@CM to MSN-CpG, indicating specific recognition of tumor antigens by the APCs. Greater CpG accumulation of DCs and macrophages in the popliteal lymph node indicates that FNC produced a cell membrane-coated cancer vaccine with improved lymph node targeting and APC accumulation.

Importantly, the membrane-coated MSNs also need to escape the endosome and release their cargo CpG in the cell cytoplasm to activate the immune response. BMDCs play an indispensable role in priming and immune activation. Matured BMDCs can further activate T cells for antibody generation and tumor suppression[120,126–128]. To further validate the DC maturation, we injected four formulations and a negative control into the mice subcutaneously and quantified the maturation markers (CD40, CD80, and CD86) of the DCs harvested from the popliteal lymph nodes (**Figure 20d**). All four formulations (CpG, MSN-CpG, MSN-CpG@B16 membrane by bulk/sonication, and MSN-CpG@B16 membrane by FNC) show increasing

numbers of mature DC population compared to the untreated group. Overall, cell membrane-coated nanoformulations show an enhanced APC uptake and lymph node targeting effect, which is crucial for successful immune activation and modulation. The FNC-based membrane-coated nanoformulation shows even better APC targeting efficacy, possibly due to a more complete coating and improved colloidal stability, making FNC-based membrane-coated MSNs ideal candidates for cancer immunotherapy. Next, we will perform animal studies to further evaluate the potency of the flash-based nanovaccine.

SA2.3 In vivo validation of membrane-coated nanoformulations for cancer immunotherapy

In vivo validation is the key to evaluate the efficacy of membrane-coated MSN nanoformulation on immune-activation. First, we selected the melanoma model and inoculated the mice with B16-F10 tumor cells for tumor development. We administered the cell membrane-based nanovaccine prepared by the FNC system to the tumor inoculated mice for immune-activation of T killer cells to treat melanoma (**Figure 21**). In terms of efficacy and potency of the nanovaccine *in vivo*, strong prophylactic and therapeutic effects are important indicators when applied to the tumor treatment model. In the prophylactic model, the mice are dosed with the nanovaccine before tumor inoculation and then tumor growth is monitored. On the contrary, the therapeutic model is to inoculate the mice with the tumor and then administer the nanoformulations to see how effective these nanoformulations are in preventing tumor growth. The timeline for both models is depicted in **Figure 21**.

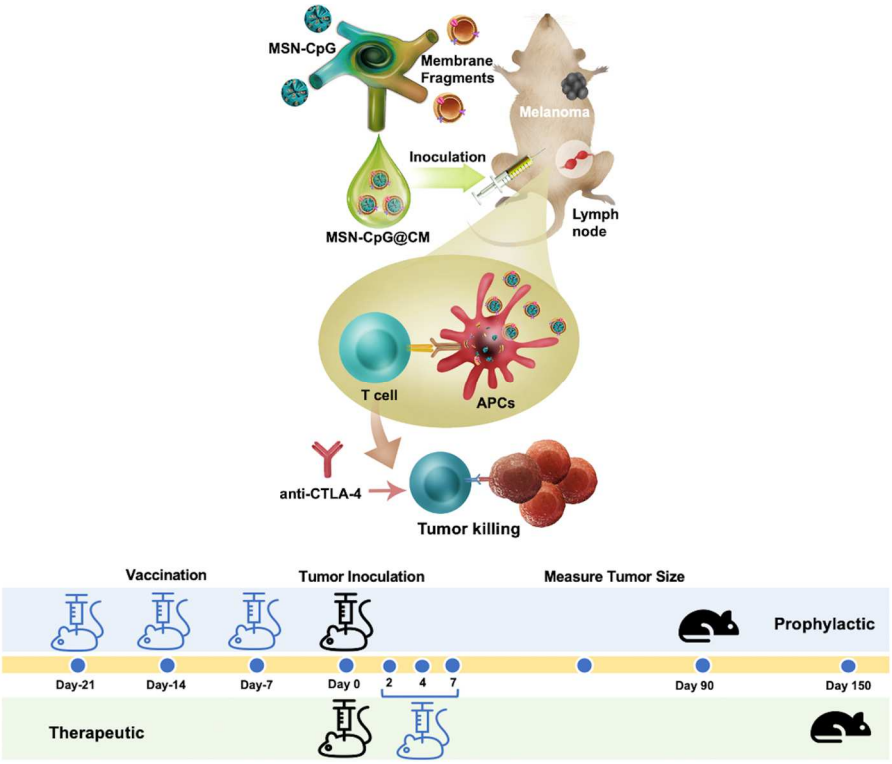

Figure 21: Schematic illustration of B16-F10 cell membrane-based MSNs for melanoma cancer immunotherapy (top) and the illustration of the *in vivo* prophylactic and the therapeutic experiment design using the mouse model (bottom).

Specifically, we evaluated the APC response, specific immune activation, and prophylactic tumor growth inhibition *in vivo* using a wild-type B16-F10 murine model. Mice were vaccinated using different nanoformulations and tumor growth was monitored for up to 40 days. In term of the results, MSN-CpG and free CpG had no significant protective benefit, consistent with previous studies; both treatments showed a median survival time of 29 d, similar to the median 26.5 d survival time for the negative control. Both FNC- and sonication-produced MSN-CpG@CM groups showed tumor growth inhibition, but the FNC-produced vaccine had a greater tumor growth inhibitory effect, and a more prolonged survival time was observed (**Figure 22a**). The improved anti-tumor response of our FNC-based nanovaccines can be explained as a result of better lymph node targeting, due to the enhanced colloidal stability of the

NPs. Next, we compared the therapeutic performance of the MSN-CpG@CM with and without the immune checkpoint-blocking antibody anti-CTLA-4. Without anti-CTLA-4, the median survival time was extended from 18 d for the blank control group, to 34 d for the bulk/sonication MSN-CpG@CM group, and to 38 d for the FNC MSN-CpG@CM group (**Figure 22b**). With anti-CTLA-4, the median survival time was over 150 days for both FNC and sonication MSN-CpG@CM groups, indicating that the combined immunotherapy produced synergistic antitumor effects.

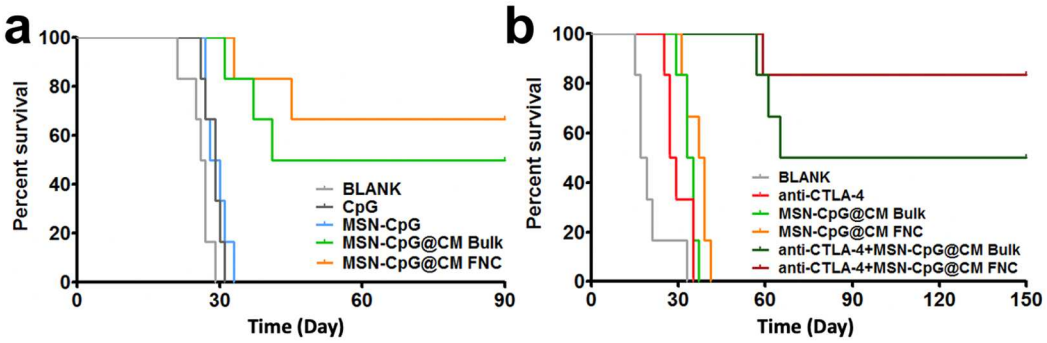

Figure 22: Anticancer immune response in melanoma mouse model. (a) Prophylactic effect of nanovaccines on survival time (n=6). (b) Therapeutic effect of nanovaccines with or without the checkpoint blockade inhibitor anti-CTLA-4 on survival time (n=6).

Importantly, we evaluated the CD8+/CD4+ ratio, the percentage of cytotoxic T lymphocytes, and the percentage of regulatory T cells within the tumors using different nanoformulations. A normal CD8+/CD4+ ratio is close to 1 in healthy mice. We could see the combined therapy using FNC-produced nanovaccines with anti-CTLA-4 led to the most potent antitumor effect among the groups, correlating with an increased CD8+/CD4+ ratio, a higher cytotoxic T lymphocyte number, and a reduced regulatory T cell number within the tumors (**Figure 23a-c**). These results demonstrate that the FNC-based nanovaccine is potent for killer T cell activation, which is essential for a strong immune response to combat tumor growth.

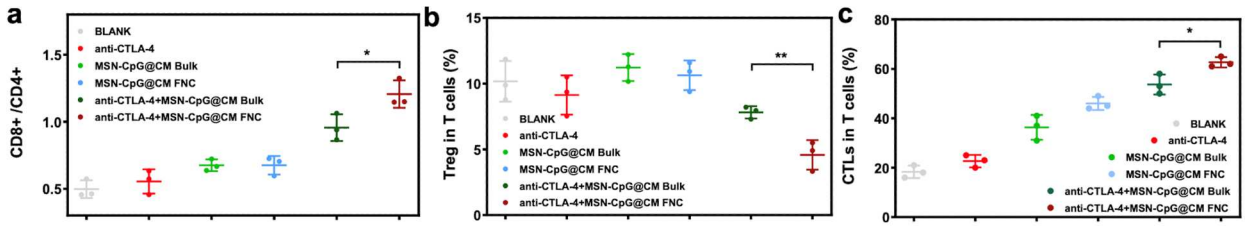

Figure 23: Relative composition of T cells within the tumor in the melanoma model after administration of nanoformulations with or without the checkpoint blockade inhibitor anti-CTLA-4 (n=3). (a) Ratio of CD8+ to CD4+ T cells, (b) percentage of regulatory T cells, and (c) percentage of cytotoxic T lymphocytes. (*Data were collected with help from Dr. Dan Shao)

3.4 Discussion

In summary, we have demonstrated a nanoformulation platform for fabricating diverse cell membrane-based NPs in a facile, reproducible, and scalable manner. The FNC platform leverages dynamic, turbulent mixing to homogeneously blend and uniformly distribute cell membrane fragments around NP surfaces. We also performed MD simulations to understand how negatively charged lipid molecules land uniformly onto positively charged NPs. For future studies, this computational tool is extremely helpful to understand the mechanistic interaction between biological substances and NP formation. Utilizing computational power, screening, optimization, and much more can be achieved with lower costs and in reduced time. We establish that FNC can be used to coat both negatively and positively charged particles with cell membranes, and it reduces batch-to-batch variation and production time, compared to the conventional sonication-coating process. This largely automated process should facilitate standardization. In addition to achieving higher throughput, the FNC process may also improve the potency of nanotherapeutics. FNC-produced MSNs loaded with CpG adjuvant and coated with a cancer cell membrane exhibited enhanced accumulation in lymph nodes, immune activation, and more significant tumor growth inhibition, with and without the immune checkpoint-blocking antibody anti-CTLA-4 in a melanoma model. This study addresses the challenge of manufacturing cell membrane-coated nanotherapeutics. For future studies, the infiltration of other immune cell types and the recruitment and repolarization of tumor-associated macrophages (TAMs) in the tumor microenvironment (TME) would be worth investigating. Furthermore, an in-depth mechanistic investigation of the cell membrane-coated NPs in generating an immune response, tissue biodistribution, and intracellular trafficking would be worth exploring. Importantly, deriving cell membranes directly from the tumors harvested from

patients with preserved neo-antigen diversity depends on the stage of malignancy. Exploring how cell membrane-coated nanotherapeutics play a role in immunomodulation to affect surrounding tissues, as well as in adaptative immune systems in penetrating, accumulating, or interacting with healthy or cancerous cells through bulk RNA sequencing or DNA sequencing could provide great insight and flexibility for future cancer precision therapy. Importantly, establishing a feedback-responsive computer-based flash system that can manufacture cell membrane-coated nanotherapeutics would be ideal for this technology to be translated into clinics with mass production potential, minimum operational variation, and fast on-demand preparation.

Chapter 4: Development of Microbiome-based Formulations for Oral Drug and Gene Delivery

* Data in SA3.2 were collected with the help of Dr. Dan Shao, Dr. Chao Yang, and Dr. Mingqiang Li

4.1 Introduction

Oral delivery is recognized as one of the most desirable routes of administration to treat a wide range of chronic diseases[82]. Convenience, high safety, treatment adherence, ease of modulation, and a longer therapeutic window have popularized oral drug delivery strategies and make them readily accepted by patients[4,129]. However, low mucosa retention and penetration of drug molecules, host immune responses, and variability of the individuals gut flora hinder the clinical translation of many promising oral delivery candidates[130,131]. Currently, microorganism-based strategies such as bacteria- and yeast-derived microformulation, are providing researchers new insights into improving the bioavailability of nanotherapeutics[132–134]. Baker's yeast (Saccharomyces cerevisiae) is the unicellular and saprotrophic fungus that has been widely used in fermentation and for human health[62,135,136]. Of particular interest in drug delivery, the cell wall of this oval-shaped yeast is mainly composed of β-glucan-rich polysaccharides (roughly 80%) with the remaining 20% being proteins and lipids[16,84,137,138]. Since many forms of the β-glucans are water-insoluble and can be regarded as a pathogen-associated molecular pattern (PAMP), the Saccharomyces can be easily recognized and endocytosed by specialized gut epithelial cells like M cells and APCs[84,139,140]. Very recently, researchers in nanomedicine have been taking advantage of this uptake specificity as well as the spacious internal cavity of the yeast capsule via removing its intracellular contents in which cargoes (imaging agents like

Quantum dots, proteins like OVA, insulin, antigens, and NPs) were entrapped within the micron-sized yeast ghost (YG) (4-6 μm)[141,142]. Notably, the consummate drug delivery efficiency and the therapeutic outcome are indispensably hinged upon the loading level of the cargo into the yeast ghost. However, the loading mechanism of compounds and NPs into the yeast ghost remains elusive. Studies have reported NP loading by exploiting the electrostatic interaction between positively charged NPs and negatively charged yeast ghosts. Nonetheless, instead of simply displacing the NPs inside the yeast ghost cavity for maximum protection and loading, a large amount of the positively charged NPs can attach to the outer surface of the YG, which may compromise the specific cellular recognition and particle uptake efficiency. Despite these literature reports24, studies have not justified nor quantified to what extent these positively charged NPs were loaded inside the yeast ghosts, rather than the NPs lingering on the outer surface. In addition, anionic NPs are more challenging to be loaded into the yeast ghost based on the electrostatic mechanism[58]. Thus, a novel strategy to efficiently load drug-loaded NPs to the yeast ghost is essential to popularize the yeast-implemented therapeutic solutions via the oral route.

Moreover, the PAMP receptor-targeting polysaccharides made of the yeast cell walls can be further processed into nanosized fragments, and they can be coated onto NP surfaces. Due to the advantages of the NP size, the mucus retention profile, and the penetration of gut epithelium of the NPs are worth exploring because the polysaccharides are also forms of immune adjuvants that can be co-delivered for immunomodulation. Together with the function of NPs and nanoparticle-loaded antigens and adjuvants, the yeast-based formulation can be engineered as a promising oral vaccine.

The work covered in this chapter, taken as a whole, makes a case for the importance of exploiting biomimetic strategies in developing a robust oral delivery formulation that aims to

reduce the cost, improve the therapeutic bioavailability, and partially fulfill the translational need of an effective oral delivery platform.

4.2 Materials and Methods

Prepare and characterize microbiome-based formulations

Preparation of the yeast ghost

40 g of Baker's yeast (Sigma) was suspended in 600 ml of 1 M sodium hydroxide. The suspension was heated at 80°C for 1 h and centrifuged at 3,000 rpm for 10 minutes. The collected pellet was washed twice with Milli-Q water and then dispersed in an aqueous solution at pH 4 and incubated at 60°C for 1 h. The sample was collected by centrifugation and thoroughly washed with DI water. Subsequently, the obtained sample was rinsed with 100 ml of isopropyl alcohol four times. After another rinse with acetone, the resulting YGs were collected by centrifugation and dried under vacuum at room temperature. To label the yeast ghost with FITC, 1 mg/mL of FITC was dissolved in DMSO and was added to 100 mg/mL yeast ghost (dispersed in Milli-Q water). The mixture was allowed to incubate with shaking overnight. The labeled yeast ghost was then collected through centrifugation and washed with PBS solution.

Yeast ghost drug loading

PLGA NPs loaded with 5-ASA were prepared by the nanoprecipitation method. 5-ASA-to-polymer ratios (1%, 3%, 5%, 10% and 50% w/w) were prepared. The weighted 5-ASA and PLGA were dissolved in 10 mL DCM, and the mixed solution was vortexed and sonicated. The drug/PLGA solution was dropwise added to water with stirring at 1,000 rpm to form drug-loaded PLGA NPs. The nanoparticle solution was then put under a vacuum to remove the organic

solvent with continuous stirring overnight. To load PLGA NPs into yeast ghost, we dispersed PLGA NPs in water and mixed it with dry yeast ghost by vortex and sonication. The obtained PLGA loaded yeast formulations were centrifuged at 4,000 rpm for 10 minutes to remove any unbounded NPs. The obtained yeast formulations were washed with Milli-Q water three times and then lyophilized and stored. For *in situ* 5-ASA loading onto the yeast ghost. We first dissolved 7 mg of PLGA polymer into 1 mL DCM then added 3.5 mg 5-ASA. The combined solution was vortexed until fully dissolved and then was combined with 10.5 mg yeast ghost. The yeast ghost-drug suspension was then vortexed and stirred for 30 minutes and added dropwise to 3 mL Milli-Q water with continuous stirring. The resulting solution was centrifuged at 4,000 rpm for 10 minutes to discard the unbounded drug and polymer. The obtained yeast formulation was washed with Milli-Q water three times. Then, 5 mL of water was used to resuspend the pellet. The resulted solution was vacuum-dried to obtain the drug-loaded yeast formulation in powder form.

Drug loading and encapsulation efficiency of the ICG or 5-ASA-loaded yeast formulations were analyzed with an ultraviolet-visible (UV-vis) spectrophotometer at 775 nm (ICG) and 350 nm (5-ASA). The drug loadings of the ICG or 5-ASA in both *in situ* and conventionally prepared yeast formulations were calculated according to Beer's law and to the following formulas based on a calibration curve obtained with known drug concentrations.

Drug Loading (%) = (weight of loaded drug/total weight of YGs with drug) × 100%

Encapsulation Efficiency (%) = (weight of loaded drug/weight of input drug) × 100%

For *in situ* CDDP loading onto the yeast ghost. We dissolved 14 mg of PLGA polymer into 1 mL DMF then added 10.5 mg CDDP. The combined solution was vortexed until fully

dissolved and then was poured into 10.5 mg yeast ghost. The yeast ghost-drug suspension was then vortexed and stirred for 30 minutes and added dropwise to 3 mL Milli-Q water with continuous stirring for 10 minutes. The resulted solution was centrifuged at 4,000 rpm for 10 minutes to discard DMF. 5 mL of water was used to resuspend the pellet. The resulted solution was vacuum dried to obtain drug-loaded yeast formulation in powder form. For preparing CDDP-loaded PLGA NPs, 14 mg PLGA was dissolved in 1 mL DMF. 10.5 mg of CDDP was then added to the DFM solution. Then, DMF solution was added dropwise to 3 mL water in a glass beaker with stirring. Next, the resulting solution was centrifuged at 10,000 rpm for 30 minutes. The pellet was resuspended in 5 mL water and dried under vacuum.

For loading CDDP into the yeast ghost conventionally. the prepared CDDP-PLGA NPs (in Milli-Q water) was combined with yeast ghost powder (10.5 mg) and stirred for 20 minutes. The combined solution was centrifuged at 4,000 rpm for 10 minutes and the pellet was resuspended in 5 mL water and dried under vacuum.

The preparation of DOX-loaded PLGA NPs was as previously described[143]. Briefly, DOX HCl was dissolved in the DCM and stirred for 24 h in the presence of triethylamine at room temperature (1:3 mole ratio). After dissolving in 20 mL DCM, PLGA solution was stirred in the demineralized-DOX solution. Then, 150 mg of dry YG was added into the organic solution and stirred moderately at 500 rpm for 30 minutes. The NPs formed immediately when the organic solution was added dropwise to the distilled water the solution was stirred overnight to eliminate the remaining solvent. Finally, DOX/PLGA@YG (*in situ*) was harvested after lyophilization. Similarly, Dox-loaded PLGA NPs were prepared without the YGs. DOX-loaded PLGA NPs were stirred with YGs in the DCM solution overnight. Following drying under vacuum, DOX/PLGA@YG(c) could be obtained.

Derivation of yeast fragments

First, 100 mg lyophilized yeast ghosts were disrupted with a mortar and pestle into the fine powder, then 10 mL of Milli-Q water and protease inhibitor cocktail were added. Next, the processed yeast ghosts in Milli-Q water were dropwise added to a cryo-preserved jar filled with liquid nitrogen to form uniform spherical precipitations (Ø 2-5 mm). Then, we collected the frozen yeast ghosts in spherical form and transferred them into a 50-mL tube surrounded by dry ice to avoid melting. Next, we loaded the frozen yeast ghosts into a SPEX freeze mill and milling for 6 hours under liquid nitrogen. The obtained yeast fragments are fine powder and appear a white color. The obtained yeast fragments were lyophilized, characterized, and stored.

IBD murine model

Male C57BL/6 mice with bodyweights of 21-23 g were used for *in vivo* studies. 3% DSS was given orally (*p.o*) to experimental group mice for 4 days (administered daily) to develop inflammatory bowel disease (IBD). For therapeutic groups, drug-loaded formulations were administered by oral gavage to mice for 11 days (administered 200 μL every other day). Colons were later harvested to be measured and processed for immunostaining and H&E staining. Specifically, all animals received care in compliance with the guidelines outlined in the Guide for the Care and Use of Laboratory Animals, and the procedures were approved by the South China University of Technology Animal Care and Use Committee, as well as by the Institute of Comparative Medicine at Columbia University. Male C57BL/6J mice and female BALB/c mice were obtained at 6–10 weeks old from Hunan SJA Laboratory Animal Co. LTD. Female BALB/c mice at ages of 10 weeks or older were purchased from Jackson Laboratory. Mice were

housed under a 12 h light/dark cycle and constant temperature (21 ± 1°C) with free access to autoclaved chow and water.

Acute ulcerative colitis was induced by addition of 3% (w/v) DSS (36–50 kDa; MP Biomedicals) to the mouse drinking water for 5 days. The male C57BL/6J mice treated with DSS were administered 5-ASA, 5-ASA/PLGA, 5-ASA/PLGA@YG(c) or 5-ASA/PLGA@YG(in) at 10 mg/kg of 5-ASA equivalent via oral gavage. For all diseased mice, daily administration was performed for 12 days, beginning on the third day of DSS treatment, while control mice were administered water. Body weight, fecal bleeding, and visible stool consistency changes in mice were observed and recorded daily. On day 14, the mice were sacrificed, and colon tissues were collected for determining colon length and histopathological examination. Remaining colon tissue was homogenized and prepared for analysis of TNF-α, IL-1β and IFN-γ levels.

Colonic disease activity index

The colonic disease activity index (DAI) was scored using the following criteria: stool consistency (hard: 0, soft: 2, and diarrhea: 4), fecal occult blood using Hemoccult Sensa (Beckman Coulter) (negative: 0, positive: 2, and macroscopic: 4), and weight loss (Less than 1%: 0, 1−5%: 1, 5−10%: 2, 10− 20%: 3, and more than 20%: 4). See **Table 1** for reference.

Ex vivo analysis of cytokines

The length of the colon was determined by measuring the distance between the most distal part of the cecum and the rectum. To determine the cytokine contents of the colon tissue, the colon segments were homogenized in 50 mM PBS solution (pH 6.0) in the ratio of 1:10

(w/v). The resulting samples were then subjected to centrifugation at 10,000 g for 10 minutes at 4°C. Colonic TNF-α, IL-1β and IFN-γ levels were determined by using ELISA assay kit.

In vivo anticancer therapeutic model

To study the melanoma tumor therapeutic effect conferred by CDDP/PLGA@YG, C57BL/6J mice were first challenged on the right flank with 1×10^5 B16-F10 cells. When tumor volume reached 100 mm^3, mice were randomized into 6 groups (n = 6) and treated with water, free CDDP, CDDP/PLGA, CDDP/PLGA@YG(c) or CDDP/PLGA@YG(in) at 2.5 mg/kg of CDDP equivalent via oral gavage. The other group of mice were orally administered with free YG the same amount as the CDDP/PLGA@YG(in) group. Mouse weight and tumors were measured every other day and the experimental endpoint was defined as either death or tumor size greater than 2000 mm^3. All tumors and major organs (heart, liver, spleen, lung, and kidney) were collected, and the tumors were weighted. Serum was collected after centrifuging whole blood at 3,000 rpm for 15 minutes. The biochemical parameters, including alanine aminotransferase (ALT), aspartate aminotransferase (AST), blood urea nitrogen (BUN) and creatinine (CRE), were assayed.

To investigate the therapeutic efficacy of DOX-loaded formulations in the liver tumor model, free DOX, DOX/PLGA, DOX/PLGA@YG(c) or DOX/PLGA@YG(in) at 5 mg/kg of DOX equivalent and YG (at same amounts of DOX/PLGA@YG(in)) were administered to the female BALB/c mice bearing 100 mm^3 4T1 liver tumors via oral gavage for 21 days. Tumors were measured every three days and the tumors were weighed at the experimental endpoint.

IVIS imaging

PLGA-loaded yeast ghost (Cy7-PLGA) was orally administered to mice (C57BL/6) at 12, 24, and 48 h. Mice were then euthanized, and the liver, lung, heart, colon, stomach, small intestine, pancreas, and kidney were harvested and imaged under an IVIS spectrum optical imaging system for fluorescing analysis. The fluorescence intensity was quantified using the IVIS analyzing system.

MSN@YF or MSN@Caco-2 (Cy7-MSN) was orally administrated to overnight-fasted mice (BALB/c, 10 weeks old) at 2, 4, 8, 12, and 24 h time points. Mice were then sacrificed, and the liver, lung, heart, entire GI tract, spleen, kidney, and mesenteric lymph nodes were harvested and imaged under an IVIS spectrum optical imaging system for fluorescence analysis. The fluorescence intensity was quantified using an IVIS analyzing system.

In vivo biodistribution analysis via ICP/MS

To investigate the biodistribution of YG delivery system *in vivo*, free CDDP, CDDP/PLGA, CDDP/PLGA@YG(c) or CDDP/PLGA@YG(in) were administered to C57BL/6J mice in the colitis or melanoma tumor model groups. In the colitis model, mice induced by 3% DSS were administered with different formulations of CDDP at 2.5 mg/kg of CDDP equivalent on day 3 and were sacrificed at 12, 24, 48 h post gavage. Parts of GI tissues (stomach, small intestine, and colon) were separated, and the platinum content was analyzed by ICP/MS. In the melanoma tumor model, when the tumor volume reached 500 mm^3, mice were administered with different formulations of CDDP at 2.5 mg/kg of CDDP equivalent and were sacrificed at 24 and 48 h post gavage. The main tissues including tumors, livers, kidneys, spleens, lungs, colon, and hearts were collected and the platinum content was analyzed by ICP/MS. To investigate the biodistribution of MSN@YF in vivo, MSN and MSN@YF were orally administered to BALB/c

(10 weeks old, female) mice. Mice were euthanized and sacrificed at 4-hour, 8-hour, and 24-hour post-oral gavage. Heart, lung, liver, spleen, kidney, and mesenteric lymph nodes were harvested and weighted. Tissues were digested using a mixture of hydrofluoric acid (OPTIMA grade, Fisher Scientific), ultrapure hydrogen peroxide (OPTIMA grade, 30%, Fisher Scientific), and nitric acid (OPTIMA grade, 70%, Fisher Scientific) at volume ratio of 3-1-1 to break down the organic matter. Then, silica contents were analyzed by ICP/MS.

Histology (colon and its histological score evaluation)

In addition, the main tissues including tumors, livers, kidneys, spleens, lungs, and hearts from the B16-F10 tumor model and distal sections of colonic tissues from the colitis model were fixed in 10% formalin and then embedded in paraffin. 4 μm thick tissue sections were prepared and then stained with hematoxylin-eosin (H&E). The safety evaluations in tissue slices were conducted by an experienced veterinary pathologist.

The histological scores of colonic tissues were assessed in a blinded manner in terms of the inflammation severity (none; 0, slight: 1, moderate: 2, and severe: 3), PMN infiltration/HPF (less than 5: 0, 5-20: 1, 21-60: 2, 61-100: 3, and more than 100: 4), injury depth (none: 0, mucosa: 1, submucosa and mucosa: 2, and transmural: 3), crypt damage (none: 0, basal 1/3: 1, basal 2/3: 2, only surface epithelium intact: 3 and total crypt lost: 4), and adjusted to the tissue involvement multiplied by the percentage factor (0−25%: x1, 26−50%: x2, 51−75%: x3, and 76−100%: x4).

Immunohistochemistry (IHC) staining

Murine GI-associated tissue, small intestine (ileum region with Peyer's patch), small intestine (ileum region with lymphoid follicle), mesenteric lymph nodes (ileum region), liver, and spleen were harvested. Gut-associated lymphatic tissues were rinsed with warm PBS and embedded and frozen in OCT tissue blocks. Tissues were hand-cut to 10-micron thin using a Leica cryo-sectioning machine. Sliced tissues were mounted onto a TruBOND micro slide glass and stained with primary antibody (Abcam, mouse anti-F4/80, anti-M-cell, anti-LYVE-1 antibody) at 4°C overnight in a dark, humid container to avoid sample dehydration or photobleaching. The primary antibody-treated samples were gently washed with PBS and stained with secondary antibody (Abcam, Alexa 594 goat anti-mouse) for 1 hour at room temperature. Then, samples were gently washed with PBS and sealed using a glass cover with sample mounting solution (Fluoromount-G™ Mounting Medium, with DAPI, Invitrogen). Samples were visualized under a Nikon AX/AX R confocal microscope.

TEM tissue Ultra-Microtome

Mesenteric lymph nodes, spleen, and liver harvested from the mice gavaged with MSN@YF were embedded in EMBed 812 resins, transitioning from 100% ethanol to propylene oxide (25%, 50%, 75%, 100%, 1-hour in-between step, respectively). Then, samples were placed in fresh 100% resin and in an appropriated polypropylene mold. Polymerization of Embed 812 was taken placed in a 60°C oven overnight. Hardened blocks are trimmed and sectioned on an ultramicrotome (RMC/Boekeler, Tuscon AZ) to a thickness of approximately 50 nm (gold or silver appearance). Then, the sectioned samples were collected and placed on a copper grid, post-stained with uranyl acetate for 30 minutes, lead citrate for 5 minutes, and visualized under TEM.

Statistical analysis

Data are expressed as mean ± SD. Differences between groups were analyzed using Student's t-test when comparing only two groups. Differences among more than two groups were analyzed using one-way analysis of variance, and the Bonferroni post hoc test was used to analyze the differences between any two groups. $P < 0.05$ was considered representative of a statistically significant difference. GraphPad Prism 8 was used to perform the statistical analysis.

Synthesis of sodium diselenide

Sodium diselenide was synthesized via reacting 2 mmol (320 mg) of Se powder (Sigma Aldrich) with approximately 4 mmol (150 mg) of sodium borohydride (Sigma Aldrich) in a flask of 2 mL of DI water. Complete dissolution was marked by the generation of hydrogen and resulted in a colorless solution within 5 minutes. The flask was then sealed via a rubber plug and heated to 70°C for 20 minutes until the solution turned dark red. Next, a solution of 4 mmol (0.68 g) benzyl bromide (Sigma Aldrich) in 5 mL of THF (Sigma Aldrich) was injected into the flask under argon flow and then the reaction was allowed to continue at 50°C for 12 hrs. The resulting product, dibenzyldiselenide, was extracted through chloroform (Sigma Aldrich) and dried via anhydrous $MgSO_4$. Dibenzyldiselenide was dissolved in 5 mL of THF and added to 0.15 g of sodium borohydride. After stirring for 10 minutes, the solution turned colorless and a 5 mL solution of 4 mmol (1.0 g) 11-bromoundecanol in 5 mL THF was added. The flask was then incubated at 50°C overnight. Finally, the reaction mixture was extracted in chloroform and dried with anhydrous $MgSO_4$. The product was purified by column chromatography via chloroform and then via diethyl ether.

4.3 Results

SA3. Development of microbiome-based formulations for oral drug and gene

SA3.1 Prepare and characterize microbiome-based formulations

First, we harvested the live Baker's yeast and stripped and pierced the yeast cell wall to remove the internal components (cytoplasm) through acid/base extractions and washes (**Figure 24a**). Based on the DLS analysis, the hydrodynamic size of the yeast ghost was larger than the yeast, which may be due to the varied refractive indexes of different components presenting on the outer surface of yeast ghost from the yeast. The larger size could also be explained by infiltration of liquid into some of the yeast ghosts, whereas the live yeasts are impervious to water and retain their 3D oval shape in water solution. Nevertheless, these results need to be further substantiated by other methods. In terms of morphology, the yeast ghost has a hollow internal structure with a lower electron conductivity compared to the unprocessed yeast, shown in SEM images (**Figure 24d**).

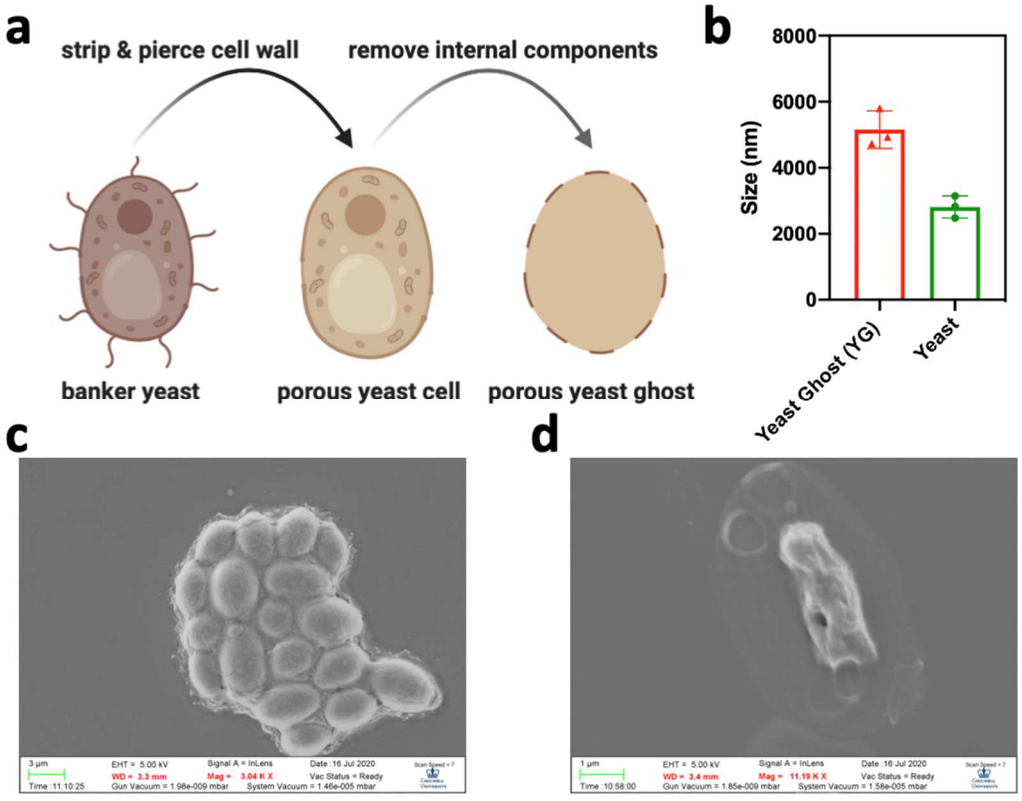

Figure: Characterization of yeast-based microformulation. (a) Illustration of yeast ghost preparation process, (b) DLS size analysis of the Baker's yeast and yeast ghost, (c) SEM image of Baker's yeast, (d) SEM image of the processed yeast ghost.

Next, we tested the feasibility of using the diffusion-based *in situ* process to formulate drug-loaded PLGA NPs (drug/PLGA@YG) directly within the yeast ghost in a facile manner (**Figure 25**). The *in situ* nanoformulation and the drug loading within the yeast ghosts were characterized and validated in two therapeutic models, the murine IBD model and cancer models. Studies described in this section are a proof-of-concept for developing a diffusion-assisted protocol for efficient, scalable, and reproducible preparation of biomimetic oral therapeutics.

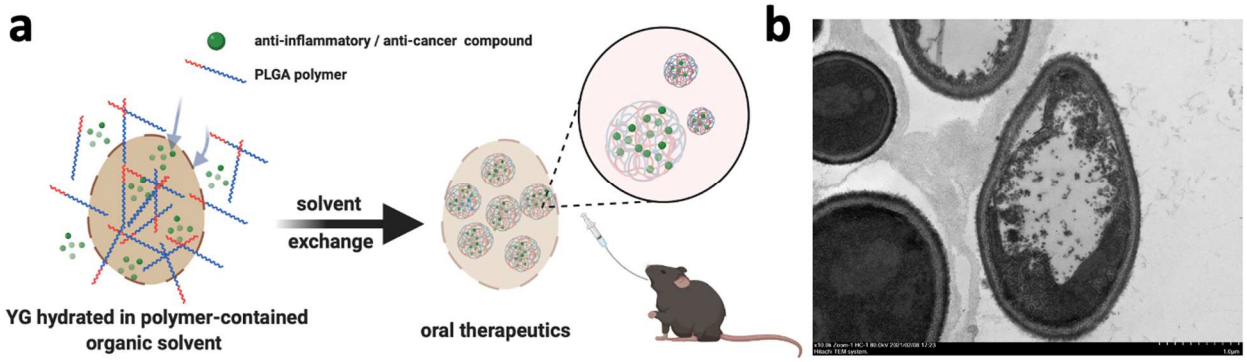

Figure 25: (a) Schematic of preparing drug-loaded yeast-based microformulation (5-ASA/PLGA@YG), and (b) Ultra-microtome TEM image of a 5ASA/PLGA@YG.

The first step was to explore the optimal condition for assembling the PLGA NP formulation within the YG. YGs are synthesized using an acid-base extraction method with a slight modification. The DLS, SEM, and TEM revealed that the intact yeasts have an oval shape and size of around 4 µm (**Figure 24b**), whereas the YGs exhibit a flat body with an empty cavity available for cargo encapsulation. We performed the TEM ultra-microtome to visualize the loading of PLGA NPs within the YG (**Figure 25b**). For oral delivery, the most important aspect is whether the oral carriers can overcome the inclement environment of the GI tract and deliver therapeutics to the desired site. To investigate the therapeutic potential of this yeast-based formulation, we carried out our first functional test on a disease model, IBD. 5-ASA (amino-salicylic acid), an anti-inflammatory compound commonly used to treat this chronic ailment, was selected. Due to the hydrophilic nature of 5-ASA, this organic acid avidly binds to the gut mucosa and is also susceptible to degradation when inundated under gastric acid[144,145]. Encapsulating 5-ASA-loaded PLGA NPs within the YG could potentially protect the drug from degradation and improve its bioavailability. Thus, we formulated the 5-ASA-loaded PLGA NPs directly inside the YG in a single step through *in situ* nanoformulation. This process was achieved through combining YGs with the polymer-drug solution by slow mixing of the PLGA-

5ASA solution and the YG. Specifically, water serves as the anti-solvent and penetrates the budding scar on the yeast through diffusion, forming 5-ASA-loaded PLGA NPs as supersaturation takes place. Compared to the conventional loading protocol, where the drug-loaded NPs were prepared first and then added to YGs through electrostatic interaction, *in situ* formulation prevents excessive YG surface attachment, thereby improving the loading efficiency. The TEM and SEM images show that there are more NPs present within the YG (electron conductivity difference), suggesting a better cargo encapsulation of the *in situ* nanoformulation method (**Figure 26**, bottom row) than the conventional loading method (**Figure 26**, top row). When comparing the drug loading of the *in situ* to the conventional formulation methods, the 5-ASA contents were quantified by UV-vis spectroscopy. The quantified 5-ASA loading levels of the *in situ* and the conventional formulations were about 13 ± 1.4% and 11% ± 2.1%, respectively. To further compare the difference in loading efficacy of the two methods. X-ray diffraction (XRD) was performed to validate the cargo loading within the YGs (**Figure 27**). Based on the XRD result, there may be more 5-ASA PLGA NPs attached to the outer surface of the YGs when prepared by conventional loading method, where the XRD curve behaves more similarly to the pure 5-ASA curve. Most of the crystalline peaks of the 5-ASA became weak and disappeared, suggesting encapsulation of the drug in YGs. However, another possible explanation for seeing more prominent peaks of the conventional loading group could be that 5-ASA diffused out from the carrier and adhered to the outer surface of the YGs. The difference in the magnitudes of the crystal peaks of the 5-ASA between the drug-loaded yeast formulation and the original 5-ASA may be due to the change in the crystal form of the drug during the re-precipitation step. The data of the *in situ* formulation method show a more amorphous curve, but also preserves the small peaks of the 5-ASA, suggesting there may be less cargo leaking

compared to the conventional loading method. However, the discrepancy in the XRD results from two yeast-based formulations might also be partially due to the final drug concentration difference after lyophilization and handling. HPLC and other analytical methods are needed to confirm the drug loading and release profiles under different conditions more accurately. Moreover, in terms of the DLS results, a more negatively charged surface for the conventional loading group could imply the adequate presence of PLGA NPs on the YGs outer surface than the *in situ* formulation group, despite there being no significant difference in size between the two groups (**Figure 28a, b**). Of note, we tested the integrity of the yeast ghost in a PBS solution of pH 2. Over a week of the pH 2 PBS treatment, the integrity of the yeast ghost-based microformulation has been conserved. The size and the zeta potential of the empty or drug-loaded yeast ghost-based microformulations did not change in pH 2 PBS solution (**Figure 28c, d**), suggesting the stability of the carrier in an acidic environment. Importantly, cargo release is crucial for successful drug delivery. We compared the release profile of 5-ASA of the YG formulation among the conventional loading, *in situ* formulation, and the bare PLGA NPs (**Figure 28e**).

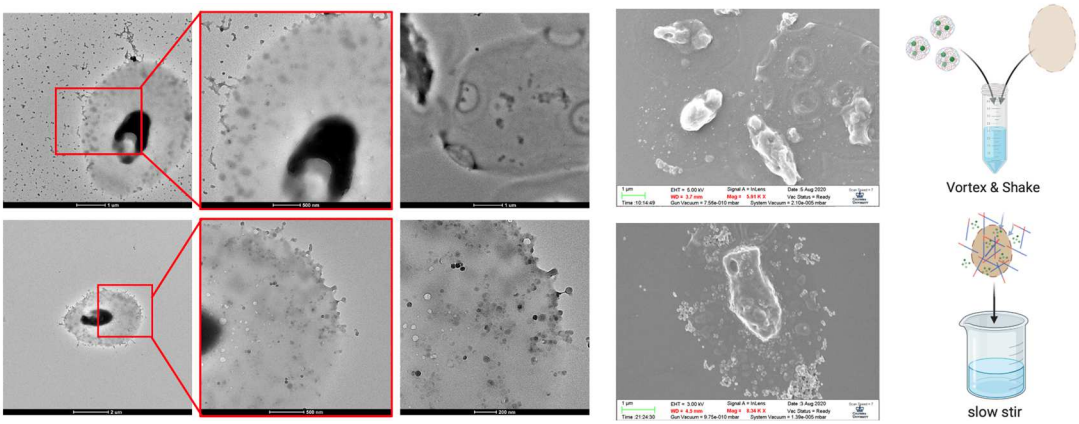

Figure 26: Drug loading comparison between the conventional loading (top row) and the *in situ* formation (bottom row) characterized by TEM and SEM.

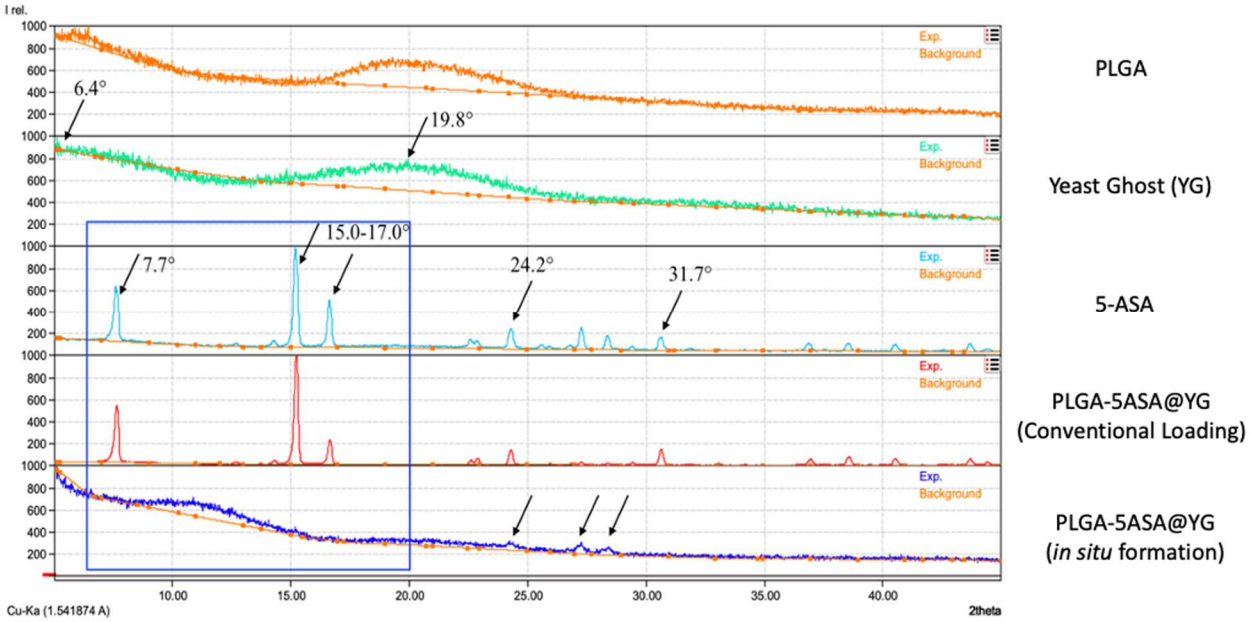

Figure 27: XRD analysis of the drug loading profile of PLGA NP, yeast ghost (YG), 5-ASA alone, PLGA-5ASA@YG through conventional loading, and PLGA-5ASA@YG through *in situ* formation loading.

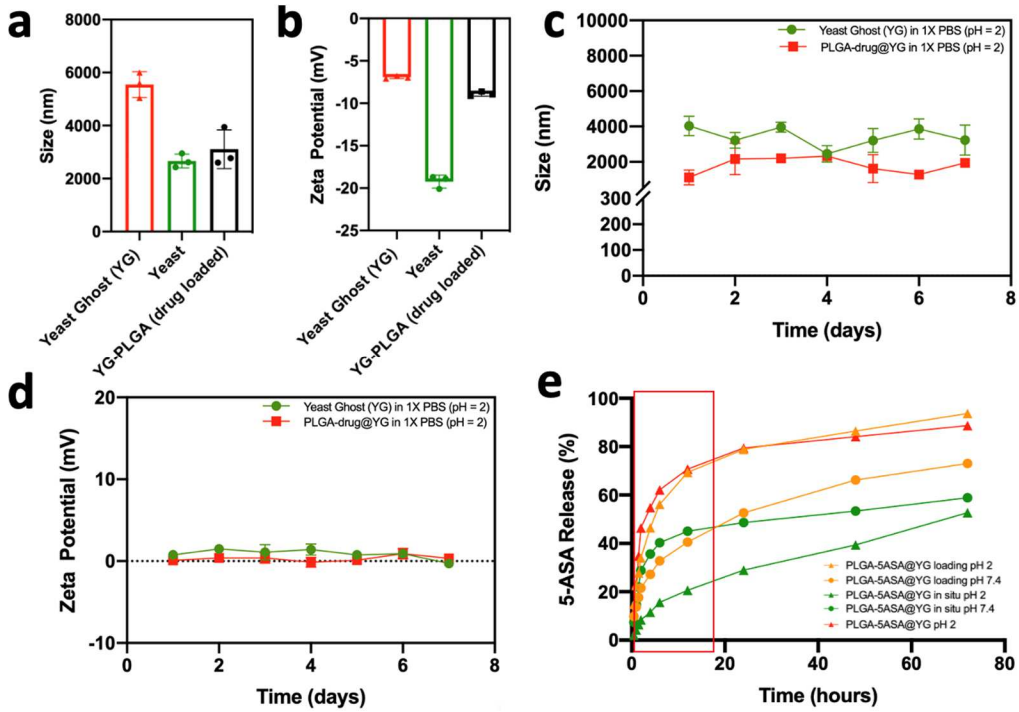

Figure 28: DLS (a) size and (b) zeta potential analysis of the YG, live yeasts, and 5-ASA/PLGA@YG, (c) colloidal stability of YG 5-ASA/PLGA@YG in pH 2 PBS solution, and (d) change of the zeta change of YG and 5-ASA/PLGA@YG in pH 2 PBS solution, and (e) the 5-ASA release profile of different formulations under pH 2 or pH 7.4.

SA3.2 In vitro and in vivo study of therapeutic efficacy of yeast-based formulation

* Data in this section were collected with the help of Dr. Dan Shao, Dr. Chao Yang, and Dr. Mingqiang Li

When designing an oral drug delivery system for systemic circulation in the bloodstream, drug-loaded YGs should be capable of crossing the gut epithelium. From a mechanistic perspective, the β-glucan of the yeast, which is a form of polysaccharide that is also pathogen-associated receptor pattern (PAMP), can avidly bind to the dectin-1 receptor abundantly present on macrophages[146–148]. According to recent literature reports, the systemic drug delivery of the YG-based microformulation can be achieved through M-cell mediated transcytosis and macrophage-mediated translocation of the endocytosed formulation to the Peyer's patches to enter the blood circulation. To confirm our yeast-based microformulations can achieve systemic delivery, we first evaluated the *in vitro* uptake of YG-based microformulation by murine macrophages (RAW 264.7). The internalization peak started at 6 h after incubation and started to decrease after 12 h (**Figure 29a**). Next, we validated the macrophage-targeting selectivity of YG-based formulations (conventional preparation versus the *in situ* formulation) by quantifying the *in vitro* uptake profiles on RAW 264.7, Caco-2, and 4T1. At 6 h, the highest uptake of YG-based micro-formulations was observed in macrophages (RAW 264.7), while both microformulations significantly dwindled in Caco-2 and 4T1 cell lines, possibly due to the decreased number of β-glucan receptors on their extracellular membrane. Importantly, a higher uptake efficiency of *in situ* yeast-based formulation was observed for all three cell lines than the formulations prepared by the conventional method (**Figure 29b**). We speculate that the higher

uptake of the yeast-based system formed by *in situ* nanoformulation could be partially due to the lower amount of PLGA NPs present on the YG surface, where they might hinder the interaction between β-glucan and dectin-1 receptors. However, further studies need to be carried out to validate this statement.

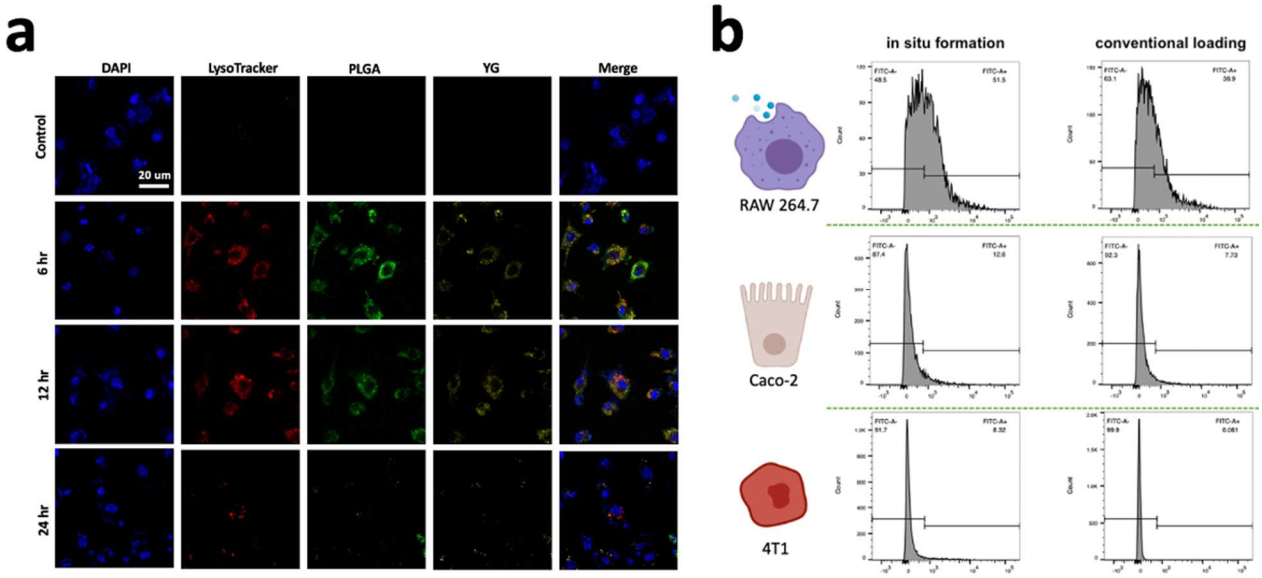

Figure 29: (a) Confocal fluorescence images of PLGA@YG uptake in RAW 264.7 cells, (b) FACS quantification of PLGA@YG uptake profiles in RAW 264.7, Caco-2 and 4T1 cell lines.

Colon retention and mucosa penetration of the anti-inflammatory drug in important when treating IBD[149,150]. Before evaluating the *in vivo* therapeutic efficacy of yeast-based *in situ* formulation, we analyzed the biodistribution of these microcarriers. The fasting mice were orally administered with a single dose of the fluorescence-labeled yeast-based formulations. After 12, 24, and 48 h, we collected the liver and large intestine for *ex vivo* IVIS imaging analysis (**Figure 30**). The fluorescence signals of yeast-based microformulations prepared by both methods were detected in the liver as early as 12 h, suggesting that the yeast-based microformulations entered the bloodstream after oral administration. Notably, at 12 h, the *in situ* formulation shows a stronger fluorescence intensity in the liver than the conventional counterpart, implying the *in situ*

formulations had an enhanced capability of crossing the gut epithelium and entering the bloodstream. This can be explained by the presence of fewer PLGA NPs on the outer shell of the YG so that the cellular translocation recognition was affected to a lesser extent. In addition, a smaller number of PLGA NPs attaching to the outer surface of the YG could also render less cargo loss when they penetrate the gut mucosa and are transported into the Peyer's patch and subsequently into the blood circulation. Since the Indocyanine Green (ICG) amounts in both formulations were kept constant, the tightness of NPs associated with the yeast ghost, either the number of NPs that were encapsulated inside the yeast ghost or attached to the yeast outer surface, may directly affect their fluorescence intensity after passing through the upper GI.

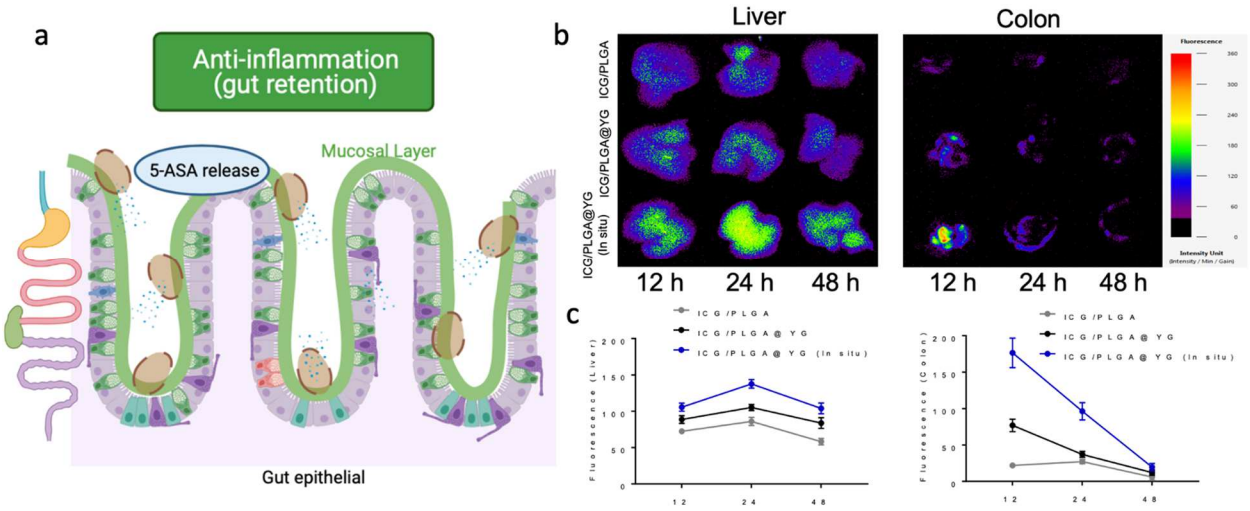

Figure 30: (a) Schematic illustration of yeast-based microformulation for treating murine IBD, (b) *ex vivo* fluorescence images of the mouse liver and colon after administration of yeast-based formulations orally, (c) quantification of fluorescence intensity in the harvested mouse liver and colon.

To demonstrate the therapeutic efficacy of the yeast-based microformulation, we tested the anti-inflammatory effects of different microformulations (YG, 5-ASA@YG, 5-ASA/PLGA NPs, 5-ASA/PLGA@YG prepared by conventional loading or *in situ* formulation) on a DSS-induced IBD murine model. We measured the blood inflammation cytokine levels on day 0 and

day 14 after treatment. We observed a significant drop in IL-1beta, TNF-alpha, and IFN-gamma secretions among all 5-ASA treated groups (**Figure 31a-c**). Consistent with the biodistribution data, the yeast-based microcarriers prepared by the *in situ* process led to the most prominent inflammation mitigation *in vivo*. Besides the speculation that there is less nanoparticle dissociation from the yeast ghost while passing the upper GI, the inflammatory environment and loosening of the colon epithelium may also lead to more active interaction between APCs and yeast-based formulations. APCs reside in lamina propria, which is right beneath the colon epithelium may as well contribute to a decreased pattern of secreted inflammatory cytokines. However, more data are needed to corroborate this statement. In addition, we carefully monitored the colon length of all treatment groups. Colon length is an important marker of disease recuperation. The mice with chronic inflammation have shortened colons, and the length of the colon is often proportional to the severity of the inflammation. Although the exact mechanism of colon shortening under the DSS-induced IBD model has not been fully elucidated, researchers speculate mucosal ulceration, neutrophilic infiltration, and disruption of epithelial tight junction all contribute to the colon shortening[151,152]. The mice treated with *in situ* microformulations have the longest colon length when compared to all other treatment groups. Of note, the colon length of the *in situ* mice groups are nearly like the lengths of the negative control group, which indicates an effective of anti-inflammation treatment (**Figure 31d, Figure 32a**).

Furthermore, we also tabulated the DAI scores and the bodyweight of all treatment groups. DAI monitors mice by the frequency of diarrhea, number of intact crypts presented in the colon, number of liquid stools, and general well-being of animals (**Table 1**). We found that among all groups, the *in situ* therapeutic group has the lowest DAI scores and less body weight

loss than the untreated group (**Figure 31e, 31f**). Overall, the 5-ASA encapsulated PLGA NP-loaded YG microformulation was the most effective in treating the IBD mice. In future works, we will further dissect the gut-associate lymphatic tissues (GALT) to study the mechanism and detailed biodistribution of the yeast-based microformulation after oral administration of the yeast-based formulations. Despite the fact that the positive results are shown in Figures 31 and 32 and DSS-induced murine IBD is a relatively simple and reproducible model to evaluate therapeutic formulations, the DSS-induced IBD model lacks chronic features of the long-term developed inflammation. Also, DSS-induced IBD does not involve T or B cells responses, and luminal bacteria and other microbiomes also contribute to the disease progression and may affect the model accuracy in evaluating different therapeutic formulations.

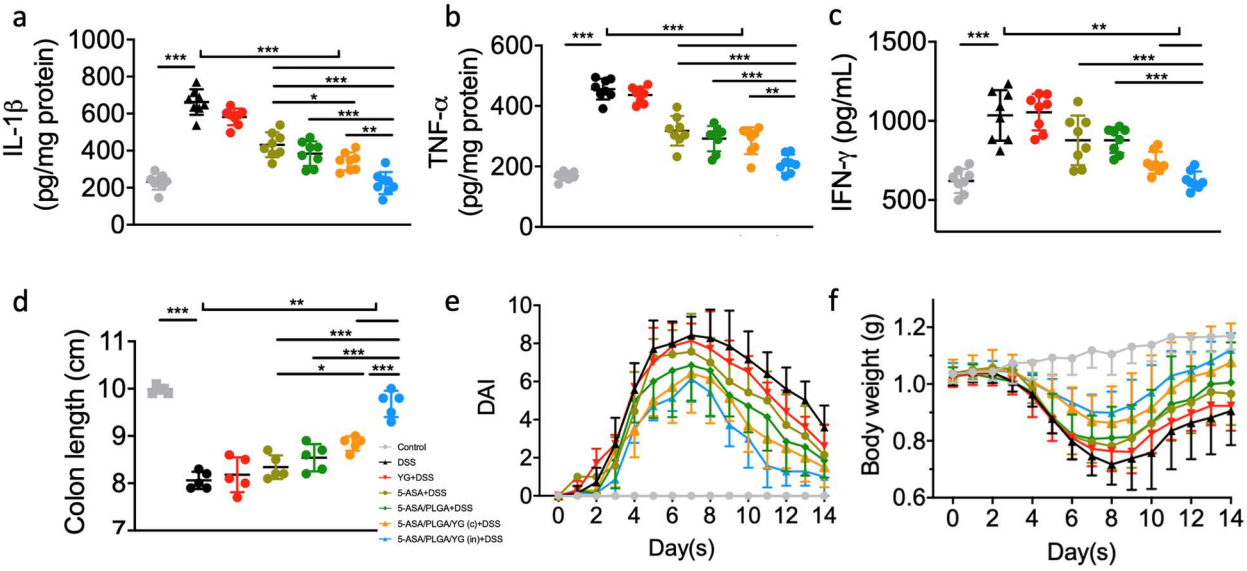

Figure 31: Secreted inflammatory cytokine level of (a) IL-1b, (b) TNF-a, (c) IFN-g, and (d) colon length, (e) DAI, and (f) mouse body weight of the negative control group, DSS-treated group, yeast ghost DSS-treated group, 5-ASA and DSS-treated group, 5-ASA/PLGA NP treated group, YG loaded with 5-ASA/PLGA NPs formed through the conventional method, and YG loaded with 5-ASA/PLGA NPs formed through the *in situ* formation method.

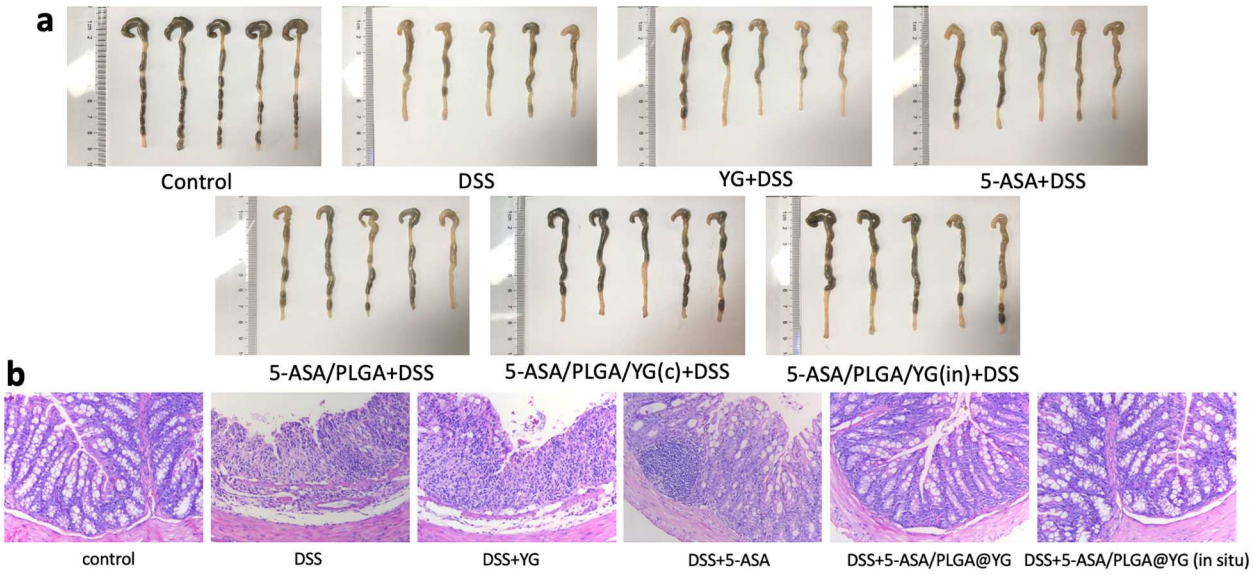

Figure 32: (a) Murine colon length images of the various control and treatment groups, (b) histology images of the various control and treatment groups.

Histology Score

Feature scored	Score	Description
Percentage Involvement	10	0%
	20	1-25 %
	30	26-50 %
	40	51-75%
	50	76-100%
Inflammation Level	10	None
	20	Mucosa
	30	Mucosa and submucosa
	40	Transmural
Inflammation Severity	10	None
	20	Mild
	30	Moderate
	40	Severe
Crypt Damage	10	None
	20	Basal 1/3
	30	Basal 2/3
	40	Crypts lost but surface epithelium remains
	50	Both lost of Crypts and surface epithelium

Disease Activity Index (DAI)

Score	Body weight loss (%)	Diarrhea	Fecal bleeding
0	none	normal	none
1	1–5		
2	6–10	loose stools	slight
3	10–15		
4	>15	diarrhea	fecal blood

Table 1: Histology score assessment (left) and DAI assessment (right).

To further demonstrate the potential of the yeast-based microformulation on oral therapeutics, we also explored the possibility of oral delivery of cancer therapeutics using the

yeast-based microformulation. To evaluate the tumor treatment efficacy of the yeast-based microformulation, we carried out the same *in situ* and conventional loading methods to encapsulate cisplatin, a cancer chemotherapeutic drug that also can be tracked effectively in murine organs. We compared the yeast formulation prepared by the *in situ* (CDDP/PLGA/YGin) and conventional methods (CDDP/PLGA/YGc) to the cisplatin-loaded PLGA NPs (CDDP/PLGA) as well as the free cisplatin (CDDP), YG alone, and the PBS control group on the tumor-bearing mouse model. From the collected tumor, we observed that both (CDDP/PLGA/YGin) and (CDDP/PLGA/YGc) groups significantly inhibited the tumor growth compared to the YG and free CDDP groups in terms of the tumor size, weight, and volume (**Figure 33 a-c**). These data suggest the yeast-based microformulations have better gut epithelial penetration, and the amount of the encapsulated cisplatin that can be delivered to the tumor sites through blood circulation is higher than the cisplatin alone group. Although promising, long-term safety evaluations such as the effect of this oral-based yeast formulation on GI function and how it affects other vital organs need to be evaluated.

Moreover, the time required for the remaining yeast-based formulation to be cleared from the body is also worth exploring. To understand how the CDDP levels change in tumors and the colon, we harvested the tumors and the colon from the mice and performed ICP/MS to quantify the CDDP level in the organ. At the 24 h timepoint, the tumor CDDP amount in the (CDDP/PLGA/YGin) group is significantly higher than any other group. We also observed a similar pattern in the colon samples. However, at the 48 h timepoint, the CPPD amount in (CDDP/PLGA/YGin) group dropped sharply and this was universal to the other study groups (**Figure 33d, e**). These data imply that the *in situ* formulation process encapsulates more CDDP inside the YG, and CDDP can be effectively transported through the blood and accumulate at the

tumor site. However, since the amount of the CDDP was constant among all treatment groups, the amount of the CDDP diminished after 24 h in the colon suggests that the majority of all the formulations had been eliminated from the mouse GI tract. This result is consistent with other oral delivery studies regarding the mouse GI transition time.

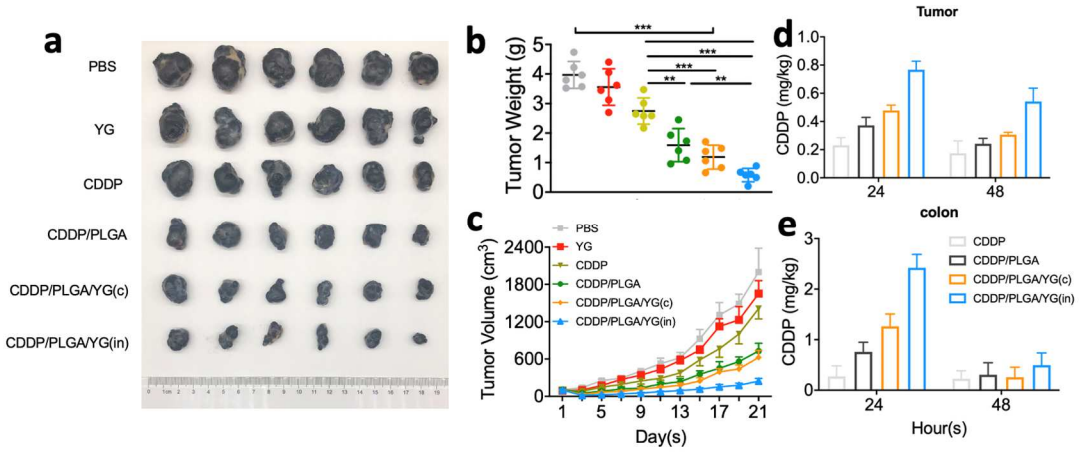

Figure 33: Oral administration of Cisplatin-PLGA@YG inhibits tumor growth in breast tumor bearing mice. (a) Image of excised tumors from different control and treatment groups, (b) tumor weight and (c) tumor volume from different control and treatment groups, and the quantitative analysis of the cisplatin from different treatment groups in (d) tumors and in (e) colons harvested from mice.

We also applied another common cancer drug, DOX, to the yeast-based microformulations to test the versatility and the robustness of this biomimetic carrier in treating murine breast tumor. Similar anti-tumor effects were observed in terms of the collected tumor size and weight (**Figure 34**).

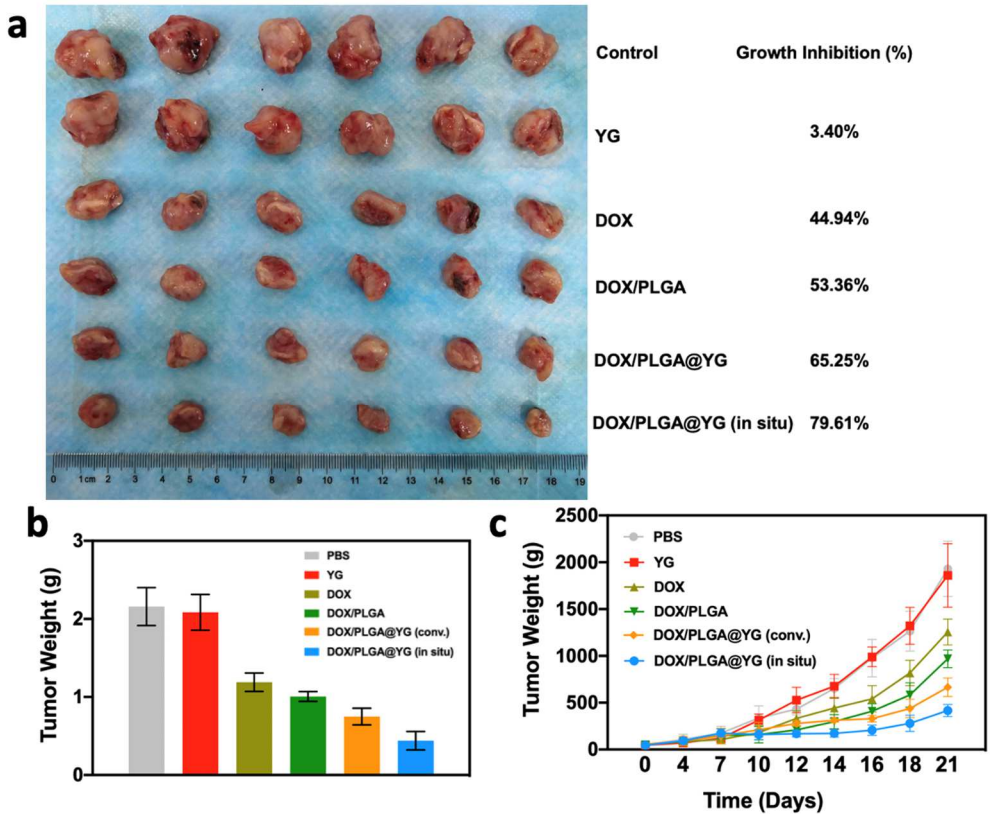

Figure 34: Oral administration of DOX-PLGA@YG inhibits tumor growth in breast tumor bearing mice. (a) Image of excised tumors from different control and treatment groups, (b) tumor weight and (c) change of the tumor weight from different control and treatment groups.

We collectively demonstrated the possibility of using the processed YG for loading polymer NPs that encapsulate drug molecules for IBD and cancer treatment. The *in situ* polymerization method can load a number of drug-loaded NPs within the YG, and its therapeutic efficacy was demonstrated to be superior to the yeast-based microformulation formed by the conventional loading method. However, the loading level of the formulation needs to be further quantified using more accurate analytical methods besides UV-vis. The better therapeutic outcome of the *in situ* yeast-based microformulation in both IBD and cancer models suggests it may have the less premature release of the drug molecule as the yeast-based microformulation passes through the GI tract and circulates in the bloodstream before reaching the tumor site. On

the other hand, the conventional method of loading drug-encapsulated NPs onto the YG solely relies on electrostatic interaction. We speculate that there may be many NPs attached to the outer surface, instead of the inner cavity of the YG. Hence, during circulation and interaction with the negatively charged intestinal mucus, the outer surface NPs may fall off. However, this hypothesis has yet to be proven. More studies need to be carried out to quantify the loading efficacy more accurately and investigate whether there is a premature release of drug molecules from the formulation under different simulated gut fluids.

SA3.3. In vitro and in vivo demonstration of yeast-based nanoformulations for oral delivery

The yeast cell wall is majorly composed of glycoproteins, mannoproteins, β-glucans, and chitin, and bounded with a plasma membrane layer (**Figure 35b**)[137,139,153–155]. Different yeast strains have distinctive compositions and a variety of polysaccharide sizes[21,156,157]. According to previous research, the polysaccharide composition and size play disparate roles in immune recognition and activation[139,147,158]. Coating NP surfaces with polysaccharides derived from the yeast may endow the nanoformulation specific cellular uptake functions in APCs and subsequent immune activation. We hypothesize that upon fragmenting the YG we previously derived from Baker's yeast, we could cloak these sub-nanometer wall fragments onto NPs. We explored the derivation of the yeast fragment from the YG using two methods. We first homogenized the YG and processed them in a freeze-miller, and then collected the powder to undergo another event of chemical digestion. Through centrifugation, we collected and evaluated the size of the obtained fragmented products. The tested yeast fragment size ranges from 20 nm to several hundred nanometers (**Figure 35a**).

Further modification of the fragmentation process is still needed for a standardized procedure and optimal yield. The YGs derived from the live Baker's yeast appears to be ivory and brown in color. After hours of freeze milling of the YG, the YGs were pulverized into nanometer fragments. Of note, color can be an indicator of the yeast fragment size. The smaller the fragments are, the whiter in color the yeast fragment powder tends to be. The size of the collected yeast fragments was also revealed under TEM characterization (**Figure 35c**), and the β-1,3-glucan composition of the derived fragments was confirmed by NMR (**Figure 35d**) and MALDI-TOF (**Figure 35e**).

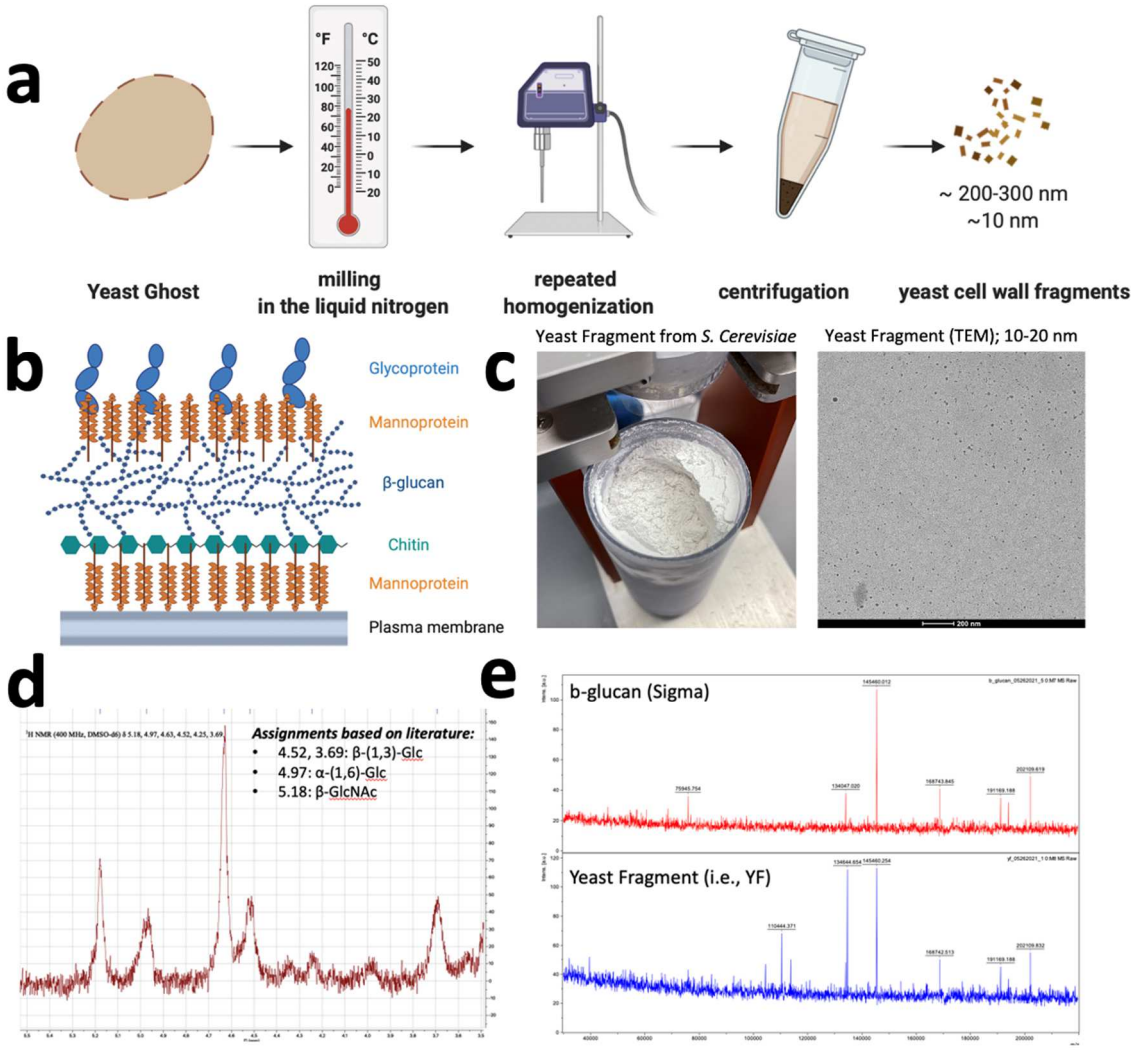

Figure 35: (a) Derivation process of yeast cell wall fragments. (b) Illustration of components of the Baker's yeast cell wall. (c) Image of the harvested yeast fragments in dry powder form and the TEM image of the yeast fragments. (d) H NMR analysis of the yeast fragments. (e) MALDI-TOF analysis of the beta-glucan from Sigma and yeast fragments.

A nanoparticulate system has the advantage of a high volume-surface ratio. Also, NPs can be tuned to have different surface charges, degradation profiles, and other endowed functionalities. We hypothesize that coating the derived yeast fragments onto a NP surface can endow the NP with enhanced intestinal epithelium penetration via specific binding to the phagocytotic receptor dectin-1 on the M-cell surface (**Figure 36b**). Because of the advantage of high surface area, pore-volume, and biodegradability, the di-selenide MSN has been selected for the yeast fragment coating. The di-selenide MSNs were also exploited and discussed in Chapters 2 and 3. The first step was to characterize the coating of yeast fragments onto the mesoporous silica NPs. Based on TEM images, the surface of the bare MSN is porous. The MSN surface becomes less porous after the yeast fragment coating due to the electron conductivity of the bare MSNs (**Figure 36a**).

Moreover, the Brunauer-Emmett-Teller (BET) analysis was performed to quantitively measure the specific surface area of the bare and yeast fragment-coated MSN. The BET reads the physical adsorption of the gas molecules on the biomaterial surface and reports its surface area and pore volume. After yeast fragment coating, a decrease in surface area and pore volume suggests successful coverage of the yeast fragments onto the MSN surface (**Figure 37a**).

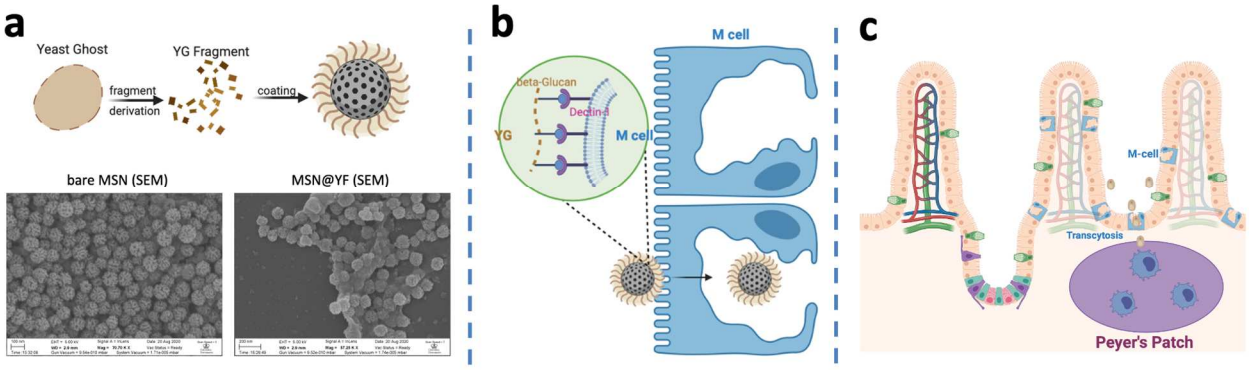

Figure 36: Illustration of yeast cell fragment coating and its application for oral delivery. (a) Illustration of yeast fragment coating onto MSN (top row) and SEM image of the bare MSN and yeast fragment-coated MSN (bottom row). (b) Beta-glucan on the yeast cell wall can be recognized by the M-cell on the intestinal epithelium for yeast fragment-coated MSN to cross the gut epithelium. (c) Route of the yeast-based formulations crossing the M-cell and enter the Peyer's patch.

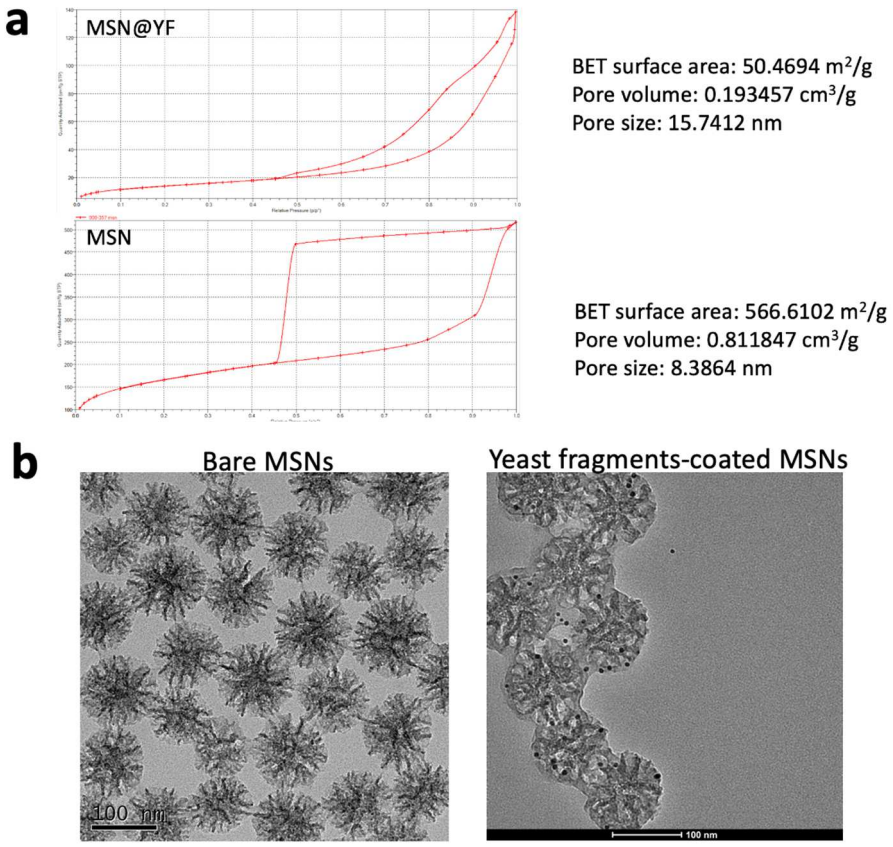

Figure 37: Yeast fragment coating characterization. (a) BET analysis of bare MSN and yeast fragment-coated MSN. (b) TEM image of bare MSNs (left) and immune-gold labeled yeast fragment-coated MSNs (right).

Importantly, validation of the polysaccharide presence after coating is essential to the subsequent functional studies. Immune-gold staining studies were conducted to further confirm the coverage of the yeast fragments on the MSN surface (**Figure 37b**). The coated MSNs were treated and washed with 1% BSA solution to block unspecific binding. The primary anti-β-glucan antibody was used to label the β-glucan on the MSNs surface. Then, the secondary antibody conjugated with 6 nm gold NPs was used to visualize the coating using TEM.

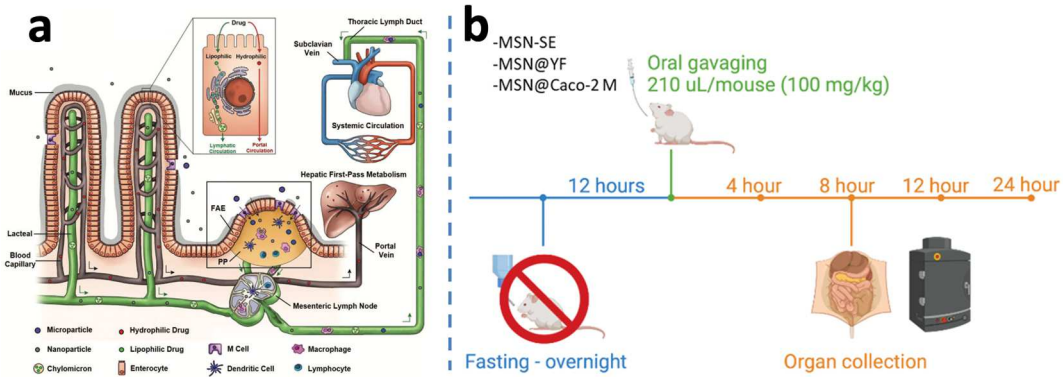

Figure 38: (a) Intestinal lymphatic system (ILS) transport of drug delivery vehicle. (Reprinted with permission from Ref[57]. 2021, Wiley.) (b) Schematics of oral delivery of fluorescence-labeled bare MSNs, MSN@YF, MSN@Caco-2 M for IVIS biodistribution.

It is critical to know whether the yeast fragment coating can render a nanoparticulate system functions of specific cellular uptake and immunogenic responses by performing *in vitro* uptake studies and *in vivo* biodistribution studies. We evaluated the capability of the yeast fragments-coated MSNs to cross the gut epithelium via M-cells and enter the systemic circulation through the gut-associated lymphatic tissue (GALT), the largest lymphoid tissue in the body[133,148,159]. The evidence of the MSN@YF entering the bloodstream was corroborated by the biodistribution study of the fluorescence-labeled MSN@YF after oral gavage of the mice. Specifically, the mice were fasted overnight to avoid food fluorescence interference before oral gavage. Three different groups, bare MSNs, MSNs coated with the yeast fragments (MSN@YF),

and MSNs coated with Caco-2 cell membrane (MSN@Caco2), were compared for biodistribution. Four different time points, 4, 8, 12, and 24 h post-gavage periods, were assessed. After sacrificing the mice, the entire mice's GI tract, mesenteric lymph nodes, and other major organs were harvested (**Figure 39-41**). Based on the quantified fluorescence signal, we observed that the fluorescence signal of the MSN@YF was higher than the MSNs group in the mesenteric lymph nodes and the liver at many time points. To further confirm the presence of the MSN@YF in GALT, immunohistochemistry (IHC) was performed on the harvested murine Peyer's patches (ileum region of the small intestine) and mesenteric lymph nodes (**Figure 42**). The histology data confirmed the presence of MSN@YF in M-cell, lymphatic vessels, and Peyer's patch.

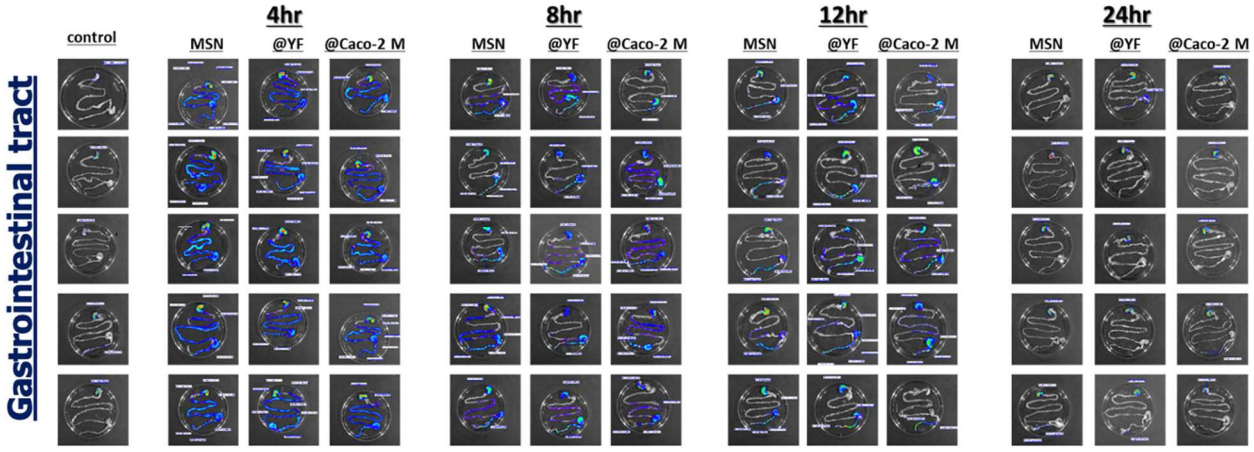

Figure 39: *Ex vivo* IVIS image of the mouse GI tracts for bare MSN, MSN@YF, and MSN@Caco-2 membrane, respectively with different oral gavage timepoints. MSNs were covalently labeled with Cy5.5 fluorescence dye.

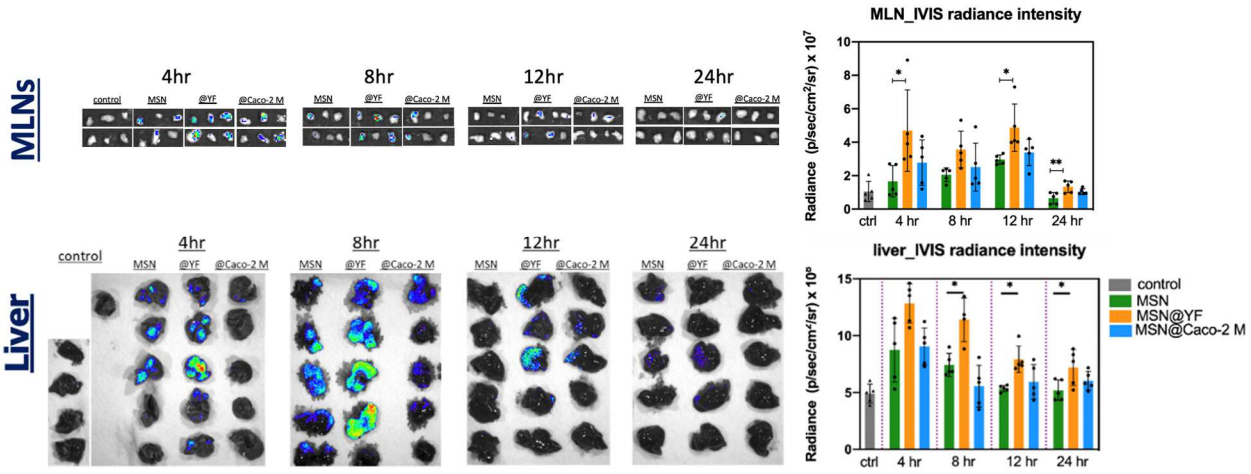

Figure 40: *Ex vivo* IVIS images and the quantified radiance of the mouse mesenteric lymph nodes (top row) and mouse livers (bottom row) for bare MSN, MSN@YF, and MSN@Caco-2 membrane, respectively with different oral gavage timepoints. MSNs were covalently labeled with Cy5.5 fluorescence dye.

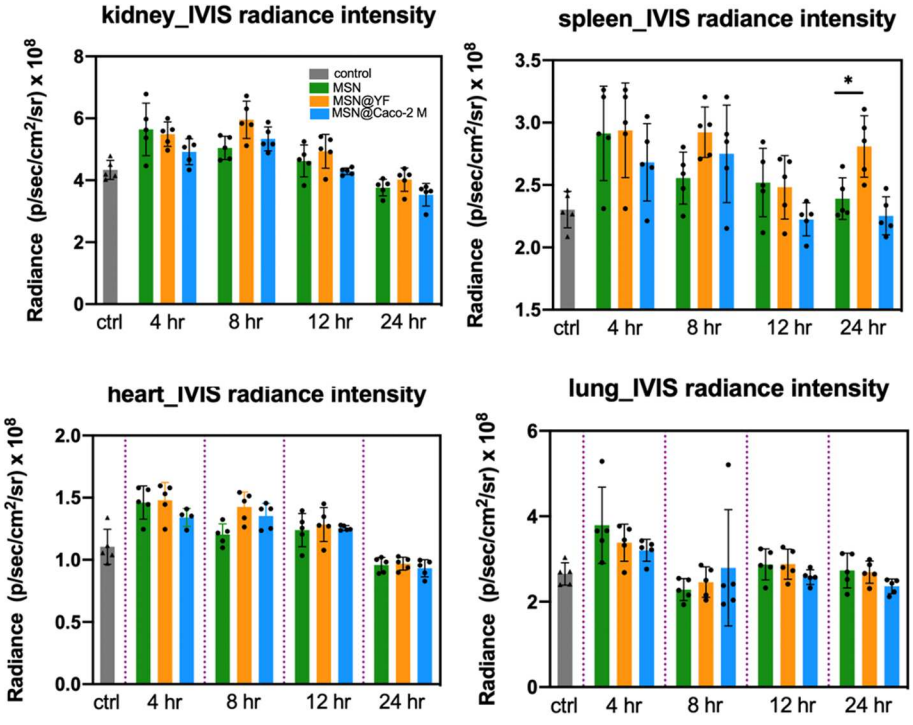

Figure 41: Quantified *ex vivo* IVIS results of the mouse kidneys, spleens, hearts, and lungs for bare MSN, MSN@YF, and MSN@Caco-2 cell-membrane, respectively with different oral gavage timepoints. MSNs were covalently labeled with Cy5.5 fluorescence dye.

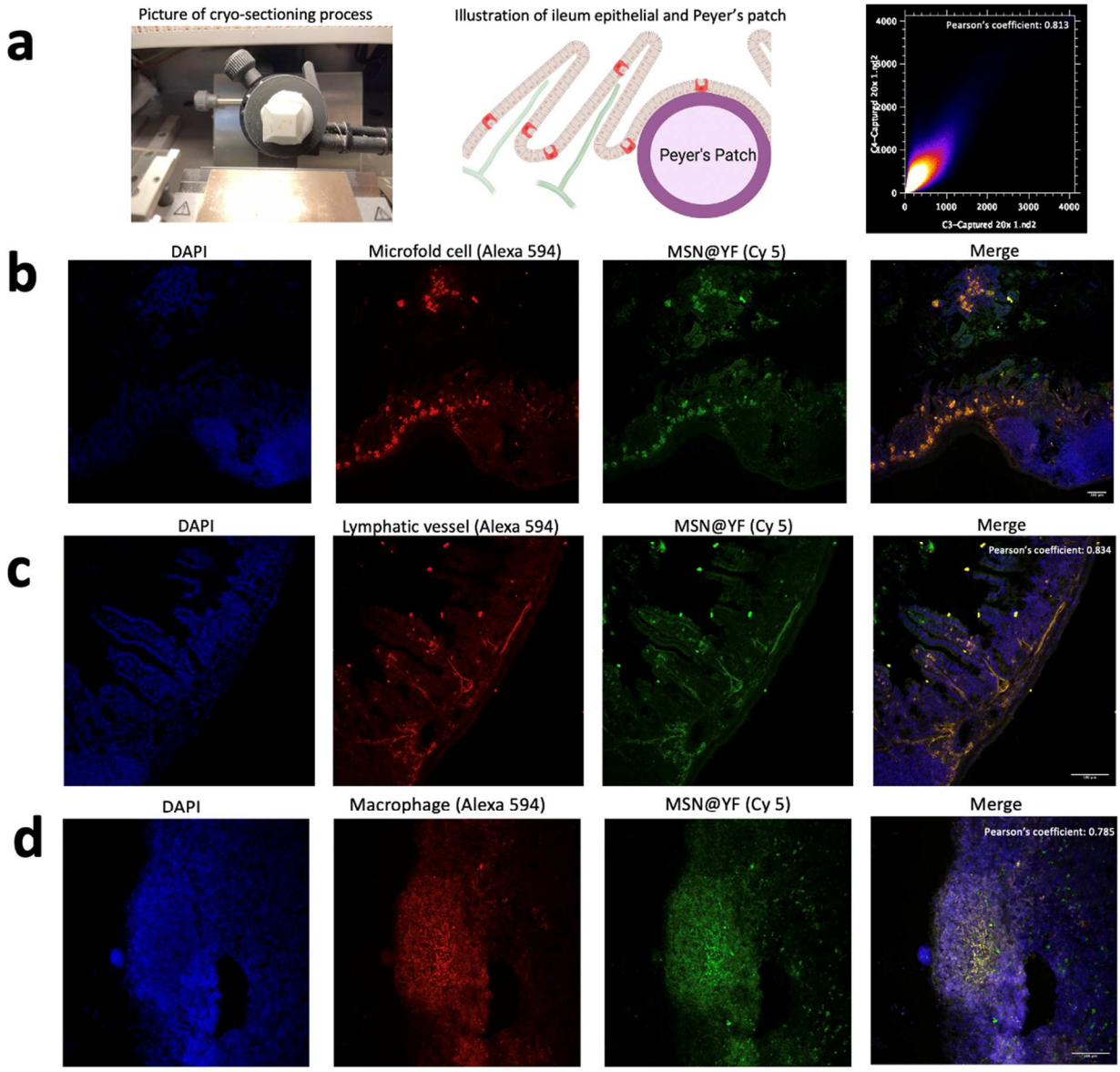

Figure 42: IHC results of the mouse GALT tissue after oral gavage the mouse with MSN@YF. (a) Image of operating the cryo-sectioning for histology preparation (left), illustration of the ileum region and Peyer's patch of the harvested histology sample (middle), and confocal images of the mouse ileum region and Peyer's patch (right) and their colocalization with (b) microfold cells, (c) lymphatic vessel, and (d) the confocal images of the mouse MLNs.

To further validate the hypothesis that yeast fragment-coated MSNs were transported through M-cells and entered the GALT and systemic circulation, we performed an *in vivo* laminarin inhibition study (**Figure 43**). Laminarin is also a polysaccharide that can competitively

bind to the dectin-1 receptor on the M-cells[137,141]. The mice were pre-treated with laminarin before oral gavage with MSN@YF. Based on the *ex vivo* IVIS results, we observed a significant decrease in the fluorescence intensity of the MSN@YF in the mesenteric lymph nodes and the kidney. These results suggest the yeast fragments on the MSN surface facilitate the transport of the MSN@YF through M-cell's specific recognition of β-glucan of its dectin-1 receptors. However, there is no significant difference in the fluorescence intensity between the MSN@YF with and without laminarin treatment. One possible explanation could be that there might be other endocytosis pathways that also grant the transport of the nanoformulation through the gut epithelium to enter the bloodstream, or the non-significance might be due to the large variability amongst the animals, especially through the *p.o.* route.

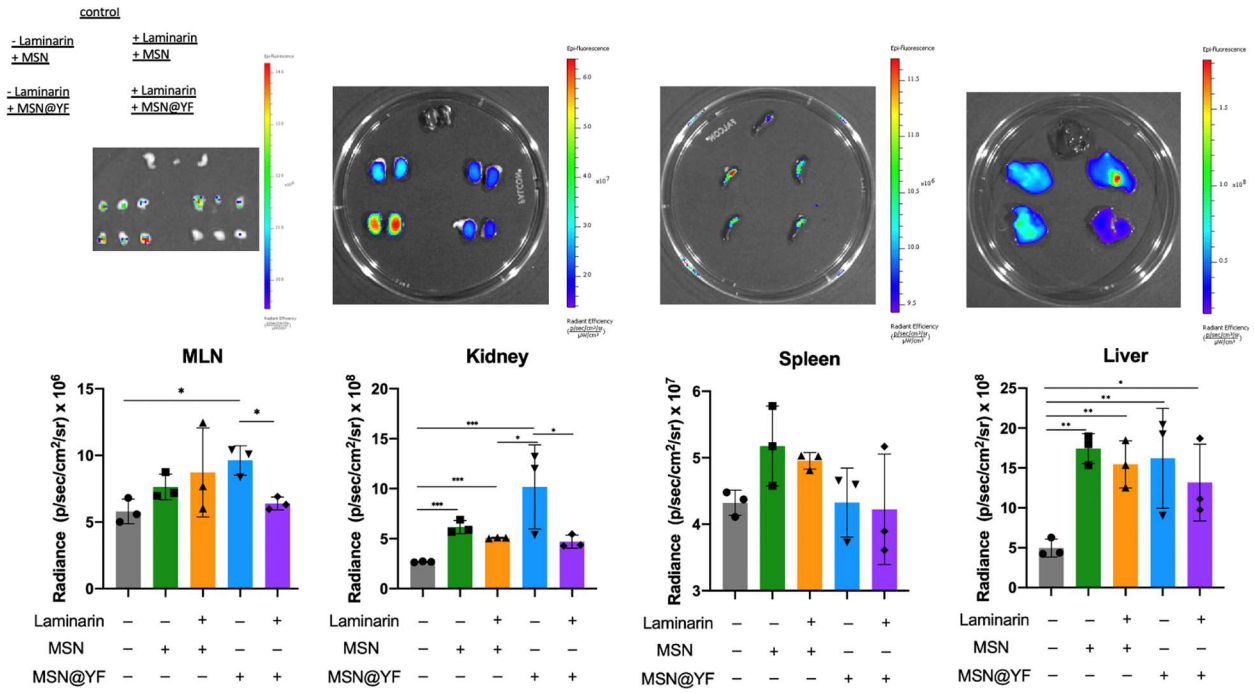

Figure 43: Images and quantified *ex vivo* IVIS result of the mouse MLN, kidney, spleen, and liver for the negative control, MSN, and MSN@YF treated with or without beta-glucan inhibitor laminarin, respectively.

To build a fully functional nanoformulation, we can also place immune-activation cargo (STING agonist, antigen, immunogenic drug compound) into the NP or covalently attach them to the yeast fragment. In addition, due to the presence of chemokines and growth factors produced by cancer and stromal cells in the tumor microenvironment, most monocytes are M2-type of the tumor-associated macrophage (TAM), which promote tumor angiogenesis, metastasis, and immunosuppression[157,160,160–165]. In contrast, the M1 phenotype fosters inflammation responses against invading pathogens and tumor cells. The M1/M2 ratio has a significant association with cancer progression and patient survival[122,162,166,167]. With the presence of β-glucan on the yeast fragment surface, we hypothesize the macrophages can be converted to an M1 phenotype after incubating them with the yeast-fragment coated functional NP core. We carried out the quantitative polymerase chain reaction (qPCR) to assess macrophage polarization. By screening the M1 and M2 markers, it is shown that the yeast fragment-coated NPs tend to polarize the macrophages into the M1 type, rather than the M2 type (**Figure 44**). Yeast fragments serve as a potent adjuvant for immune recognition. Coating MSNs with yeast fragments also renders the MSNs targeting function. Developing a nanosystem with immunostimulant antigen, adjuvant, and an effective carrier by exploiting the synergism between the high loading capacity of the MSNs and the M-cell targeting yeast fragments, we can utilize this potent system for oral immunomodulation. For future studies, we need to perform drug loading experiments to further characterize fragment-based nanoformulation, *in vitro* immunogenic validation, and *in vitro* therapeutic efficacy. Most importantly, *in vivo* demonstration is needed of the yeast fragment-based nanoformulations on cancer vaccination and immunomodulation when combined with immune checkpoint blockade therapy (**Figure 45**).

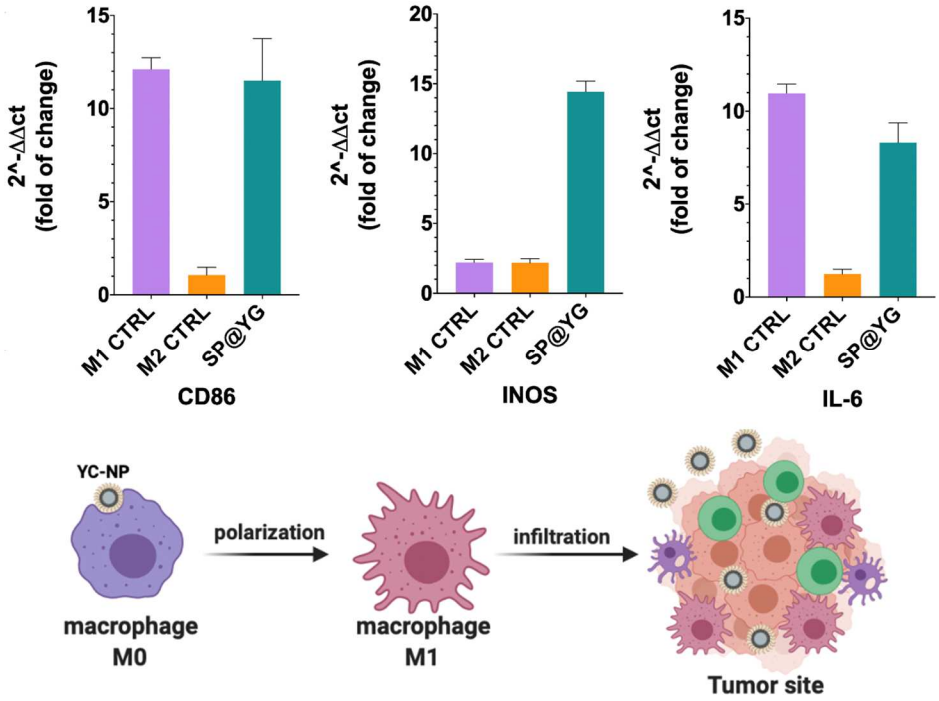

Figure 44: qPCR results of the macrophage-type-1 associated gene (top row) and schematic illustration of utilizing the yeast fragments-coated MSNs for macrophage polarization (bottom row).

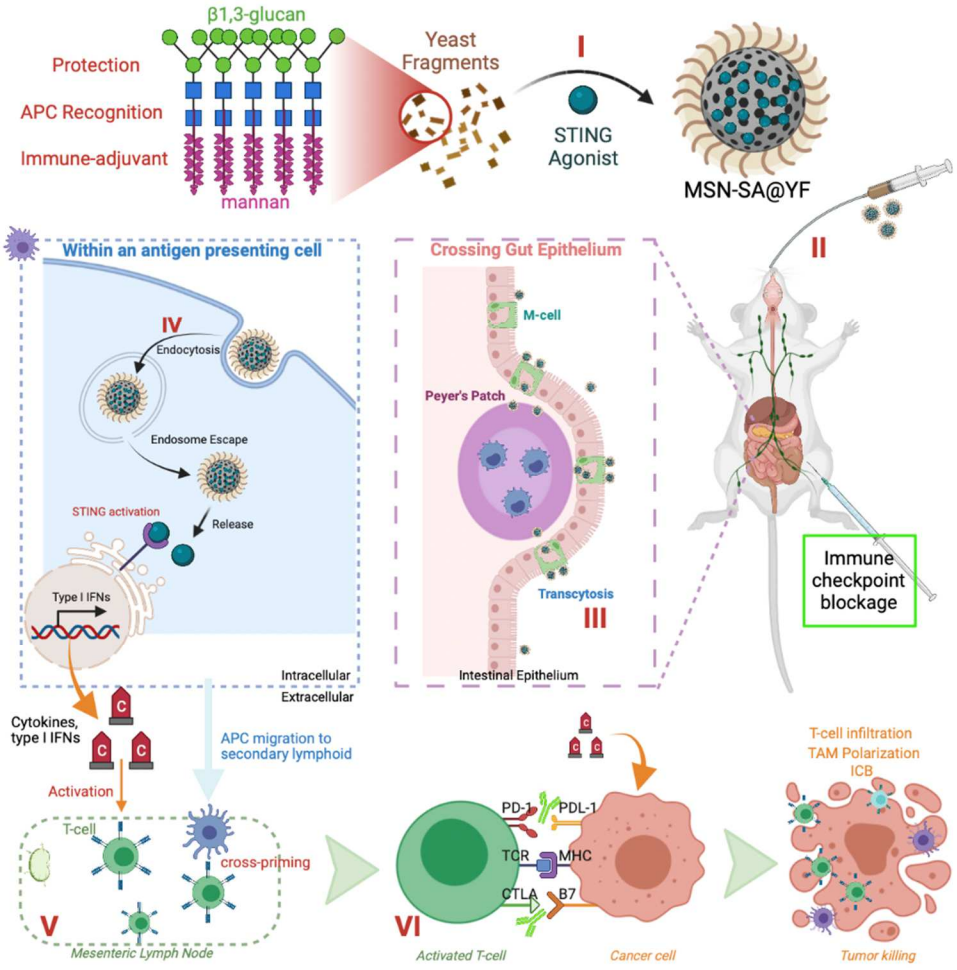

Figure 45: Schematic illustration of utilizing the yeast fragment-coated MSNs for oral cancer immunomodulation.

4.4 Discussion

This chapter explores the possibility of using yeast-based formulations for oral drug delivery. The ability to effectively deliver small molecular drugs through the oral route provides unique advantages for treating inflammation and cancer. Resisting a harsh pH environment and being able to penetrate the gut mucosal barrier are crucial to the delivery vehicle for successful cargo shipment and ideal therapeutic outcomes. We constructed a yeast-based ghost to carry the anti-inflammatory agent 5-ASA or cancer-treating drugs as the stealth transport platform. The *in*

situ nanoformulation of drug laden PLGA NPs within the YG renders it good drug loading potency. The *in situ* nanoformulation effectively loads the capsule with NPs and prevents excessive NPs from attaching to the yeast surface. With adequate cargo loading and the acid-resisting YG serving as the micron-size shield, *in vitro* experiments demonstrate that the yeast-based microcapsules are preferred and rapidly endocytosed by macrophages.

The enhanced drug loading through *in situ* nanoformulation makes the oral capsule favorable in ameliorating the inflammatory conditions on murine IBD models and improves the treatment outcomes of tumor-bearing mice. The synergic effect of *in situ* nanoformulation and biomimetic strategy makes the engineered oral platform a promising remedy for IBD and breast cancer. Moreover, due to the advantage of the particle size being in the nanometer range, coating processed yeast cell wall fragments onto a NP can endow the NP with the specific targeting capabilities and improve the bioavailability of the API encapsulated within the NPs. This is the first time, to our knowledge, of reporting the use of yeast cell wall fragments for NP coating. Beta-glucan assay, TEM, SEM, DLS, and BET analysis were used for coating validation. However, the coating efficiency and the verification of the β-glucan needs to be further characterized and studied. We also performed the laminarin inhibition study and verified that the β-glucan of the yeast fragments binds explicitly to the dectin-1 receptors on the M-cells for transportation of the MSN@YF across the gut epithelium.

Moreover, the mesenteric lymph nodes, Peyer's patch on the illume region of the small intestine, and other vital organs were harvested and prepared for IVIS imaging and IHC. The results collectively corroborate our hypothesis that yeast fragment coating enhanced NP transportation into the lymphatic tissue and entrance into the bloodstream. Because β-glucan is a form of the PAMP, the yeast fragment-coated MSNs have enhanced accumulation in the

secondary lymphatic tissues. Antigens and adjuvants can either be encapsulated inside the MSNs or be conjugated to the surface of the yeast fragments through a chemical linker. The potential of yeast-based nanoformulation is awaiting to be explored for oral immunomodulation and therapy.

Chapter 5: Conclusions and Future Work

In this thesis, we designed and optimized various biomimetic platforms for use in different contexts, spanning different cell targets and routes of administration. To fulfill future clinical translation and industrial requirements, we designed, modified, tested, and fabricated flash-based self-assembly systems to tackle the challenges of limited production and batch-batch variation issues. We managed to provide an attractive medical platform for lipid-based nanoformulations and cell-membrane-coated cancer immunotherapy with our flash-based systems. We also explored the potential of yeast-based formulations for administering anti-inflammatory and anti-cancer therapeutics orally.

In the first aim, we manufactured a line of flash devices made of different configurations, materials, and fabrication methods. First, we performed computational fluidic dynamics to study the shear stress and mixing profile of our modified MIVMs. Based on the simulation, we finalized the 2-D and 3-D layouts of the modified MIVM for manufacturing reference. The two-inlets and three-inlets CIJM were manufactured at machine shop according to the previous designs. Other than machine shops, we also explored more acid-resistant manufacturing materials and utilized 3D printing to fabricate the flash devices to demonstrate our effort of bridging our bench-top research to future clinical translation for massive production of our flash-based system. In speaking of the formulating homogeneous NPs, due to the highly dynamic mixing of flash chambers, the polycationic and polyanionic biomaterials can be complexed into polyplexes continuously and homogeneously. Two- and three-inlet CIJM devices are more suitable for making polyplexes or lipoplexes by controlling the equal flow rate of all inlets, which were well studied in the field. NP coating and when more than two materials are involved, MIVM was devised to overcome the limitation of the equal momentum of the flows in the CIJM.

The flow of each MIVM inlet can be independently adjusted for a more complex nanoformulation. For the first time, the MIVM was explored for coating lipids onto the functionalized MSNs, leading to improved physical characteristics like colloidal stability. The first significant test of our platform was to achieve consistent, reproducible, and scalable lipid-coated MSNs. *In vitro* results also provide an ideal cellular uptake profile. Compared to the bulk mixing of the lipid coating of MSNs, which often involves multiple steps of preparation, our FNC process is a single-step and highly consistent protocol to coat lipid onto MSNs. The lipid-coated MSNs prepared by FNC has better particle colloidal stability in solution than its bulk-mixing counterpart. This enhanced particle stability suggests a more uniform and homogeneous coating of the FNC process than the bulking mixing method. For the first time, we demonstrated the concept of utilizing the flash-based platform for NP coating with the potential to close the gap between benchtop research and future clinical translation. However, acquiring biological or chemical functions of a formulation by coating synthetic lipid onto NPs can still be limited by the complex design of functional lipids. Most cationic lipids have the issue of high toxicity. Screening an ideal ionizable lipid requires much of the computational power and synthesis expertise. Also, ideal membrane fluidity, PEGylated lipids, and other functional lipids need to be well balanced for optimal particle stability, desired targeted function, ideal cellular uptake, endosomal escape, and minimized cytotoxicity. When it comes to biomimicry, a top-down approach can be more strategic and reasonable than the bottom-up process.

To further explore the versatility and robustness of the flash-based system for coating, we exploited the cell membrane for particle coating. Essentially, cell membranes are lipids with different proteins. Cell membrane naturally contains a variety of membrane-bound proteins and glycans that serve as targeting or immune-evasive moieties depending on different cell sources.

We began the cell membrane coating validation by extracting different types of cell membranes and selected particles with distinctive size, surface charge, and surface morphologies. Encouragingly, the coating results showed that the cell membrane-coated particles by the flash-based platform also have better colloidal stability and size consistency compared to the conventional coating method. Further, we selected the small pore biodegradable MSN to be the core and coated it with the cell membranes derived from melanoma cancer cells. By extracting the cell membrane directly from melanoma cells, all the membrane-bound proteins can be preserved. These proteins serve as potent anti-tumor antigens that can be transferred to our nanoparticulate system. We verified the presence of cancer antigens on the cell membrane surface via Western blotting and SDS-PAGE gel electrophoresis. We also loaded the MSNs with an immunoadjuvant, CpG, which is a TLR-9 antagonist. Together with the tumor antigens and immune-stimulating adjuvant, the cell membrane-coated MSNs are potential vaccines for melanoma immunotherapy. The *in vitro* confocal fluorescence colocalization verified the integrity of the cell membrane-coated formulation. The therapeutic readout, *in vitro* cytotoxicity, and *in vivo* health markers such as alanine transaminase and weight were noted accordingly. Results were promising as there was no significant toxicity, owing to the relatively good biocompatibility and the biodegradability of the MSNs.

Further, the combined effects of flash-based coating and the co-stimulation from the antigen and adjuvant in a high spatial-temporal resolution was synergistic and more potent than the nanoformulation formulated by the conventional coating method, indicative of the robustness of the flash-based system for formulating cell membrane-coated MSNs for cancer immunotherapy. Because of this specific, scalable capability of the flash-based platform, it has been used in the context of multiple biomimetic strategies in different cell membrane types. The

flash-based platform can potentially be automated and explored for sequential coating of NPs, which can be used for a variety of biological applications not limited to therapeutics. Because of the utility of the flash-based platform, future work done by our lab or collaborators could also employ the system for complexing polyplexes and different biomaterials other than cell membranes for particle coating. With the aid of future automation and computational power, a feedback-responsive flash system has the potential for mass production of cell membrane-coated nanotherapeutics. Membrane-bound tumor antigens can be well harnessed for future precision medicine. Direct derivation of cell membranes from tumors preserved all the neo-antigens from the tumor tissue. Such a personalized biomimetic strategy can be applied to localized tumor therapy as well as to distant sites in the body that are prone to metastases for aggressive tumor treatment. Patient-derived cell-membrane-based nanovaccines coupled with genome analysis offer a unique opportunity for the therapies of individual cancer patients. Further, by performing transcriptomics analysis, we could understand how our adaptive immune systems work at the cellular level. Moreover, DNA barcoding can track the presence of NPs at a single-cell level. This can help us understand which immune cell types were involved in different immune-activating functions in tumor microenvironments. As our immune system is complicated and ever-changing, studying interactions between immune cells and cancerous cells at high spatial and temporal resolutions is highly valuable. The combination of flash technology, cell membrane coating, and gene sequencing will enlighten the future of precision medicine.

Besides the lipid and cell membrane coating, another biomimetic strategy exploring the Baker's yeast for oral drug and gene delivery offers new insights into nanotherapeutics. Compared with other synthetic systems, the yeast cell wall of Saccharomyces cerevisiae contains a specific amount of β-glucan with an ideal chain length and a molecular weight that can be

utilized for targeted oral delivery[168]. The β-glucan on the yeast cell wall particularly binds to the dectin-1 receptors on the M-cells of the small intestine to initiate the transport. Pulverizing the yeast cell wall into fragments and coating them onto MSNs make this nanoformulation ideal for enhanced gut epithelium penetration, lymphatic tissue targeting, and entering the blood circulation. The *in vivo* biodistribution and IHC data verified this targeting pathway and validated the yeast-based formulation's potential for oral delivery.

There is ample room for engineered yeast-based nanotherapeutics to develop, as many groups are continuously working on defining and refining the microbiome-based methodology for meeting industry-wide benchmarks. The natural polysaccharides and proteins displayed on the yeast surface serve as the ideal immune-stimulating adjuvants or antigens when developing an oral vaccine system. Furthermore, native yeast cell walls can be engineered to enhance targeting and therapeutic approach by genetic or chemical approaches. Besides, there are a number of yeast strains that can be screened for different delivery purposes. Considering the size of many yeasts are in the range of 2-10 microns, which could not be absorbed completely or may cause uninvited inflammation when administrating intramuscularly or intraperitoneally, pulverizing yeast cell walls of the selected or genetically engineered strains and coating the yeast fragments onto NPs represents new strategies for not only oral delivery of therapeutics, but as potential vaccines could be compatible for many administration routes. By taking advantage of the cost-effectiveness of yeast production, yeast-based formulations may provide a feasible foundation for developing safe and effective therapeutics and vaccines for treating many diseases. Importantly, the choice of an animal model is crucial to accurately evaluate the therapeutic potential of a particular formulation. The differences in physiology, metabolism rate, residing microorganisms, and behaviors between mice and humans must be considered when

explaining the obtained data. Also, experimental results associated with different administration routes should be explained independently before making the universal conclusion since therapeutic effects on mice can be disproportionally related to their human counterpart depending on how the formulations are administered. For example, the enhanced permeability and retention (EPR) effect has long been the paradigm corroborating solid tumor treatment in nanomedicine since the 1980s[169–171]. Owing to the leaky vasculature, rapid and chaotic angiogenesis, and poor lymphatic drainage in the tumor, better operability of nanoparticulate therapeutics can accumulate in these tumors. However, the non-stellar performance of claimed EPR effect of nanoparticulate systems in many late-phase clinical trials led researchers to question its accuracy and appropriateness for humans. The heterogeneity of vasculature among species and different tumor types requires scientists to revisit this EPR paradigm, and it is time to embark on fundamental studies on how NPs interact with the tumor in a comprehensive manner. Biomimetic formulations are promising strategies when it comes to engineering an ideal system for interacting with the complicated physiological environment.

These works demonstrate a small step in closing the gap between benchtop research and clinical translation. Scalable production, minimal batch-to-batch variation, safety, and targeted delivery routes are essential for a successfully marketed nanotherapeutic. Further, the optimization process for each biomimetic strategy provides valuable insight into the design of nanomedicines. Convergence of nanotechnology, fabrication technique, computational aid, material science, bioengineering, and pharmaceutical perspectives can help reduce cost, diminish the gap between fundamental research and clinical translation, and eventually bring the merits of nanotherapeutics to patients.

References

[1] J. Ahn, J. Ko, S. Lee, J. Yu, Y. Kim, N. L. Jeon, *Advanced Drug Delivery Reviews* **2018**, *128*, 29.

[2] J. Sun, L. Zhang, J. Wang, Q. Feng, D. Liu, Q. Yin, D. Xu, Y. Wei, B. Ding, X. Shi, X. Jiang, *Adv. Mater.* **2015**, *27*, 1402.

[3] J. Ding, J. Chen, L. Gao, Z. Jiang, Y. Zhang, M. Li, Q. Xiao, S. S. Lee, X. Chen, *Nano Today* **2019**, *29*, 100800.

[4] M. Durán□Lobato, Z. Niu, M. J. Alonso, *Adv. Mater.* **2020**, *32*, 1901935.

[5] Y. Chen, M. Chen, Y. Zhang, J. H. Lee, T. Escajadillo, H. Gong, R. H. Fang, W. Gao, V. Nizet, L. Zhang, *Adv. Healthcare Mater.* **2018**, *7*, 1701366.

[6] S. K. Alsaiari, S. S. Qutub, S. Sun, W. Baslyman, M. Aldehaiman, M. Alyami, A. Almalik, R. Halwani, J. Merzaban, Z. Mao, N. M. Khashab, *Sci. Adv.* **2021**, *7*, eabe7174.

[7] V. E. Lee, C. Sosa, R. Liu, R. K. Prud'homme, R. D. Priestley, *Langmuir* **2017**, *33*, 3444.

[8] A. K. Andriola Silva, R. Di Corato, T. Pellegrino, S. Chat, G. Pugliese, N. Luciani, F. Gazeau, C. Wilhelm, *Nanoscale* **2013**, *5*, 11374.

[9] C.-M. J. Hu, L. Zhang, S. Aryal, C. Cheung, R. H. Fang, L. Zhang, *Proceedings of the National Academy of Sciences* **2011**, *108*, 10980.

[10] S. Bhatia, in *Natural Polymer Drug Delivery Systems*, Springer International Publishing, Cham, **2016**, pp. 33–93.

[11] J.-M. Lim, A. Swami, L. M. Gilson, S. Chopra, S. Choi, J. Wu, R. Langer, R. Karnik, O. C. Farokhzad, *ACS Nano* **2014**, *8*, 6056.

[12] Y. Liu, C. Cheng, Y. Liu, R. K. Prud'homme, R. O. Fox, *Chemical Engineering Science* **2008**, *63*, 2829.

[13] S. F. Chow, C. C. Sun, A. H. L. Chow, *European Journal of Pharmaceutics and Biopharmaceutics* **2014**, *88*, 462.

[14] X. Chen, T. Shi, C. Yang, F. Chen, X. He, K. Zhang, H. Hu, L. Cai, K. W. Leong, D. Shao, *Sig Transduct Target Ther* **2022**, *7*, 96.

[15] N. Anton, F. Bally, C. A. Serra, A. Ali, Y. Arntz, Y. Mely, M. Zhao, E. Marchioni, A. Jakhmola, T. F. Vandamme, *Soft Matter* **2012**, *8*, 10628.

[16] R. De Smet, T. Demoor, S. Verschuere, M. Dullaers, G. R. Ostroff, G. Leclercq, L. Allais, C. Pilette, M. Dierendonck, B. G. De Geest, C. A. Cuvelier, *Journal of Controlled Release* **2013**, *172*, 671.

[17] S. Allen, O. Osorio, Y.-G. Liu, E. Scott, *Journal of Controlled Release* **2017**, *262*, 91.

[18] Y. Chen, K. Ai, J. Liu, G. Sun, Q. Yin, L. Lu, *Biomaterials* **2015**, *60*, 111.

[19] M. C. Koetting, J. F. Guido, M. Gupta, A. Zhang, N. A. Peppas, *Journal of Controlled Release* **2016**, *221*, 18.

[20] M. Martínez-Carmona, D. Lozano, M. Colilla, M. Vallet-Regí, *Acta Biomaterialia* **2018**, *65*, 393.

[21] T. Jiang, B. Singh, S. Maharjan, H.-S. Li, S.-K. Kang, J.-D. Bok, C.-S. Cho, Y.-J. Choi, *European Journal of Pharmaceutics and Biopharmaceutics* **2014**, *88*, 768.

[22] S. Modaresi, S. Pacelli, S. Subham, K. Dathathreya, A. Paul, *Adv. Therap.* **2020**, *3*, 1900130.

[23] S. Pathak, S. Regmi, P. Shrestha, I. Choi, K. Doh, J. Jeong, *Small* **2019**, 1901269.

[24] J. A. Copp, R. H. Fang, B. T. Luk, C.-M. J. Hu, W. Gao, K. Zhang, L. Zhang, *Proc Natl Acad Sci USA* **2014**, *111*, 13481.

[25] X. Sun, G. Wang, H. Zhang, S. Hu, X. Liu, J. Tang, Y. Shen, *ACS Nano* **2018**, *12*, 6179.

[26] P. Angsantikul, S. Thamphiwatana, Q. Zhang, K. Spiekermann, J. Zhuang, R. H. Fang, W. Gao, M. Obonyo, L. Zhang, *Adv. Therap.* **2018**, *1*, 1800016.

[27] R. H. Fang, A. V. Kroll, W. Gao, L. Zhang, *Adv. Mater.* **2018**, *30*, 1706759.

[28] T. Nie, Z. He, Y. Zhou, J. Zhu, K. Chen, L. Liu, K. W. Leong, H.-Q. Mao, Y. Chen, *ACS Appl. Mater. Interfaces* **2019**, *11*, 29593.

[29] Z. Zeng, P. Zhao, L. Liu, X. Gao, H.-Q. Mao, Y. Chen, *ACS Appl. Mater. Interfaces* **2018**, *10*, 24969.

[30] Z. He, Y. Hu, T. Nie, H. Tang, J. Zhu, K. Chen, L. Liu, K. W. Leong, Y. Chen, H.-Q. Mao, *Acta Biomaterialia* **2018**, *81*, 195.

[31] L. S. Grundy, V. E. Lee, N. Li, C. Sosa, W. D. Mulhearn, R. Liu, R. A. Register, A. Nikoubashman, R. K. Prud'homme, A. Z. Panagiotopoulos, R. D. Priestley, *ACS Nano* **2018**, *12*, 4660.

[32] R. F. Pagels, J. Edelstein, C. Tang, R. K. Prud'homme, *Nano Lett.* **2018**, *18*, 1139.

[33] N. M. Pinkerton, M. E. Gindy, V. L. Calero-DdelC, T. Wolfson, R. F. Pagels, D. Adler, D. Gao, S. Li, R. Wang, M. Zevon, N. Yao, C. Pacheco, M. J. Therien, C. Rinaldi, P. J. Sinko, R. K. Prud'homme, *Adv. Healthcare Mater.* **2015**, *4*, 1376.

[34] L. Gutierrez, L. Gomez, S. Irusta, M. Arruebo, J. Santamaria, *Chemical Engineering Journal* **2011**, *171*, 674.

[35] A. W. York, K. R. Zablocki, D. R. Lewis, L. Gu, K. E. Uhrich, R. K. Prud'homme, P. V. Moghe, *Adv. Mater.* **2012**, *24*, 733.

[36] H. D. Lu, A. C. Spiegel, A. Hurley, L. J. Perez, K. Maisel, L. M. Ensign, J. Hanes, B. L. Bassler, M. F. Semmelhack, R. K. Prud'homme, *Nano Lett.* **2015**, *15*, 2235.

[37] S. D. Allen, Y.-G. Liu, S. Bobbala, L. Cai, P. I. Hecker, R. Temel, E. A. Scott, *Nano Res.* **2018**, *11*, 5689.

[38] C. Zhang, V. J. Pansare, R. K. Prud'homme, R. D. Priestley, *Soft Matter* **2012**, *8*, 86.

[39] Y. Liu, C. Cheng, Y. Liu, R. K. Prud'homme, R. O. Fox, *Chemical Engineering Science* **2008**, *63*, 2829.

[40] J. Feng, C. E. Markwalter, C. Tian, M. Armstrong, R. K. Prud'homme, *J Transl Med* **2019**, *17*, 200.

[41] R. H. Fang, K. N. H. Chen, S. Aryal, C.-M. J. Hu, K. Zhang, L. Zhang, *Langmuir* **2012**, *28*, 13824.

[42] P. Nimbalkar, P. Tabada, A. Bokare, J. Chung, M. Mousavi, M. Simon, F. Erogbogbo, *MRC* **2019**, *9*, 1053.

[43] N. Yang, Y. Ding, Y. Zhang, B. Wang, X. Zhao, K. Cheng, Y. Huang, M. Taleb, J. Zhao, W.-F. Dong, L. Zhang, G. Nie, *ACS Appl. Mater. Interfaces* **2018**, *10*, 22963.

[44] R. JC. Bose, B. J. Kim, Y. Arai, I. Han, J. J. Moon, R. Paulmurugan, H. Park, S.-H. Lee, *Biomaterials* **2018**, *185*, 360.

[45] Y. Liu, S. Li, X. Liu, H. Sun, T. Yue, X. Zhang, B. Yan, D. Cao, *ACS Appl. Mater. Interfaces* **2019**, *11*, 23822.

[46] A. Jayk Bernal, M. M. Gomes da Silva, D. B. Musungaie, E. Kovalchuk, A. Gonzalez, V. Delos Reyes, A. Martín-Quirós, Y. Caraco, A. Williams-Diaz, M. L. Brown, J. Du, A. Pedley, C. Assaid, J. Strizki, J. A. Grobler, H. H. Shamsuddin, R. Tipping, H. Wan, A. Paschke, J. R. Butterton, M. G. Johnson, C. De Anda, *N Engl J Med* **2022**, *386*, 509.

[47] W. Fan, Q. Wei, J. Xiang, Y. Tang, Q. Zhou, Y. Geng, Y. Liu, R. Sun, L. Xu, G. Wang, Y. Piao, S. Shao, Z. Zhou, J. Tang, T. Xie, Z. Li, Y. Shen, *Advanced Materials* **2022**, 2109189.

[48] A. C. Piffer, G. Camilli, M. Bohm, R. Lavenir, J. Quintin, **n.d.**, 28.

[49] Y. Hou, J. Jin, H. Duan, C. Liu, L. Chen, W. Huang, Z. Gao, M. Jin, *Biomaterials* **2022**, *283*, 121440.

[50] T. Maric, S. Atladóttir, L. H. E. Thamdrup, O. Ilchenko, M. Ghavami, A. Boisen, *Applied Materials Today* **2022**, *27*, 101418.

[51] L. S. L. Janardhanam, S. P. Bandi, V. V. K. Venuganti, *ACS Appl. Mater. Interfaces* **2022**, *14*, 10030.

[52] M. J. Carrasco, S. Alishetty, M.-G. Alameh, H. Said, L. Wright, M. Paige, O. Soliman, D. Weissman, T. E. Cleveland, A. Grishaev, M. D. Buschmann, *Commun Biol* **2021**, *4*, 956.

[53] Q. Liu, X. Wang, X. Liu, S. Kumar, G. Gochman, Y. Ji, Y.-P. Liao, C. H. Chang, W. Situ, J. Lu, J. Jiang, K.-C. Mei, H. Meng, T. Xia, A. E. Nel, *ACS Nano* **2019**, *13*, 4778.

[54] Y. Xia, L. Rao, H. Yao, Z. Wang, P. Ning, X. Chen, *Adv. Mater.* **2020**, 2002054.

[55] M. Li, H. Zhou, C. Yang, Y. Wu, X. Zhou, H. Liu, Y. Wang, *Journal of Controlled Release* **2020**, *323*, 253.

[56] X. Hu, G. Yang, S. Chen, S. Luo, J. Zhang, *Biomater. Sci.* **2020**, 10.1039.C9BM01378D.

[57] Y. Miao, Y. Lin, K. Chen, P. Luo, S. Chuang, Y. Yu, H. Tai, C. Chen, K. Lin, H. Sung, *Adv. Mater.* **2021**, 2104139.

[58] Q. Song, H. Zhao, C. Zheng, K. Wang, H. Gao, Q. Feng, H. Zhang, Z. Zhang, Y. Zhang, L. Wang, *Adv. Funct. Mater.* **2021**, 2104994.

[59] L. Yin, C. Peng, Y. Tang, Y. Yuan, J. Liu, T. Xiang, F. Liu, X. Zhou, X. Li, *Biomater. Sci.* **2020**, *8*, 3640.

[60] D. S. Leventhal, A. Sokolovska, N. Li, C. Plescia, S. A. Kolodziej, C. W. Gallant, R. Christmas, J.-R. Gao, M. J. James, A. Abin-Fuentes, M. Momin, C. Bergeron, A. Fisher, P. F. Miller, K. A. West, J. M. Lora, *Nat Commun* **2020**, *11*, 2739.

[61] K. Chen, Y. Zhu, Y. Zhang, T. Hamza, H. Yu, A. Saint Fleur, J. Galen, Z. Yang, H. Feng, *Sci. Transl. Med.* **2020**, *12*, eaax4905.

[62] K. Chen, Y. Zhu, Y. Zhang, T. Hamza, H. Yu, A. Saint Fleur, J. Galen, Z. Yang, H. Feng, *Sci. Transl. Med.* **2020**, *12*, eaax4905.

[63] R. Kiefer, M. Jurisic, C. Dahlem, M. Koch, M. J. Schmitt, A. K. Kiemer, M. Schneider, F. Breinig, *Biotechnology and Bioengineering* **2020**, *117*, 776.

[64] J. Xu, Q. Ma, Y. Zhang, Z. Fei, Y. Sun, Q. Fan, B. Liu, J. Bai, Y. Yu, J. Chu, J. Chen, C. Wang, *Nat Commun* **2022**, *13*, 110.

[65] G. P. Howard, G. Verma, X. Ke, W. M. Thayer, T. Hamerly, V. K. Baxter, J. E. Lee, R. R. Dinglasan, H.-Q. Mao, *Nano Res.* **2019**, *12*, 837.

[66] B. K. Johnson, R. K. Prud'homme, *Aust. J. Chem.* **2003**, *56*, 1021.

[67] Y. Hu, Z. He, Y. Hao, L. Gong, M. Pang, G. P. Howard, H.-H. Ahn, M. Brummet, K. Chen, H. Liu, X. Ke, J. Zhu, C. F. Anderson, H. Cui, C. G. Ullman, C. A. Carrington, M. G. Pomper, J.-H. Seo, R. Mittal, I. Minn, H.-Q. Mao, *ACS Nano* **2019**, *13*, 10161.

[68] R. D. Groot, P. B. Warren, *The Journal of Chemical Physics* **1997**, *107*, 4423.

[69] C. E. Markwalter, B. Uralcan, I. Pelczer, S. Zarzhitsky, M. H. Hecht, R. K. Prud'homme, P. G. Debenedetti, *ACS Nano* **2020**, acsnano.0c06056.

[70] S. M. D'Addio, C. Kafka, M. Akbulut, P. Beattie, W. Saad, M. Herrera, M. T. Kennedy, R. K. Prud'homme, *Mol. Pharmaceutics* **2010**, *7*, 557.

[71] Y. Chen, Y. Zhang, M. Chen, J. Zhuang, R. H. Fang, W. Gao, L. Zhang, *Small* **2019**, *15*, 1804994.

[72] L. Rao, W. Wang, Q.-F. Meng, M. Tian, B. Cai, Y. Wang, A. Li, M. Zan, F. Xiao, L.-L. Bu, G. Li, A. Li, Y. Liu, S.-S. Guo, X.-Z. Zhao, T.-H. Wang, W. Liu, J. Wu, *Nano Lett.* **2019**, *19*, 2215.

[73] J. Shi, W. Yu, L. Xu, N. Yin, W. Liu, K. Zhang, J. Liu, Z. Zhang, *Nano Lett.* **2020**, *20*, 780.

[74] P. Angelikopoulos, L. Sarkisov, Z. Cournia, P. Gkeka, *Nanoscale* **2017**, *9*, 1040.

[75] K.-H. Bang, Y.-G. Na, H. W. Huh, S.-J. Hwang, M.-S. Kim, M. Kim, H.-K. Lee, C.-W. Cho, *Cancers* **2019**, *11*, 807.

[76] A. R. N. Bastos, C. D. S. Brites, P. A. Rojas□Gutierrez, C. DeWolf, R. A. S. Ferreira, J. A. Capobianco, L. D. Carlos, *Adv. Funct. Mater.* **2019**, 1905474.

[77] H. Cao, Z. Dan, X. He, Z. Zhang, H. Yu, Q. Yin, Y. Li, *ACS Nano* **2016**, *10*, 7738.

[78] T. Nie, Z. He, J. Zhu, L. Liu, Y. Chen, *Adv. Therap.* **2020**, 2000016.

[79] E. Rideau, R. Dimova, P. Schwille, F. R. Wurm, K. Landfester, *Chem. Soc. Rev.* **2018**, *47*, 8572.

[80] Y. Kim, F. Fay, D. P. Cormode, B. L. Sanchez-Gaytan, J. Tang, E. J. Hennessy, M. Ma, K. Moore, O. C. Farokhzad, E. A. Fisher, W. J. M. Mulder, R. Langer, Z. A. Fayad, *ACS Nano* **2013**, *7*, 9975.

[81] N. M. Pinkerton, L. Behar, K. Hadri, B. Amouroux, C. Mingotaud, D. R. Talham, S. Chassaing, J.-D. Marty, *Nanoscale* **2017**, *9*, 1403.

[82] M. Aouadi, G. J. Tesz, S. M. Nicoloro, M. Wang, M. Chouinard, E. Soto, G. R. Ostroff, M. P. Czech, *Nature* **2009**, *458*, 1180.

[83] G. C.-F. Chan, W. K. Chan, D. M.-Y. Sze, *J Hematol Oncol* **2009**, *2*, 25.

[84] Y. Wu, Q. Jin, Y. Chen, H. Li, C. Deng, Z. Sun, Y. Li, B. Wang, H. Li, C. Wu, L. Zhang, M. Xie, *Biomater. Sci.* **2020**, 10.1039.D0BM01028F.

[85] J. G. Croissant, K. S. Butler, J. I. Zink, C. J. Brinker, *Nat Rev Mater* **2020**, DOI 10.1038/s41578-020-0230-0.

[86] K. A. Dawson, Y. Yan, *Nat. Nanotechnol.* **2021**, *16*, 229.

[87] H. Hu, C. Yang, M. Li, D. Shao, H.-Q. Mao, K. W. Leong, *Materials Today* **2020**, S136970212030300X.

[88] J. Fu, Z. Gu, Y. Liu, J. Zhang, H. Song, Y. Yang, Y. Yang, O. Noonan, J. Tang, C. Yu, *Chem. Sci.* **2019**, *10*, 10388.

[89] H. Shen, S. Hong, R. K. Prud'homme, Y. Liu, *J Nanopart Res* **2011**, *13*, 4109.

[90] S. Bobbala, S. D. Allen, E. A. Scott, *Nanoscale* **2018**, *10*, 5078.

[91] C. E. Markwalter, R. K. Prud'homme, *Journal of Pharmaceutical Sciences* **2018**, *107*, 2465.

[92] B. K. Johnson, R. K. Prud'homme, *AIChE J.* **2003**, *49*, 2264.

[93] D. Shao, M. Li, Z. Wang, X. Zheng, Y.-H. Lao, Z. Chang, F. Zhang, M. Lu, J. Yue, H. Hu, H. Yan, L. Chen, W. Dong, K. W. Leong, *Adv. Mater.* **2018**, *30*, 1801198.

[94] Z. Zhu, *Biomaterials* **2013**, *34*, 10238.

[95] Z. He, Z. Liu, H. Tian, Y. Hu, L. Liu, K. W. Leong, H.-Q. Mao, Y. Chen, *Nanoscale* **2018**, *10*, 3307.

[96] H. Tian, Z. He, C. Sun, C. Yang, P. Zhao, L. Liu, K. W. Leong, H.-Q. Mao, Z. Liu, Y. Chen, *Adv. Healthcare Mater.* **2018**, *7*, 1800285.

[97] L. Sun, Z. Liu, H. Tian, Z. Le, L. Liu, K. W. Leong, H.-Q. Mao, Y. Chen, *Biomacromolecules* **2019**, *20*, 528.

[98] Z. Fan, P. Y. Li, J. Deng, S. C. Bady, H. Cheng, *Nano Res.* **2018**, *11*, 5573.

[99] W. Ma, D. Zhu, J. Li, X. Chen, W. Xie, X. Jiang, L. Wu, G. Wang, Y. Xiao, Z. Liu, F. Wang, A. Li, D. Shao, W. Dong, W. Liu, Y. Yuan, *Theranostics* **2020**, *10*, 1281.

[100] X. Wei, J. Gao, R. H. Fang, B. T. Luk, A. V. Kroll, D. Dehaini, J. Zhou, H. W. Kim, W. Gao, W. Lu, L. Zhang, *Biomaterials* **2016**, *111*, 116.

[101] S.-Y. Li, H. Cheng, B.-R. Xie, W.-X. Qiu, J.-Y. Zeng, C.-X. Li, S.-S. Wan, L. Zhang, W.-L. Liu, X.-Z. Zhang, *ACS Nano* **2017**, *11*, 7006.

[102] C. Li, X.-Q. Yang, J. An, K. Cheng, X.-L. Hou, X.-S. Zhang, Y.-G. Hu, B. Liu, Y.-D. Zhao, *Theranostics* **2020**, *10*, 867.

[103] M. Lazaratos, K. Karathanou, L. Mainas, A. Chatzigoulas, N. Pippa, C. Demetzos, Z. Cournia, *Biochimica et Biophysica Acta (BBA) - General Subjects* **2020**, 129671.

[104] Z. He, Y. Hu, T. Nie, H. Tang, J. Zhu, K. Chen, L. Liu, K. W. Leong, Y. Chen, H.-Q. Mao, *Acta Biomaterialia* **2018**, *81*, 195.

[105] D. Qiao, L. Liu, Y. Chen, C. Xue, Q. Gao, H.-Q. Mao, K. W. Leong, Y. Chen, *Nano Lett.* **2018**, *18*, 3007.

[106] Z. Liu, M. Ramezani, R. O. Fox, J. C. Hill, M. G. Olsen, *Ind. Eng. Chem. Res.* **2015**, *54*, 4512.

[107] R. Li, Y. He, S. Zhang, J. Qin, J. Wang, *Acta Pharmaceutica Sinica B* **2018**, *8*, 14.

[108] C. E. Markwalter, R. K. Prud'homme, *Journal of Pharmaceutical Sciences* **2018**, *107*, 2465.

[109] H. Shen, S. Hong, R. K. Prud'homme, Y. Liu, *J Nanopart Res* **2011**, *13*, 4109.

[110] P. X. Ma, *Advanced Drug Delivery Reviews* **2008**, *60*, 184.

[111] L. Zhang, Q. Feng, J. Wang, J. Sun, X. Shi, X. Jiang, *Angew. Chem. Int. Ed.* **2015**, *54*, 3952.

[112] R. Molinaro, M. Evangelopoulos, J. R. Hoffman, C. Corbo, F. Taraballi, J. O. Martinez, K. A. Hartman, D. Cosco, G. Costa, I. Romeo, M. Sherman, D. Paolino, S. Alcaro, E. Tasciotti, *Adv. Mater.* **2018**, *30*, 1702749.

[113] D. J. Kozuch, K. Ristroph, R. K. Prud'homme, P. G. Debenedetti, *ACS Nano* **2020**, acsnano.0c01835.

[114] T. I. Morozova, V. E. Lee, N. Bizmark, S. S. Datta, R. K. Prud'homme, A. Nikoubashman, R. D. Priestley, *ACS Cent. Sci.* **2020**, *6*, 166.

[115] A. V. Kroll, R. H. Fang, Y. Jiang, J. Zhou, X. Wei, C. L. Yu, J. Gao, B. T. Luk, D. Dehaini, W. Gao, L. Zhang, *Adv. Mater.* **2017**, *29*, 1703969.

[116] D. Shao, F. Zhang, F. Chen, X. Zheng, H. Hu, C. Yang, Z. Tu, Z. Wang, Z. Chang, J. Lu, T. Li, Y. Zhang, L. Chen, K. W. Leong, W. Dong, *Adv. Mater.* **2020**, *32*, 2004385.

[117] A. V. Kroll, R. H. Fang, Y. Jiang, J. Zhou, X. Wei, C. L. Yu, J. Gao, B. T. Luk, D. Dehaini, W. Gao, L. Zhang, *Adv. Mater.* **2017**, *29*, 1703969.

[118] Y. Guo, D. Wang, Q. Song, T. Wu, X. Zhuang, Y. Bao, M. Kong, Y. Qi, S. Tan, Z. Zhang, *ACS Nano* **2015**, *9*, 6918.

[119] J. M. Silva, E. Zupancic, G. Vandermeulen, V. G. Oliveira, A. Salgado, M. Videira, M. Gaspar, L. Graca, V. Préat, H. F. Florindo, *Journal of Controlled Release* **2015**, *198*, 91.

[120] B. Bahmani, H. Gong, B. T. Luk, K. J. Haushalter, E. DeTeresa, M. Previti, J. Zhou, W. Gao, J. D. Bui, L. Zhang, R. H. Fang, J. Zhang, *Nat Commun* **2021**, *12*, 1999.

[121] X. Gao, S. Li, F. Ding, X. Liu, Y. Wu, J. Li, J. Feng, X. Zhu, C. Zhang, *Adv. Mater.* **2021**, *33*, 2006116.

[122] M. Genin, F. Clement, A. Fattaccioli, M. Raes, C. Michiels, *BMC Cancer* **2015**, *15*, 577.

[123] Y. Koda, T. Teratani, P.-S. Chu, Y. Hagihara, Y. Mikami, Y. Harada, H. Tsujikawa, K. Miyamoto, T. Suzuki, N. Taniki, T. Sujino, M. Sakamoto, T. Kanai, N. Nakamoto, *Nat Commun* **2021**, *12*, 4474.

[124] J. L. Turley, H. B. T. Moran, C. P. McEntee, K. O'Grady, N. Muñoz-Wolf, L. Jin, F. Follmann, P. Andersen, M. Andersson, E. C. Lavelle, *Biomaterials* **2021**, *275*, 120961.

[125] O. J. Finn, *Nat Rev Immunol* **2003**, *3*, 630.

[126] G. Deng, Z. Sun, S. Li, X. Peng, W. Li, L. Zhou, Y. Ma, P. Gong, L. Cai, *ACS Nano* **2018**, *12*, 12096.

[127] X. Feng, W. Xu, Z. Li, W. Song, J. Ding, X. Chen, *Adv. Sci.* **2019**, *6*, 1900101.

[128] G. Garcia, M.-H. Kim, V. A. Morikis, S. I. Simon, *Front. Immunol.* **2020**, *11*, 571489.

[129] E. Ivanova, *Bioengineered* **2021**, *12*, 8325.

[130] Z. Le, Y. Chen, H. Han, H. Tian, P. Zhao, C. Yang, Z. He, L. Liu, K. W. Leong, H.-Q. Mao, Z. Liu, Y. Chen, *ACS Appl. Mater. Interfaces* **2018**, *10*, 42186.

[131] J. Y. Lock, T. L. Carlson, R. L. Carrier, *Advanced Drug Delivery Reviews* **2018**, *124*, 34.

[132] D. T. Riglar, P. A. Silver, *Nat Rev Microbiol* **2018**, *16*, 214.

[133] S. Lin, S. Mukherjee, J. Li, W. Hou, C. Pan, J. Liu, *Sci. Adv.* **2021**, *7*, eabf0677.

[134] X. Wang, Z. Cao, M. Zhang, L. Meng, Z. Ming, J. Liu, *Sci. Adv.* **2020**, *6*, eabb1952.

[135] W. Li, H. Wang, X. G. Xu, Y. Yu, *Langmuir* **2020**, *36*, 6169.

[136] C. Sabu, P. Mufeedha, K. Pramod, *Expert Opinion on Drug Delivery* **2019**, *16*, 27.

[137] L. Zhang, H. Peng, W. Zhang, Y. Li, L. Liu, T. Leng, *Theranostics* **2020**, *10*, 8479.

[138] H. P. van Steenwijk, A. Bast, A. de Boer, *Nutrients* **2021**, *13*, 1333.

[139] J. Chen, R. Seviour, *Mycological Research* **2007**, *111*, 635.

[140] H. S. Goodridge, A. J. Wolf, D. M. Underhill, *Immunological Reviews* **2009**, *230*, 38.

[141] X. Zhou, X. Zhang, S. Han, Y. Dou, M. Liu, L. Zhang, J. Guo, Q. Shi, G. Gong, R. Wang, J. Hu, X. Li, J. Zhang, *Nano Lett.* **2017**, *17*, 1056.

[142] X. Zhang, X. Xu, Y. Chen, Y. Dou, X. Zhou, L. Li, C. Li, H. An, H. Tao, H. Hu, X. Li, J. Zhang, *Materials Today* **2017**, *20*, 301.

[143] Y. T. Tam, K. K. W. To, A. H. L. Chow, *Colloids and Surfaces B: Biointerfaces* **2016**, *139*, 249.

[144] C. Williams, R. Panaccione, S. Ghosh, K. Rioux, *Therap Adv Gastroenterol* **2011**, *4*, 237.

[145] S. E. Berends, A. S. Strik, M. Löwenberg, G. R. D'Haens, R. A. A. Mathôt, *Clin Pharmacokinet* **2019**, *58*, 15.

[146] Y. Miao, K. Chen, C. Chen, F. Mi, Y. Lin, Y. Chang, C. Chiang, J. Wang, K. Lin, H. Sung, *Adv. Mater.* **2021**, 2100701.

[147] Y. Sun, B. Duan, H. Chen, X. Xu, *Adv. Healthcare Mater.* **2020**, *9*, 1901805.

[148] C. Pan, J. Li, W. Hou, S. Lin, L. Wang, Y. Pang, Y. Wang, J. Liu, *Adv. Mater.* **2021**, 2007379.

[149] Y. Sun, B. Duan, H. Chen, X. Xu, *Adv. Healthcare Mater.* **2020**, *9*, 1901805.

[150] X. Wang, J. Yan, L. Wang, D. Pan, Y. Xu, F. Wang, J. Sheng, X. Li, M. Yang, *Theranostics* **2020**, *10*, 10808.

[151] S. Y. Oh, K.-A. Cho, J. L. Kang, K. H. Kim, S.-Y. Woo, *International Journal of Molecular Medicine* **2014**, *33*, 333.

[152] B. A. Hendrickson, R. Gokhale, J. H. Cho, *Clin Microbiol Rev* **2002**, *15*, 79.

[153] E. R. Soto, G. R. Ostroff, *Bioconjugate Chem.* **2008**, *19*, 840.

[154] T. Ren, J. Gou, W. Sun, X. Tao, X. Tan, P. Wang, Y. Zhang, H. He, T. Yin, X. Tang, *Mol. Pharmaceutics* **2018**, *15*, 2870.

[155] D. Liu, S. Lu, L. Zhang, L. Zhang, M. Ji, X.-G. Liu, Z. Yu, R. Liu, *Nanoscale Adv.* **2020**, *2*, 3494.

[156] Y. S. Grewal, M. J. A. Shiddiky, S. M. Mahler, G. A. Cangelosi, M. Trau, *ACS Appl. Mater. Interfaces* **2016**, *8*, 30649.

[157] R. Honegger, A. Haisch, *New Phytologist* **2001**, *150*, 739.

[158] F. Hong, J. Yan, J. T. Baran, D. J. Allendorf, R. D. Hansen, G. R. Ostroff, P. X. Xing, N.-K. V. Cheung, G. D. Ross, *J Immunol* **2004**, *173*, 797.

[159] N. A. Mabbott, D. S. Donaldson, H. Ohno, I. R. Williams, A. Mahajan, *Mucosal Immunol* **2013**, *6*, 666.

[160] J. Ahn, S. Son, S. C. Oliveira, G. N. Barber, *Cell Reports* **2017**, *21*, 3873.

[161] A. Amouzegar, M. Chelvanambi, J. N. Filderman, W. J. Storkus, J. J. Luke, *Cancers* **2021**, *13*, 2695.

[162] M. An, C. Yu, J. Xi, J. Reyes, G. Mao, W.-Z. Wei, H. Liu, **2019**, 27.

[163] E. N. Chin, C. Yu, V. F. Vartabedian, Y. Jia, M. Kumar, A. M. Gamo, W. Vernier, S. H. Ali, M. Kissai, D. C. Lazar, N. Nguyen, L. E. Pereira, B. Benish, A. K. Woods, S. B. Joseph, A. Chu, K. A. Johnson, P. N. Sander, F. Martínez-Peña, E. N. Hampton, T. S. Young, D. W. Wolan, A. K. Chatterjee, P. G. Schultz, H. M. Petrassi, J. R. Teijaro, L. L. Lairson, *Science* **2020**, *369*, 993.

[164] X. Lu, L. Miao, W. Gao, Z. Chen, K. J. McHugh, Y. Sun, Z. Tochka, S. Tomasic, K. Sadtler, A. Hyacinthe, Y. Huang, T. Graf, Q. Hu, M. Sarmadi, R. Langer, D. G. Anderson, A. Jaklenec, *Sci. Transl. Med.* **2020**, *12*, eaaz6606.

[165] M. Luo, H. Wang, Z. Wang, H. Cai, Z. Lu, Y. Li, M. Du, G. Huang, C. Wang, X. Chen, M. R. Porembka, J. Lea, A. E. Frankel, Y.-X. Fu, Z. J. Chen, J. Gao, *Nature Nanotech* **2017**, *12*, 648.

[166] H. Kang, K. Zhang, D. S. H. Wong, F. Han, B. Li, L. Bian, *Biomaterials* **2018**, *178*, 681.

[167] D. Kwon, B. G. Cha, Y. Cho, J. Min, E.-B. Park, S.-J. Kang, J. Kim, *Nano Lett.* **2017**, *17*, 2747.

[168] B. Han, K. Baruah, E. Cox, D. Vanrompay, P. Bossier, *Front. Immunol.* **2020**, *11*, 658.

[169] H. Maeda, *Advanced Drug Delivery Reviews* **2015**, *91*, 3.

[170] J. Fang, W. Islam, H. Maeda, *Advanced Drug Delivery Reviews* **2020**, *157*, 142.

[171] K. Guo, N. Xiao, Y. Liu, Z. Wang, J. Tóth, J. Gyenis, V. K. Thakur, A. Oyane, Q. T. H. Shubhra, *Nano Materials Science* **2021**, S2589965121000933.